Carbon nanotubes filled with continuous ferromagnetic α-Fe nanowires and surface-functionalized with paramagnetic Gd(III): A candidate magnetic hyperthermia structure and MRI contrast agent

Thesis submitted for the degree of Doctor of Philosophy

By

Taze Peci

Queen Mary University of London

Supervisors: Dr. M. Baxendale and Dr. T.J.S. Dennis

Dedication

To my lovely daughter Viviana

Declaration

I declare that the work presented in this thesis was performed entirely by myself during the course of my Ph.D. studies at the School of Physics and Astronomy, Queen Mary University of London, under the supervision of Dr. Mark Baxendale and Dr.John Dennis. No part of this thesis has been submitted elsewhere for any other degree or qualification.

Taze Peci

Acknowledgements

My greatest thanks go to my supervisors, Dr. Mark Baxendale and Dr. John Dennis for their continuous support, guidance and patience in the course of this project, for believing in my abilities and always encouraging me to advance further.

I would like to thank all the support staff that helped me in the course of this PhD: Dr. Rory Wilson for the help in the X-ray diffraction measurements, Dr. Nadja Tarakina and Russell Bailey for the help in scanning electron microscopy and transmission electron microscopy and Dr. Ray Burton-Smith for the help in the electron paramagnetic resonance spectroscopy measurements. I also would like to thank Dr. Zofia Luklinska for the help in electron microscopy measurements performed in the first year.

Many thanks to Dr. Demie Kepaptsoglou for the help in scanning transmission electron microscopy and electron energy loss spectroscopy measurements and to Dr. Richard Thorogate for the help in the magnetic measurements.

Also, many thanks to Dr. Harold Toms for the help in nuclear magnetic resonance spectroscopy measurements and Natalie Ludgate for the help in inductively coupled plasma optical emission spectrometry.

I am grateful for the financial support from the Engineering and Physical Science Research Council, UK.

I would like to specially thank my family for the support, encouragement and

love during these years that I have spent in pursuit of my doctorate degree.

Thanks also to all my friends at Queen Mary University of London for the help and good time we had throughout the PhD course: Maureen Willis, Filippo Boi, Ali Karatutlu, Calum McAndrew, Eva Zarkadoula, Shamim Khademi, Eleftherios Andritsos, Mingying Song, Juan Du, Osman Ersoy, Dominic Carter, Muhammad Ibrar, Helen Duncan, Viswanathan Mohandoss, Asmi Barot, Prashantha Murahari and Serena Maugeri.

Abstract

The main goal of this project was the development of carbon nanotubes as a candidate for dual-functioning magnetic hyperthermia structure and magnetic resonance imaging contrast agent. This was achieved by filling carbon nanotubes with continuous ferromagnetic α-Fe nanowires and surface functionalized with paramagnetic Gd(III). Also, length control of both nanotube and nanowire was investigated.

Firstly, a low vapour flow-rate and constant evaporation temperature chemical vapour deposition method based on the thermal decomposition of ferrocene was employed which achieved continuous α-Fe nanowires on the same scale as the nanotube for lengths >10 μm without the necessity of post-synthesis heat-treatment or introduction of other precursor elements. The low vapour flow-rate regime has the advantage of sustaining the intrinsic temperature gradient at the tip of the forming structure which drives the vapour feedstock to the growth front to guarantee continuous nanowire formation. For initially mixed-phase nanowires of length less than 10 μm, the continuous α-Fe nanowires were achieved by post-synthesis heat treatment.

Secondly, a simple wet chemical method involving only sonication in aqueous $GdCl_3$ solution was used for surface functionalization of iron-filled multiwalled carbon nanotubes with gadolinium. Functional groups on the sidewalls produced by the sonication provide active nucleation sites for the loading of Gd^{3+}

ions. Characterization by electron paramagnetic resonance, electron energy loss spectroscopy, and high-resolution transmission electron microscopy confirmed the presence of Gd^{3+} ions on the sidewall surface. The ferromagnetic properties of the encapsulated iron nanowire maintained after surface functionalization. At room temperature a saturation magnetization of 40 emu/g and a coercivity of 600 Oe were observed.

Heating functionality in an alternating applied magnetic field was quantified through the measurement of specific absorption rate: 50 W/g_{Fe} and the intrinsic loss power: 1.12 nHm^2kg^{-1} at magnetic field strength 8 kA/m and frequency of 696 kHz. These structures exhibited an extremely high relaxivity $r_1 \sim 200$ mM^{-1} s^{-1} at high magnetic field (9.4 T).

Publications

1. Taze Peci, T. John S. Dennis, and Mark Baxendale, Iron-filled multiwalled carbon nanotubes surface-functionalized with paramagnetic Gd (III): A candidate dual-functioning MRI contrast agent and magnetic hyperthermia structure, Carbon 87 (2015) 226-232.

2. Taze Peci and Mark Baxendale, Length and α-Fe content control of self-organised ferromagnetic nanowires encapsulated by multiwalled carbon nanotubes by low flow-rate CVD, Carbon 98 (2016) 519-525.

3. Taze Peci and Mark Baxendale, A facile method for self-organized texturing of iron-filled multiwalled carbon nanotube arrays, Physica Status Solidi A (2017), 1700327.

Contents

List of Abbreviations

CNT ..... Carbon nanotube

SWCNT ..... Single-walled carbon nanotube

MWCNT ..... Multiwalled carbon nanotube

Fe-MWCNT ..... Iron-filled multiwalled carbon nanotube

CVD ..... Chemical vapour deposition

LSCVD ..... Liquid source chemical vapour deposition

SSCVD ..... Solid source chemical vapour deposition

SEM ..... Scanning electron microscopy

EDX ..... Energy dispersive X-ray spectroscopy

TEM ..... Transmission electron microscopy

SAED ..... Selective area electron diffraction

HRTEM ..... High-resolution transmission electron microscopy

STEM ..... Scanning transmission electron microscopy

ADF ..... Annular dark field

HAADF ..... High-angle annular dark field

EELS ..... Electron energy loss spectroscopy

SQUID ..... Semiconducting quantum interference device

XRD ..... X-ray diffraction

SAR ..... Specific absorption rate

ILP ..... Intrinsic loss power

MRI ..... Magnetic resonance imaging

EPR ..... Electron paramagnetic resonance

NMR ..... Nuclear magnetic resonance

SDBS ..... Sodium dodecyl benzene sulfonate

SPIO ..... Superparamagnetic iron oxide

List of Figures

Introduction

Two of the key challenges in cancer research are to detect cancer at the earliest possible time, at a stage when the disease would be still treatable, and to deliver the best possible treatment at the right place. The former requires advances in diagnostics and imaging and the latter would benefit from new modalities of treatment.

Magnetic hyperthermia is an emerging cancer treatment which employs heat dissipated by magnetic nanoparticles in an alternating magnetic field to destroy cancer cells. It is based on the higher sensitivity of cancer cells to temperature in the range of 42 to 46 °C than normal tissue cells [1]. The concept of magnetic hyperthermia was first proposed in 1957 by Gilchrist [2] and recently this technique has shown success in the clinical trials [1]. The most common magnetic material for hyperthermia is currently superparamagnetic iron oxide (SPIO) nanoparticles. The recent success of magnetic hyperthermia in cancer therapy is very promising, but the technique still needs further improvement before it can become a standard medical procedure [3]. In particular, it is necessary to produce magnetic nanoparticles with improved magnetic heating characteristics, minimal inherent toxicity and efficient targeting [3].

In this respect, carbon nanotubes (CNTs) filled with ferromagnetic iron nanowires have been under consideration as the alternative magnetic structures for magnetic hyperthermia cancer therapy [4]. There are several reasons for this interest: (i)

metallic iron can produce heat more efficiently than iron oxide due to higher saturation magnetisation, (ii) the ferromagnetic response can be engineered through the composition and shape anisotropy of the nanowire, (iii) the CNTs chemically isolate the internal nanowire thus reducing toxicity, (iv) the CNT surface can readily be functionalized to prevent agglomeration and (v) iron-filled CNTs provide the opportunity of direct cancer targeting. A magnetic field gradient can drive the translation of iron-filled CNTs toward a desired position and along a given path [4,5].

As it is mention above, another ongoing challenge in cancer research is the early stage accurate detection of cancer. Although magnetic resonance imaging (MRI) is one of the most powerful diagnostic methods available for the human body, it still lacks the spatial resolution for early detection [6]. Given the greater spatial resolution and sensitivity associated with higher frequencies, the current tendency in MRI is to increase the magnetic field strength [7,8]. In clinics today, most MRI scans work at 3 T. However, in pre-clinical animal studies, high magnetic field strengths of 9.4 T and 11.7 T are routinely used [7]. Also, the first human images at the new high-field benchmark of 9.4 T have been reported by Vaughan and co-workers. The results demonstrated the feasibility of safe and successful human imaging at 9.4 T [8]. Generally, at increasing magnetic field strengths, the relaxing properties of available contrast agents change; longitudinal relaxivity (r_1) decreases with increasing field [7]. At field strengths higher than 3 T, the efficacy of Gd(III)-based contrast agents is diminished due to decreased r_1 relaxivity, somewhat limiting contrast-enhanced imaging of tumours [7]. Conse-

quently, new contrast agents need to be specifically tailored to fully exploit the benefits of high-field MRI.

Clearly, it is of great importance to design an unique and versatile structure which would be able to reveal tumours and metastases at the earliest possible time and subsequently treat them by magnetic hyperthermia.

The main goal of this project was to design functionalized CNTs that can act as both a magnetic hyperthermia structure and as an MRI contrast agent for high field imaging. This is achieved by starting with filling the central capillary of CNTs with continuous ferromagnetic α-Fe nanowires, and after that iron-filled CNTs were surface functionalized with paramagnetic Gd (III).

CNTs have drawn a lot of attention since their discovery in 1991 due to their mechanical and chemical stability as well as their electronic and optical properties [4]. They have a high aspect ratio (length/diameter >100) and their unique structure allows filling them with different materials and as well as attaching functional elements to the inert sidewalls [4].

Various functionalization methods for tuning their properties to a given application have been developed. Magnetic functionalization has resulted in nanohybrids with desirable chemical, magnetic, and other physical properties for magnetic hyperthermia cancer therapy, contrast agents for MRI, and magnetic carrier and drug delivery systems [4,5,9–11].

In particular, the possibility of filling CNTs with ferromagnetic nanowires has been investigated for many years owing to the desirable magnetic properties that these materials would possess when accommodated inside CNTs. Ferromagnetic

nanowires encapsulated by multiwalled carbon nanotubes (MWCNTs) are synthesised by chemical vapour deposition (CVD) methods in which the species produced by the thermal decomposition of metallocenes provide nucleating metal droplets and the chemical feedstock for self-organised growth of structures perpendicular to an inert substrate at elevated temperature [12-25]. Confinement of the nanowire within the central capillary of the nanotube can result in unusual compositions not readily obtainable in the bulk. The carbon nanotube chemically passivates the nanowire and prevents its mechanical degradation.

The majority of effort has focussed on encapsulation of elemental α-Fe, owing to both the characteristically high saturation magnetisation and coercivity, by thermal decomposition of ferrocene ($Fe(C_5H_5)_2$) at high temperature $Fe(C_5H_5)_2 \rightarrow Fe + H_2 + CH_4 + C_5H_6 + ...$ [24]. The growth mechanism is controversial but there is consensus for the general features, usually expressed within a vapour-liquid-solid (VLS) framework: liquid droplets of elemental Fe accumulate on the substrate, hydrocarbons from the vapour then decompose on its catalytic surface; carbon is absorbed until the solubility limit of carbon in iron is reached; upon saturation, surface carbon is catalytically graphitised by the Fe resulting in multiwalled carbon nanotube growth perpendicular to the substrate. Subsequent growth is driven by supply of iron and carbon species from the vapour either to the base of the structure or to the open tip, or both [24]. The most commonly observed encapsulated nanowires contain crystallites of α-Fe, γ-Fe, and Fe_3C [18,19,22-24]. In many reports, the nanowires are not continuous but comprise isolated 10s-100s nm length crystallites with a much greater intermediate spacing

and the nanotubes have low graphitic quality (as judged by the straightness of the structure).

A continuous, completely α-Fe nanowire is desirable for magnetic hyperthermia applications, as is control of both nanowire and nanotube length and diameter. Length and diameter control of CNTs is important because toxicology profiles of CNTs significantly differ between CNTs of various sizes (length and diameter) [4]. Control of nanowire length and diameter is an effective method of tuning magnetic properties.

Selection of elemental α-Fe is due to its high saturation magnetisation (220 emu/g at room temperature) which leads to high specific absorption rate (SAR). The γ-Fe is predicted to be paramagnetic at room temperature, whereas Fe_3C although exhibits ferromagnetic behaviour at room temperature has low saturation magnetisation (169 emu/g) compared to that of α-Fe [12,13].

The numerous reports concerning nanowire content control suffer from several major shortcomings: i) the zone-two (synthesis) temperature is expressed as a wide range since the ferrocene vapour is consumed in the sharp temperature gradient at the entrance to the second zone, ii) the post-synthesis cooling rate of the reactor, which could play a critical role in determining the phase content of the nanowire owing to the C-diffusion and γ-α transition, is seldom quantified or controllable, and iii) little attention is paid to the origin of local diffusion gradients which drive the vapour feedstock to the growth front; often, the tacit assumption is that it is simply concentration driven and occasionally the system-specific, radial temperature gradient between the axis of the vapour-containing tube and

substrate is evoked. The temperature gradient driven model could favour base or tip growth depending on whether the substrate or the vapour is the hotter.

One of the objectives of this project was length and α-Fe content control of self-organised ferromagnetic nanowires encapsulated by multiwalled carbon nanotubes. This was achieved by using a low vapour flow-rate and constant evaporation temperature method. I contend that in view of the evidence for the open-tip temperature gradient model at $\sim$10 ccm flow rates, synthesis conditions which favour this condition are desirable since, freed of the necessity to provide a temperature gradient which drives vapour feedstock to the growth front, it facilitates fine-tuning of the synthesis temperature to favour decomposition of Fe_3C into α-Fe and graphitic carbon [26]. Low rates of supply of vapour feedstock also favour low carbide content and the desirable γ-α transition owing to the associated longer residence times (time exposed to elevated temperature). By a similar logic, this regime will guarantee nanowire continuity by providing a local, rather than global, temperature gradient to drive the vapour feedstock to the active growth front. The constant close-to-melting-point temperature used for the evaporation of ferrocene was intended to avoid dispersion in the diameter of the nucleating Fe droplet. The synthesis temperature was fixed in narrow range 880-950 °C to encourage C-diffusion but minimise damping of the tip temperature gradient by the natural gradient in the reactor. Under these constrains, the key variable was the mass flow rate of ferrocene vapour into the second zone of the reactor. This method achieved continuous α-Fe nanowires on the same

scale as the nanotube for lengths greater than 10 μm without the necessity of post-synthesis heat-treatment or introduction of other precursor elements. For initially mixed-phase nanowires of length less than 10 μm, the continuous α-Fe nanowires can be achieved by post-synthesis heat treatment.

Concerning the length control of iron-filled multiwalled carbon nanotubes (Fe-MWCNTs) besides the above method, a facile CVD-based method was used for the texturing of substrate-supported Fe-MWCNTs vertical arrays by exploitation of the interplay of temperature gradients and modulated vapour flow which imposed annular height variation and a vertical-array-to-spherulitic morphological transformation. This method imposed well-defined annular features on the height of the vertical arrays, while maintaining continuity of the iron filling on the micrometre scale. I speculate that the observed annular height variation results from creation of stationary cells of feedstock vapour above the growth front. In conditions of higher substrate temperature and less modulated vapour flow the presence of the stationary cells impacts on the iron island formation process to produce a morphological transformation from array to spherulitic agglomeration.

Once the filling of MWCNTs with continuous ferromagnetic α-Fe nanowires was achieved the second step was the suface funtionalization of Fe-MWCNTs with paramagnetic Gd (III). Generally, covalent and non-covalent modifications are frequently used to functionalize the CNT surface [27,28]. Covalent functionalization is achieved by using both chemical modifications by strong acids and ultra-sonication pre-treatments which may result in severe damage to the side-

walls and can modify the physical properties [27,28]. Moreover, the properties of a sensitive filling material may be destroyed by treatment at high temperature, or strong pH values, required by some methods reported in the literature. For example, the saturation magnetisation of surface functionalized Fe-MWCNTs is dramatically lowered if functionalized via acid treatment because the iron is oxidised by the acid [9].

Non-covalent functionalization is achieved by coating CNTs with amphiphilic surfactant molecules or polymers using various adsorption forces, such as the van der Waals force, hydrogen bonds, electrostatic forces, and π-stacking interactions [29–31]. But, for biomedical applications, the use of polymers, surfactants or specific reactants could affect the biological response [11].

Accordingly, alternative, non-destructive methods for multiple-functionalization and generally application are needed to prepare surface-functionalised CNTs.

I have appoached this problem by using a single-step, wet chemical method involving only sonication in aqueous $GdCl_3$ solution for surface functionalization of Fe-MWCNTs with gadolinium. This method is based on the fact that mild sonication of MWCNTs in deionized water can oxidise existing $–CH_n$ groups on outer walls, initially to –OH then to -C=O and finally to –COOH depending on the degree of local energy density delivered to the surface by the sonication [32]. Functional groups on the sidewalls produced by the sonication provide active nucleation sites for the loading of Gd^{3+} ions.

The advantage of mild pH and sonication conditions has the benefits; (i) the magnetic properties of Fe-MWCNTs are maintained after surface functionaliza-

tion, which will otherwise be destroyed if conventional acid treatment process was applied, and (ii) the method does not involve the additional use of amphiphilic surfactant molecules or polymers which could affect the biological response.

This work demonstrates that Fe-MWCNTs surface-functionalized with Gd^{3+} ions are candidate hybrids for dual-functioning magnetic hyperthermia cancer therapy and MRI contrast agent structures owing to integration of both the heating element (α-Fe) and the paramagnetic Gd (III). The claim of suitability for the magnetic hyperthermia application is made on the basis of measurement of the SAR and the intrinsic loss power (ILP). Whereas, the claim of suitability for the MRI contrast agent functionality is made on the basis of direct observation of a room temperature electron paramagnetic resonance (EPR) signal that is the signature of lanthanide ions with a half filled sub-shell [33, 34] and on the measurement of relaxivity (r_1).

The measurement of relaxivity (r_1) was performed using magnetic field strengths 9.4 T and 14 T to assess viability as contrast agent for high-field imaging.

Thesis outline

Chapter 1 contains the literature review and Chapter 2 explains the theoretical background to this work. In Chapter 1, the current understanding of the growth mechanisms is outlined and the conventional methods that are generally used to synthesize Fe-MWCNTs are described. The shortcomings of previous work in the achievement of a continuous, completely a-Fe nanowire inside MWCNTs and

magnetic properties of Fe-MWCNTs are also reviewed. Finally, methods used to surface functionalize MWCNTs and their shortcomings are described. In Chapter 2, a brief description of the theory behind CVD process, CVD growth rate model and influence of the gas flow rate on control of CVD process is given. Chapter 2, also explaines the theory behind the magnetic hyperthermia and Gd^{3+} based contrast agents.

Chapter 3 outlines the experimental methods employed in this work to produce and characterise Fe-MWCNTs and Gd^{3+}-functionalized Fe-MWCNTs. The final part of the Chapter 3 describes the methods used to estimate the specific absorption rate, the intrinsic loss power and relaxivity.

Experimental results and discussion are described in detail in Chapter 4. The first part of this chapter is concerned with the findings from the length and α-Fe content control of self-organised ferromagnetic nanowires encapsulated by MWCNTs and their magnetic properties. The second part contains the results obtained from the Gd^{3+} functionalized Fe-MWCNTs. The potential of these structures for magnetic hyperthermia and MRI contrast agent is highlighted here by the measurement of the specific absorption rate and relaxivity. The final part of this chapter is dedicated to preliminary work directed at self-organized texturing of Fe-MWCNT arrays.

Chapter 5 summarises the final conclusions of this project.

Chapter 6 describes the suggestions for the future work that follow from this project.

Chapter 1

Literature review

This chapter provides information on CNTs structure, the current understanding of the growth mechnisms of CNTs and methods that are generally used to synthesize Fe-MWCNTs. Several working parameters were varied and investigated in attempt to synthesize MWCNTs filled with completely α-Fe due to its excellent ferromagnetic characteristics. Besides filling the central capillary of MWCNTs with different materials, several methods have been used to surface functionalize the inert sidewalls to fully exploit their potential applications. An overview of these methods is presented in the final part of this chapter.

1.1 Carbon nanotubes structure and modification

Carbon nanotubes, long and thin cylinders of carbon atoms, were discovered in 1991 by Sumio Iimija [35]. They are large macromolecules with the simplest chemical composition and atomic bonding configuration but exhibit perhaps the most extreme diversity and richness among nanomaterials in structures and structure-property relations. Carbon nanotubes have drawn much attention owing to their

mechanical and chemical stability as well as their electronic and optical properties [4]. A carbon nanotube can be either single-walled (SWCNT) or multiwalled (MWCNT) see Figure 1.1 (b and c). Conceptually a SWCNT can be formed by rolling a sheet of graphene into a cylinder along an wrapping (chiral) vector in the graphene plane, whereas MWCNTs comprise many concentric layers of graphene sheets with a fixed spacing of 0.34 nm between the layers.

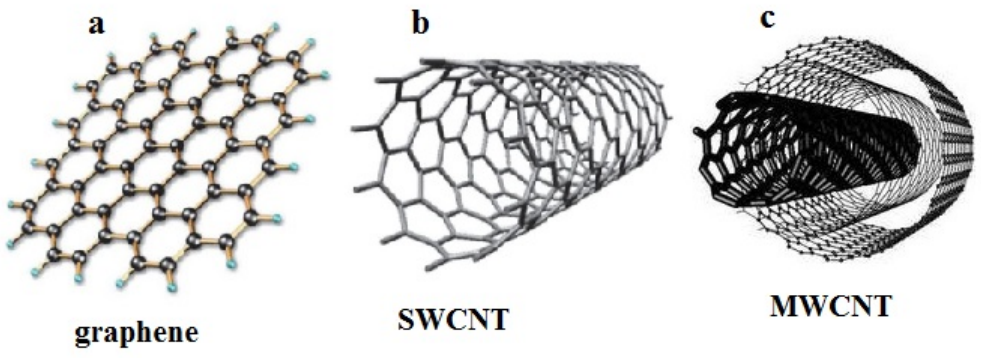

Figure 1.1: Structural images of: a graphene sheet (a), single-walled (b) and multiwalled (c) carbon nanotubes [36].

The properties of CNTs are determined by the geometry, number of walls, diameter, length, defectiveness, and the chirality; three structural types of CNT are shown in Figure 1.2 (b,c,d).

The structure of a SWCNT is characterized by the chiral vector $\mathbf{C} = n\mathbf{a}_1 + m\mathbf{a}_2$, where $\mathbf{a}_1$ and $\mathbf{a}_2$ are the graphitic Bravais lattice vectors, and n and m are integers (Figure 1.2a). The graphitic Bravais lattice vectors $\mathbf{a}_1$ and $\mathbf{a}_2$ define also the translational vector $\mathbf{T}$. The chiral angle θ is that between $\mathbf{a}_1$ and $\mathbf{C}$. The Chiral vector $\mathbf{C}$ determines the circumference of the nanotube and the different values

of n and m lead to the different nanotube structures (Figure 1.2 b,c,d) [36].

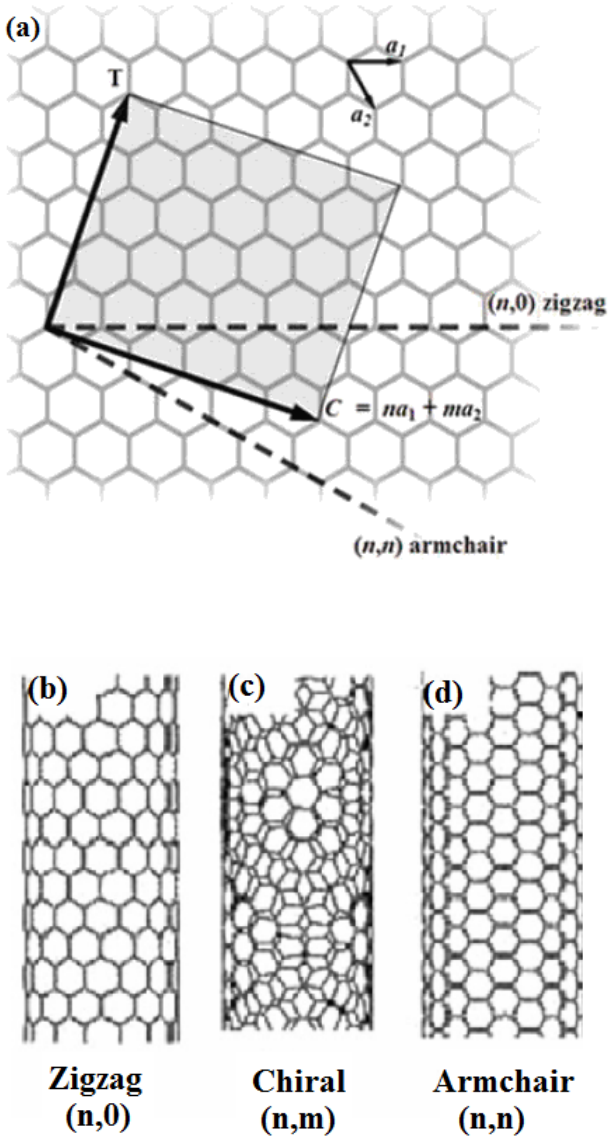

Figure 1.2: An individual graphene sheet indicating lattice configuration of an individual single-wall carbon nanotube showing the chiral vector **C**, the translational vector **T** and the unit vectors $\mathbf{a}_1$ and $\mathbf{a}_2$. The three structural types of SWCNT: zigzag, chiral and armchair shown in (b), (c), (d) respectively, are formed by rolling the graphene sheet along chiral vectors with differing (n, m) indices [36].

The strong sp^2 hybridised carbon bonding of CNTs give rise to a high Young's modulus (maximum measured value 950 GPa) [37]. CNTs have a high aspect ratio (length/diameter >100) [4]. Furthermore, their unique structure allows filling them with different materials and as well as attaching functional elements to the inert sidewalls.

CNTs can be tailored to have specific properties by controlling the growth conditions, but various functionalization methods have been shown to be an easier route for tuning the properties of CNTs to a given application. Depending on the material used for functionalization, the carbon nanotube can have several potential applications including drug delivery systems, contrast agents for MRI imaging, magnetic hyperthermia cancer therapy, CNT-based thermometers, magnetic force microscopy probes [4,5,9-11, 38].

1.2 Synthesis of filled carbon nanotubes by CVD method

Various investigations have been reported on the synthesis of carbon nanotubes but catalytic CVD is the most convenient method for producing different types of carbon nanotubes ranging from the single-walled over multiwalled to metal-filled carbon nanotubes in large quantities and satisfactory quality.

The processes for synthesis of empty and filled carbon nanotubes are similar. At both cases hydrocarbon precursor compounds are required to supply the carbon

for formation of carbon nanotubes. The role of the catalyst is to control the kinetics of the reaction such as the decomposition of the precursor, can be located on the substrate or is delivered via the gas phase. Filled carbon nanotubes can be produced by synthesis and simultaneous filling of the nanotubes, or by a two-step process which involves the preliminary production of the hollow carbon nanotubes which are then filled by chemical methods [4,12-25].

For synthesis and simultaneous filling the most common precursors are metal-organic compounds, since these compounds possess a convenient temperature range for sublimation and thermal decomposition [12-25].

Metallocenes contain both elements carbon and metal in their structure in a fixed ratio of 1:10. They are solid at room temperature and show suitable decomposition behaviour in the temperature range 600-1150 °C [16]. In particular, it was proposed that from temperatures around 600 °C metallocenes starts to decompose according to the reaction:

$$\mathsf{Me(C_5H_5)_2(g) \rightarrow Me(s) + H_2 + CH_4 + C_5H_6 + \ldots}, \tag{1.1}$$

where Me refers to a metallic element, (g) and (s) indicate the gas and solid phases, respectively [24].

The metallocene family has a sandwich structure of two parallel cyclopentadienyl rings with a metal in the centre between these rings (see Figure 1.3) [24].

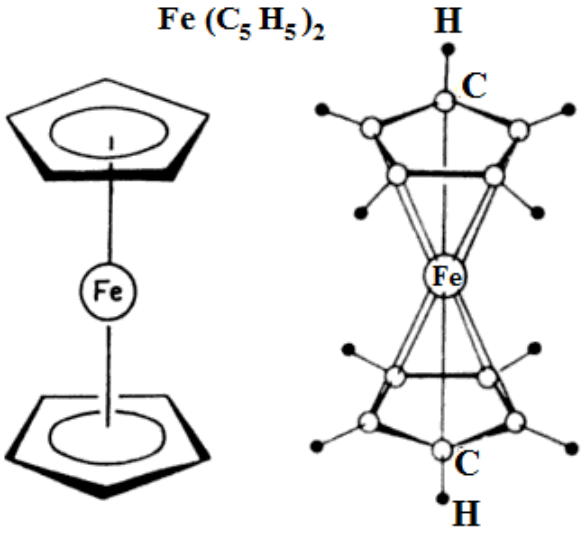

Figure 1.3: The ferrocene molecule as representative of the general structure of metallocenes [39]. It is usually used in the synthesis of MWCNTs filled with α-Fe.

There are two different methods for *in-situ* filling processes: solid source chemical vapour deposition (SSCVD) [14,17,19,24] and liquid source chemical vapour deposition (LSCVD) [17,24]. In the first method a metallocene powder is used as precursor, whereas in the second one the metallocene is dissolved in a liquid hydrocarbon at the outset of the synthesis process. In both cases a horizontal quartz tube and a two zone furnace is generally used. The typical reactor for the SSCVD method is shown in Figure 1.4. In a general SSCVD experiment, metallocene powder is placed in a quartz boat and it is sublimated at the compound specific temperature in the first zone of the reactor (preheater zone). Then the metallocene vapour is transported by a controlled carrier gas flow (usually Ar, N_2 or mixtures of both) into the reaction zone where the decomposition of the metallocene and the growth of metal filled carbon nanotubes occur.

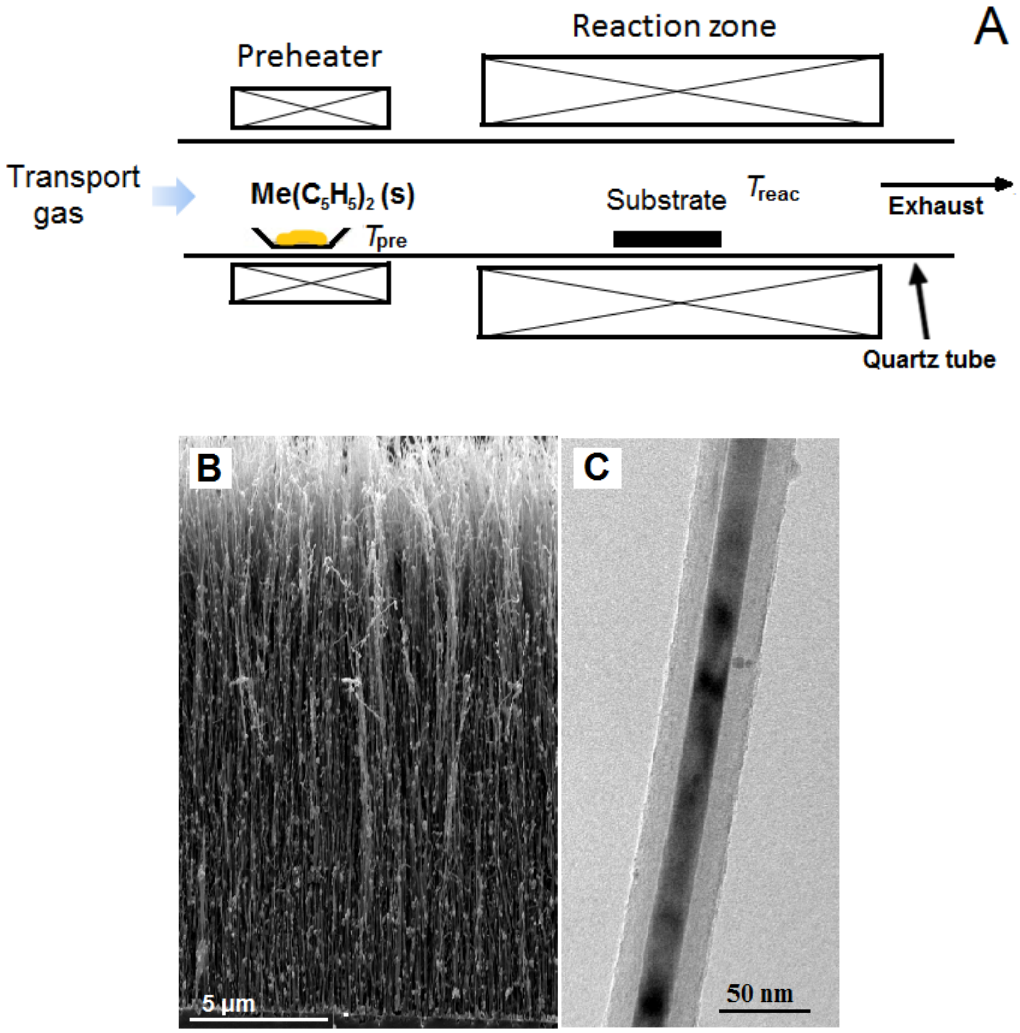

Figure 1.4: A typical two-zone reactor for the SSCVD (A). $T_{pre} > 170$ °C whereas T_{reac} between 750 and 1100 °C. SEM image of aligned Fe-MWCNTs arrays on the substrate (B). TEM image of an individual Fe-MWCNT showing contrast between the encapsulated Fe nanowire and the MWCNT (C).

The choice of sublimation temperature is important since it determines the sublimation rate and together with argon flow rate regulate the amount of metallocene that is transported into reaction zone. The concentration of the precursor is a decisive factor for the properties of the obtained material. The reaction temperature usually used for synthesis of the iron-filled carbon nanotubes varied between

750 and 1100 °C [24]. The deposition occurs on the substrates placed in the hot zone of the reactor as well as on the inner wall of the quartz tube. Commonly, silicon substrates with an upper thin SiO_2 layer and a thin metal layer on the top of the oxide layer are used in the synthesis processes. The role of the thin metal layer is to prevent oxygen diffusion into the nanotube walls and filling, although it can be omitted if the timescale for diffusion is much greater than the duration of the reaction at a given temperature. The most important aspects of the deposition process are nucleation and growth. Despite intense research activity since discovery CNT formation is not fully understood; the proposed models on nucleation and growth are outlined below.

1.3 Growth mechanism

Understanding the formation mechanisms of the carbon nanotubes is a key requirement for deliberate synthesis of tailored properties needed for a given application. Although, the formation mechanism of filled carbon nanotubes is still under discussion and further research is necessary, some experimental facts have been established. The growth of filled carbon nanotubes was found to be a catalytically controlled process, where the catalyst and the filling are identical. Tubular carbon nanotubes form by a vapour-liquid-solid (VLS) mechanism and it can be assumed that filled carbon nanotubes form by a similar mechanism. The VLS mechanism which was originally developed for the growth of silicon whiskers by Wagner and Ellis [40] consists of the assumption that carbon diffuses through a liquid metal particle, driven by concentration and temperature gradient. The

first mechanism to explain the growth of carbon nanotubes was developed by Baker et al [41]. He proposed a three stage growth mechanism model for the growth of carbon nanotubes (Figure 1.5).

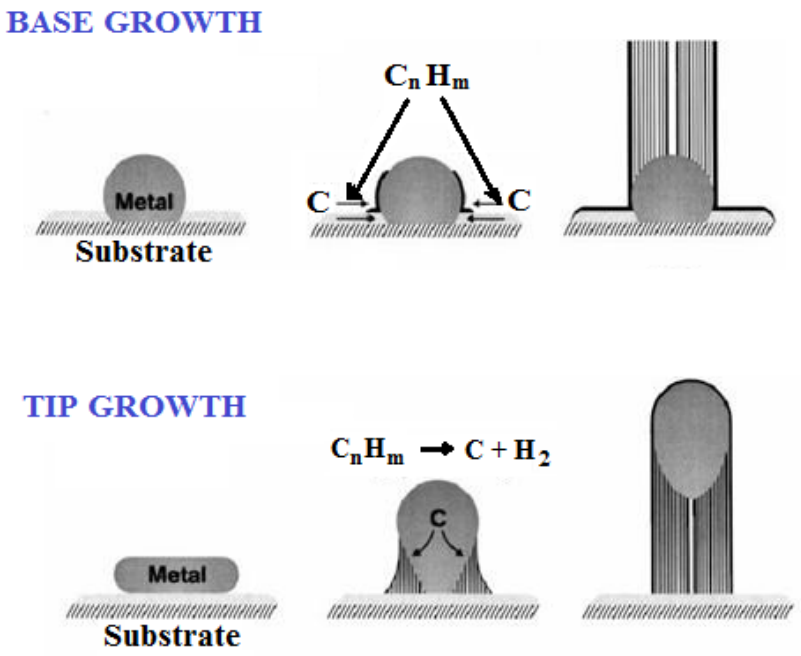

Figure 1.5: Base and tip growth mechanism of carbon nanotubes [42].

The first stage involves the decomposition of the hydrocarbons on the front of the surface of the metal particles, generating hydrogen and carbon that will dissolve into metal. The dissolved carbon will diffuse through the volume of the particle and will be deposited on the trailing face, forming the filament (second stage). After that the particle can remain attached on the substrate surface and the synthesis mode is called base-growth or the particle can detaches from the surface and lifts up forming the so-called tip growth mode. In this case the lifting particle can be observed on the top of the filament. The difference of growth modes is often explained in terms of contact force between the catalyst-particle

and the substrate. Evidently a strong interaction between the particle and the substrate promotes the base-growth mechanism whereas a weak particle – substrate interaction, favours the tip-growth.

In 1984 Gary Tibbetts explained why carbon filaments were tubular [43]. It was shown that the free energy required for the growth of a filament has a minimum value when graphite is in the form of a cylinder surrounding the metal. The inner core of the filament is hollow because inner cylindrical planes of small diameter would be highly strained and energetically unfavourable to form.

Another mechanism for CNTs growth was proposed by Nasibulin *et al.* which involves formation of carbon atom islands on the catalyst particle when the particle is supersaturated in C [44]. In this process, during CNT formation, competition between two fluxes of carbon atoms take place as presented schematically in Figure 1.6. The segregation flux of dissolved carbon atoms towards the particle surface and the diffusion flux of carbon atoms on the particle surface seeking their lowest energy states [44]. Due to the competition between the segregation and diffusion fluxes, two situations can occur in the system. First if the segregation flux is higher than the diffusion flux, initiation of CNT growth can occur. In this case nucleation process is likely to occur from islands where the segregation flux is larger. Second, when the segregation flux is lower than the diffusion flux, carbon will form the thermodynamically most stable system consisting of metal particles surrounded by graphitic layers.

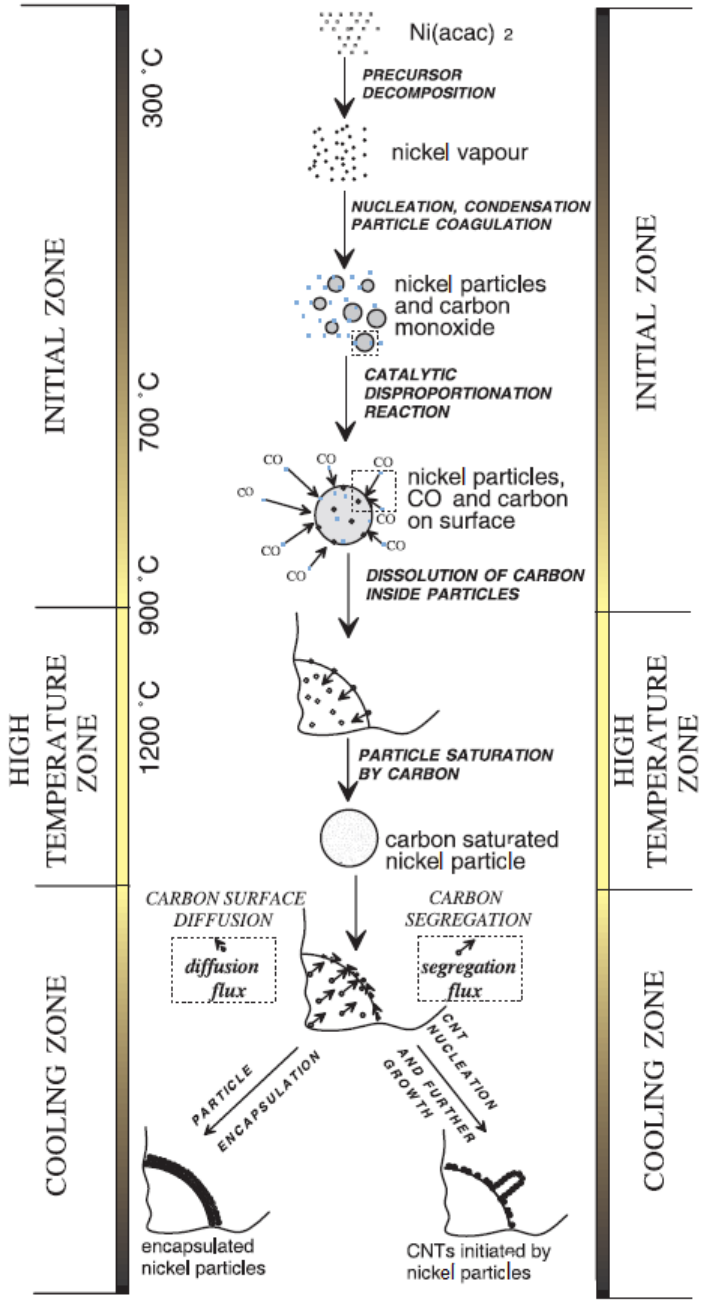

Figure 1.6: Schematic representation of CNTs formation mechanism consisting of nucleation and growth [44].

Several groups adjusted the VLS mechanism and the concepts of the tip and base growth mode to explain the formation of *in-situ* filled carbon nanotubes. Muller *et al.* proposed a growth mechanism knowing as open-ended base growth

for filled carbon nanotubes [18]. In this type of growth mechanism the nanotubes are open during the growth process and carbon is added at their open ends. The carbon nanotube growth starts from the decomposition of hydrocarbons on the metal surfaces and the diffusion of carbon atoms into the metal particles (Figure 1.7).

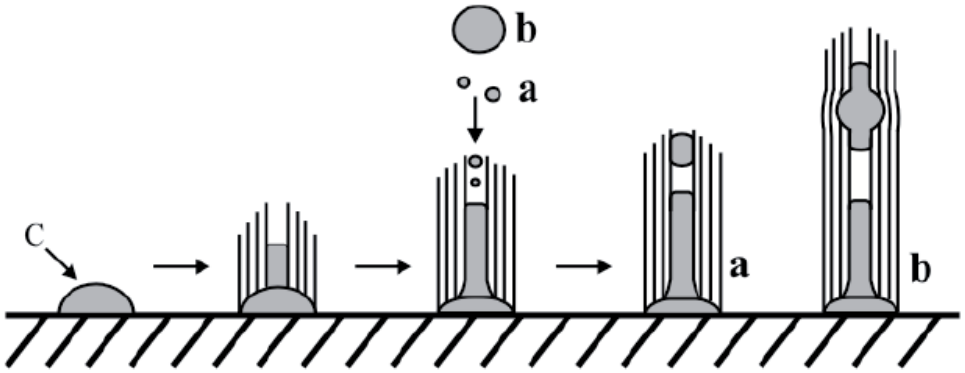

Figure 1.7: Schematic representation of the open-ended base growth mechanism [18].

Due to their small size and large amount of dissolved carbon the melting point of the metal particles is far below the melting point of bulk metal. This means that the catalyst particles are most likely in liquid state during the growth. When the carbon concentration exceeds supersaturation carbon shells precipitate from the catalyst particles. This is followed by an increase of the catalyst surface tension and the dissolution of carbon starts again. The layer by layer growth on the already grown inner tube layers occurs due to periodic fluctuations of the catalyst particle and fluctuations in the carbon concentration. During this process the initial catalyst particles remain fixed to the substrate surface, which corresponds to a base growth route. Simultaneously, during the CNT growth

metal particles with diameters in range of the inner tube diameter or smaller, can continuously accumulate at the open ends. The liquid-like particles can easily change their shapes, diffuse along the hollow core and contributes to an existing nanorod or form a new one. The closure of the tube will be observed when the growth rate decreases and finally stops. This can happen when a particle deposits on the open end and owing to the incorporation of pentagons and heptagons in the hexagonal carbon lattice, the high defect level leads to tube closure. Guo *et al.* suggested that additional carbon atoms, bridging the dangling bonds between carbon shells provide stability to the structure [45]. Also, Kwon *et al.* suggested that the covalent bonds between adjacent walls are highly favourable (lip-lip interactions) [46].

A combine growth mode for the metal-filled CNTs was presented by Kunadian *et al* [47]. They combined the tip- and base-growth mode explaining the formation of the filling in the context of a closed tip growth process. This mechanism (Figure 1.8) is based on the idea that the initial state follows the base growth mode. Hydrocarbons decompose on the surface of the catalyst particles. Due to the floating catalyst conditions metal clusters are formed and hydrocarbons can also decompose already in the gas phase. The catalytically active metal clusters and carbon atoms fall onto the catalyst particles that remain attached to the substrate surface. It was supposed that this results in a continuing change of the catalyst conditions. Each metal cluster that connects to the catalyst particle modifies volume, shape and the carbon concentration of the catalyst.

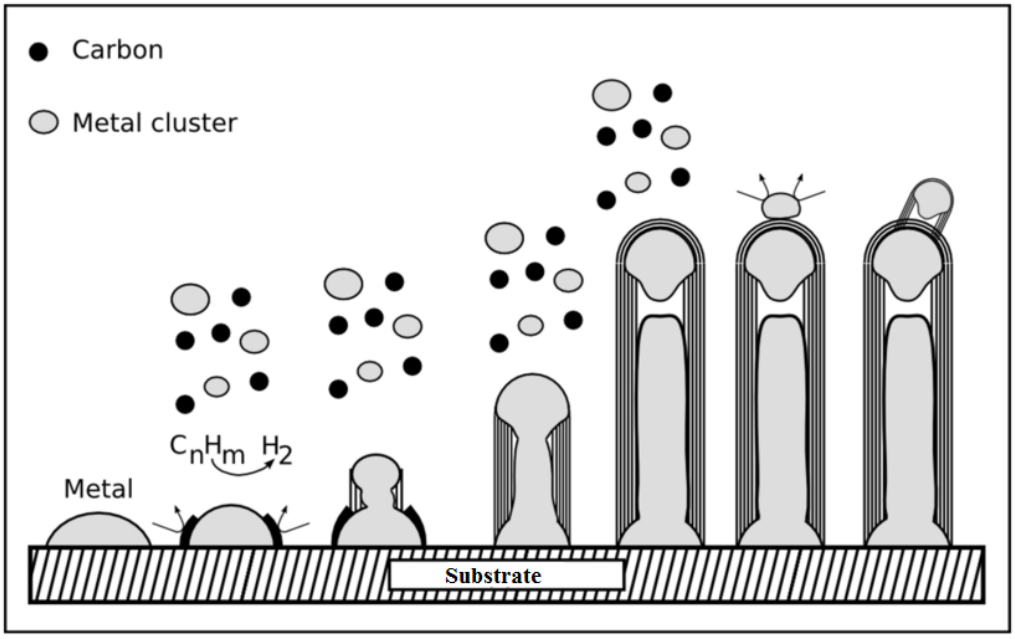

Figure 1.8: The combined base and tip growth mechanism [47].

Therefore under floating catalyst conditions it is likely that the growth mode switches from base to tip growth mode. After the switching the filling process as well as the shell formation occur simultaneously at the tip. When the CNT tip is closed by carbon layers, a secondary nucleation can take place and a further CNT can be formed on the existing material. These new CNTs are generally formed by tip growth mode because the interaction between the metal particle and the already existing CNT is low so the particles detach.

In all growth models described above the nanotube-nucleation and growth occurs from heterogeneously nucleated catalyst particles (catalyst particles are formed on the substrate surface).

Recently, Boi *et al.* reported radial structures that nucleate and grow from homogeneously nucleated particles in randomly fluctuating vapour created in the viscous boundary layer between a rough surface and a laminar pyrolyzed-

ferrocene/Ar vapour flow [26]. He proposed a three-stage formation mechanism in fluctuating metal–carbon vapour (Figure 1.9).

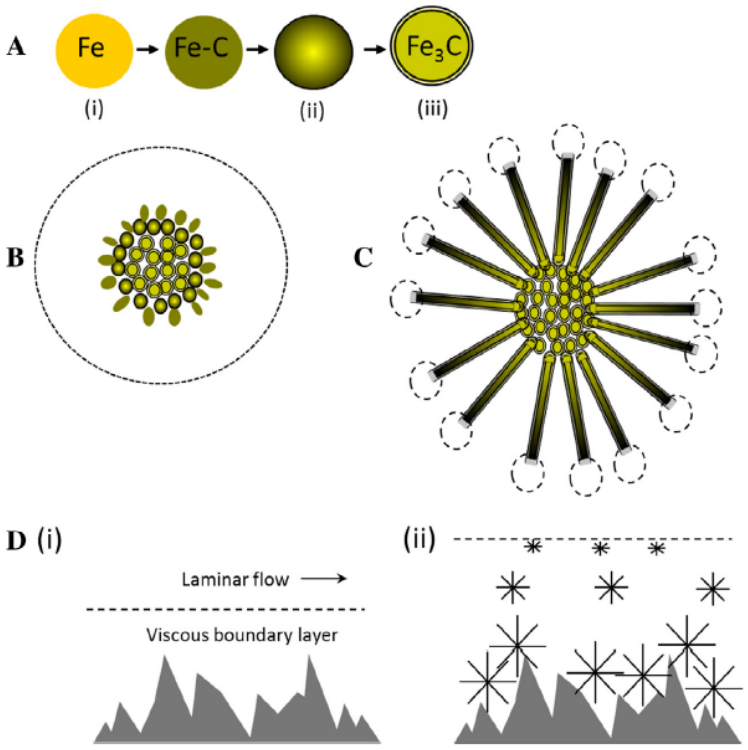

Figure 1.9: Growth mechanism of the radial structures [26].

In the first stage, Figure 1.9 A, the graphite-encapsulated Fe_3C particles spontaneously form by homogeneous nucleation of Fe or Fe-C particles in the viscous boundary layer region of the vapour. Carbon feedstock is driven to the particle by diffusion gradient and dissolves in the particle. When the rate of arrival carbon feedstock exceeds the rate of dissolution, the graphitic carbon shells form. After that (second stage), Figure 1.9 B, these spherical structures spontaneously agglomerate. The central particles are encapsulated (stage A (iii)) whereas the peripheral particles have no graphitic shell (stage A (i)). The spherical diffusion gradient created by the agglomeration results in an asymmetry in the vapour

feedstock for the peripherical particles which results in elongation and CNT nucleation. Finally, Figure 1.9 C, the lowest energy stable graphitic MWCNTs structures start to grow. The elongated particles are rapidly closed on the side of the agglomeration by graphitic shell formation, so the radial growth of the filled nanotubes is driven by the diffusion gradient established at the open tip. This tip growth must involve a temperature gradient exactly at the tip due to the endothermic nanotube formation.

In analogy with the radial structures, also Boi reported flower-like structures comprising MWCNTs that nucleate and grow from homogeneously nucleated particles [48]. The growth mechanism of flower-like structures is given in Figure 1.10.

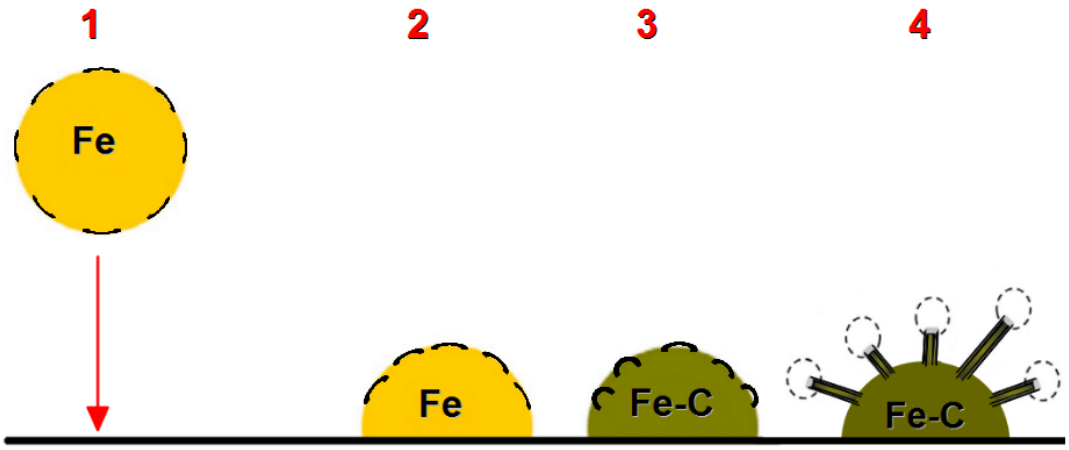

Figure 1.10: Schematic representation of the growth-mechanism of flower-like structures. The black solid lines represent the islands of C atoms formed in a spherical homogeneously nucleated particle (1) that assumes a cap-like shape after contact with the substrate [48].

A homogeneously nucleated Fe particle deposits from the vapour to the sub-

strate assuming the shape of a cap. The exposure to the C species in the vapour leads to the formation of some islands in the homegenously nucleated particle. The islands of C atoms formed in a spherical homogeneously nucleated particle are represented by the black solid lines in Figure 1.10. In this process two carbon fluxes must be taken into account: the segregation flux of dissolved carbon atoms towards the particle surface and the diffusion flux of carbon atoms seeking their lowest energy states [44]. If the segregation flux is higher than the diffusion flux, initiation of MWCNT growth can occur.

After a certain time of exposure to the vapour species (Fe and C) the particle will reach a certain Fe-C concentration and some caps will start to grow from islands of C atoms (Figure 1.10) in a mechanism similar to that previously mentioned in the case of SWCNT-nucleation [44, 49]. The nucleation of these caps will lead then to the nanotube growth-stage. The shape of each cap may change during this process leading to open-growth mode of the MWCNT. Boi proposed two possible open-growth mechanism modes: tip-growth and base-growth.

1.4 Dimensional and α-Fe content control of Fe-MWCNTs

Many studies have been conducted to achieve a complete control of the length and α-Fe content of Fe-MWCNTs. A continuous, completely α-Fe nanowire is desirable for some important applications, as is control of both nanowire and nanotube length and diameter. Although, the majority of effort has focussed

on encapsulation of elemental α-Fe, the most commonly observed encapsulated nanowires contain crystallites of α-Fe, γ-Fe, and Fe_3C [18,19,22-24]. Furthermore, in many reports, the nanowires are not continuous but comprise isolated 10-100s nm length crystallites with a much greater intermediate spacing.

The presence of γ-Fe, which transforms to α-Fe below 912 °C according to the standard Fe-C phase diagram, usually as a minority component is thought to result from suppression of the γ-α transition, which results in a 9% volume increase, by confinement of the internal nanowire by the high elastic modulus of the carbon nanotube walls ($\sim$1 TPa) [19].

It is known the decomposition of Fe_3C into α-Fe and graphitic carbon when in contact with a graphitic phase, at 600-750 °C [50]. Direct observation suggests that diffusion of carbon from the nanowire to the nanotube is rate-limited by an intermediate amorphous layer [19]. The presence of Fe_3C in the encapsulated nanowire is, therefore, the result of incomplete diffusion of carbon from within the nanowire to the junction with the nanotube. Consequently, to maximize the quantity of α-Fe, a post-synthesis heat treatment has been frequently considered which minimise the nanowire carbide content and provide the thermal energy to promote the γ-α transition [21, 51]. This annealing treatment was first reported by Leonhardt *et al.* [51]. They demonstrated that a post-synthesis heating treatment of 20 h could allow achieving a single phase of α-Fe at annealing temperature of 645 °C in an Ar/H_2 flow . However, this heat treatment at temperature 675 °C was accompanied by an unusual oxidation process leading to nanotube decomposition and α-Fe_2O_3 formation. In contrast, the work reported by Gui *et al.*

showed that after 15 h of annealing at 645 °C, large quantities of γ-Fe and Fe_3C were still found inside MWCNTs [21].

Boi *et al.* recently concluded that high vapour flow-rate ($\sim$100 ccm) promotes high α-Fe content as consequence of driving deposition into a higher temperature region of the reactor to promote C-diffusion and γ - α transitions but at the expense of poor nanowire continuity [52]. Numerous reports have addressed the question of poor nanowire continuity; Leonhardt *et al.* reported that continuity of is improved by simply increasing the zone-two (synthesis) temperature [14]. Shamsudin *et al.* observed that magnetic properties were highly dependent on changes of synthesis temperature [25]. In 2003, it was reported that continuous filling could be achievable by using high sublimation rates and high pyrolysis temperatures of ferrocene [17]. However, it was shown that higher filling rates than 40% are not achievable with SSCVD due to the fixed C/Fe ratio of each ferrocene molecule containing 10 atoms of C and only 1 atom of Fe.

Recently, Boi *et al.* reported radial Fe-MWCNT structures departing from a central particle synthesised in fluctuating, flowing vapour produced by the thermal decomposition of ferrocene. In this work they pointed out that continuous filling can be achieved in these radial structures due to the temperature gradient produced by hydrocarbon decomposition (exothermic) and graphitic carbon formation (endothermic) at an open tip as that which drives the feedstock to the active growth front when the vapour flow rate is low ($\sim$10 ccm) [26]. Although, they achieved the continuous filling, still the encapsulated nanowires contained crystallites of α-Fe, γ-Fe, and Fe_3C as commonly observed.

It is known that the nanowire diameter is proportional to that of the nucleating Fe particle and that diffusion of carbon from the nanowire feeds the growth of the nanotube so there is also a scaling of the number of nanotube walls (i.e. nanotube diameter) with encapsulated nanowire diameter [14,24]. Considering that the size of the catalyst particles fixes the diameter of the growing nanotubes, an increase in the ferrocene concentration would lead to a higher clustering rate of the catalyst particles and therefore to a larger single-crystals diameter [17]. The diameter of both the nanowires and nanotubes has been found to scale with the ferrocene evaporation temperature (zone one) close to the melting point temperature, but elevation to $\sim$ 400 ^{0}C results in vapour-phase nucleation of spherical particles which deposit on the exterior of the nanotube [16,53]. Independent control of these diameters was achieved either by *ex situ* nanotube filling or introduction of a chlorine-containing precursor and hydrogen [54, 55].

1.5 Magnetic properties of Fe-MWCNTs

Ferromagnetic nanowires exhibit unique and tuneable magnetic properties that are very different from those of the bulk ferromagnetic materials and spherical particles. To tailor the response of Fe-MWCNTs to a given application, the magnetic properties must be understood in detail.

The encapsulated iron nanowires usually contain crystallites of α-Fe, γ-Fe, and Fe_3C, but only α-Fe and Fe_3C exhibit ferromagnetic behaviour at room temperature. The γ-Fe is predicted to be paramagnetic at room temperature and antiferromagnetic at $T < 50$ K [12,13,56], whereas the graphitic carbon of MWCNT

walls is paramagnetic at room temperature and weakly diamagnetic at $T < 50$ K [57].

Hall magnetometry and magnetic force microscopy are the most used techniques to investigate the properties of individual Fe-MWCNTs which provide the detailed information on the magnetisation reversal process and the respective switching fields [4,22,23,58]. Whereas the magnetic behaviour of Fe-MWCNTs ensemble usually has been investigated by an alternating gradient magnetometer [4,13,51,56]. By using this method, typical hysteresis loops can be measured for an aligned array of Fe-MWCNTs deposited on the silicon substrate. The shape of the hysteresis loops is strongly influenced by the magnetic anisotropy since it controls the coersivity and remanence.

It is well known that ferromagnetic α-Fe nanowires possess uniaxial anisotropy with the easy axis aligned along the nanowire axis. The main origin of the magnetic anisotropy is shape anisotropy for long α-Fe nanowires since they have very low magneto-crystalline anisotropy (0.048 $\mathrm{MJm^{-3}}$) due to their cubic structure, leaving the shape anisotropy (0.96 $\mathrm{MJm^{-3}}$) as clearly dominating factor [23].

The opposite case, it is observed in the Fe_3C nanowires, where the magnetic easy axis is found to be perpendicular to the Fe_3C nanowire axis. Fe_3C has an orthorhombic crystal structure with strong magneto-crystalline anisotropy (3.94×10^5 $\mathrm{Jm^{-3}}$), which clearly dominates over the shape anisotropy (3.06×10^5 $\mathrm{Jm^{-3}}$) for a long Fe_3C nanowire) leading to a perpendicular magnetization [23]. As the two anisotropy contributions are in competition the resulting effective anisotropy is small, resulting in a low coercivity.

The saturation magnetization M_S and the coercivity H_C of Fe-MWCNTs can be tailored by modifying not only the amount of the filling material and ferromagnetic α-Fe fraction that is generally the dominating component, but also changing the length and the diameter of the encapsulated iron nanowire is an effective method of tuning magnetic properties. The saturation magnetization of a powder containing MWCNTs filled with α-Fe, γ-Fe and Fe_3C seems to be dependent mainly on the quantity of α-Fe [51,59]. Previous reports have shown that after annealing, the saturation magnetization of the powder increased owing to the higher quantity of α-Fe inside the MWCNT [51]. Whereas, the coercivity of Fe-MWCNTs appears to be strongly dependent on the degree of alignment [51], the shape anisotropy, the nanowire diameter, and the spatial-distribution of the ferromagnetic-phases inside the nanowire [12,13].

A key problem in the understanding the magnetism of the ferromagnetic nanowires is the diameter dependence of the coercivity. For iron nanowires, coercivity plotted as a function of the diameter exhibits a maximum at a critical value, the origin of which is explained within the next subsection.

1.5.1 Magnetism at the nanometre scale

In ferromagnetic materials two types of structure can be distinguished: single-domain (SD) and multi-domain particles (MD). MD particles consist of magnetic domains that are separated by domain walls. As the particle diameter decreases the formation of domain walls becomes energetically less favourable below a certain value. Below this critical diameter, the particle consists of a single domain

(SD). The distinction between SD and MD is straightforward. The magnetic properties like coercivity and remanence are strongly affected by the reduction in the particle diameter. The change in coercivity with the decrease in the particle diameter is shown in the Figure 1.11. As can be seen from the figure, the maximum coercivity for a given material occurs within the SD regime. For larger particle diameters, coercivity decreases as the particle subdivides into domains. For smaller diameters, coercivity again decreases, but this time due to the randomizing effects of thermal energy.

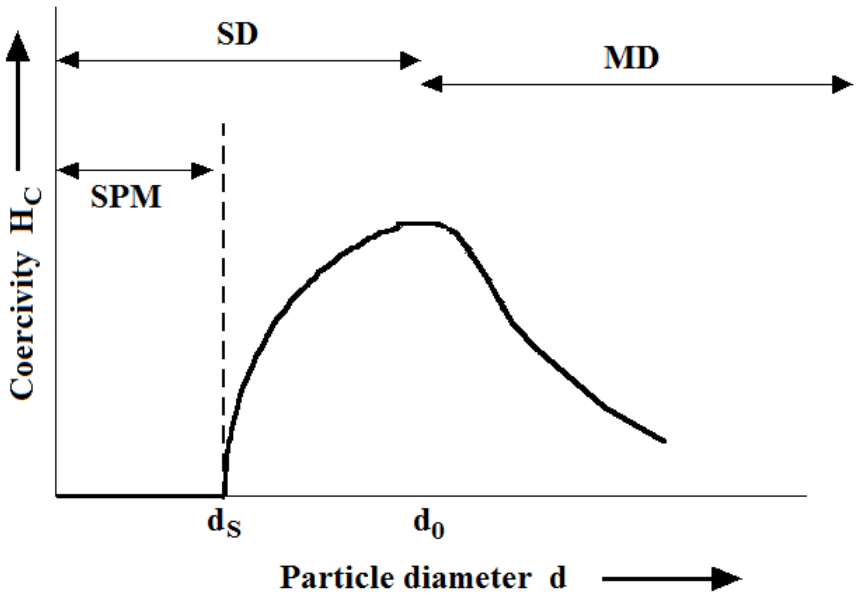

Figure 1.11: The effect of particle diameter on coercivity in ferromagnetic material [60].

The multi-domain particles are magnetically soft with low values of coercivity and remanence. Since the multi-domain particles have domain walls, magnetization reversal can be accomplished through domain wall displacement, an energetically easy process, which can be achieved in relatively low fields. In the case

of SD particles, to achieve magnetization reversal, the only way is to rotate the magnetization, an energetically difficult process. Thus, SD particles are magnetically hard and have high coercivities and remanence. If the particle diameter decreases within the SD regime, another critical threshold will be reached, at which the remanence and coercivity tend to zero. Below this critical diameter the particle becomes superparamagnetic.

1.6 Surface functionalization of carbon nanotubes

CNTs have potential applications in many aspects of biomedicine owing to the outstanding mechanical, optical, and electronic properties [4]. Various functionalization methods for tuning the properties to a given application have been developed. Magnetic functionalization has resulted in nanohybrids with desirable chemical, magnetic, and other physical properties for magnetic hyperthermia cancer therapy, contrast agents for MRI imaging, and magnetic carrier and drug delivery systems [4,5,9–11].

In addition to filling the central capillary of CNTs with magnetic nanostructures, benefits can be gained by surface functionalization of the inert sidewalls [27]. Generally, covalent and non-covalent modifications are frequently used to functionalize the CNT surface [28]. Covalent functionalization which is associated with the transformation of sp^2- into sp^3-hybridized bonding commonly is achieved by using both chemical modifications by strong acids and ultra-sonication pretreatments [27]. These treatments together alter the tube walls by introducing

considerable defects and dangling bonds where various functional groups (such as hydroxyl, carbonyl, carboxyl, *etc.*) can be covalently attached providing active nucleation site for loading of nanoparticles [61].

However, care has to be taken since strong acid treatment accompanied with sonication may result in severe damage to the sidewalls which can modify the physical properties [28]. Moreover, the properties of a sensitive filling material may be destroyed by treatment at high temperature, or strong pH values, required by some methods reported in the literature. For example, the saturation magnetisation of surface functionalized Fe-MWCNTs is dramatically lowered if functionalized via acid treatment because the iron is oxidised by the acid [9]. Also, the nanohybrids used as carriers for drug delivery or tissue engineering often contain sensitive organic moieties anchored on the carbon nanotubes which may be similarly damaged by strong pH values or by high temperature treatment [11].

In contrast, noncovalent functionalization is achieved by coating CNTs with amphiphilic surfactant molecules or polymers using various adsorption forces, such as the van der Waals force, hydrogen bonds, electrostatic forces, and π-stacking interactions [29-31]. Non-covalent functionalization has the advantage that it could be done under relatively mild reaction conditions so the integrity of the CNT and filling material can be maintained [28]. However, for biomedical applications, the use of polymers, surfactants or specific reactants could affect the biological response [11].

Many studies have been conducted to employ carbon nanotubes for MRI by in-

corporating paramagnetic gadolinium (Gd^{3+}) or superparamagnetic iron oxide nanoparticles into CNTs [4,62-67]. CNTs non-covalently functionalized with amphiphilic Gd^{3+} chelates was reported by Richard and co-workers [63]. Superparamagnetic iron-oxide nanoparticles attached to the surface of CNTs could act as T_2 contrast agent for MRI. A Gd^{3+}-conjugated ultra-short SWCNT nanocomposite was reported as a CNT-based MRI contrast agent by Sitharaman; the authors assumed that gadolinium ions occupied defects sites created on the tubes during a cutting step [62]. This type of Gd^{3+}-SWCNTs is high-performance MRI contrast agent [62]. Also, Sitharaman *et al.* reported gadolinium-catalyzed SWCNTs which exhibited both high R_1 and R_2 relaxation rate properties [68].

Chapter 2

Theoretical background

This chapter aims at laying the groundwork for understanding the observations and discussion thereof presented in this thesis. The theory behind CVD process including CVD growth rate model, boundary layer and the influence of the gas flow rate on control of CVD process are discussed in the first part of this chapter. A brief introduction into magnetic hyperthermia will be followed by heating mechanisms of magnetic nanoparticles in alternating magnetic field and physical limitations of magnetic hyperthermia for cancer therapy. The complete understanding of all physical and chemical parameters that influence relaxivity is crucial for desing new efficient MRI contrast agents. The final part of this chapter will describe the theoretical concepts behind gadolinium based contrast agents such as relaxivity of Gd^{3+} complexes and principal parameters for relaxivity optimization.

2.1 Theory of the chemical vapour deposition process

Chemical vapour deposition is a process whereby a solid material is deposited from a vapour by a chemical reaction occurring on or in the vicinity of a normally heated substrate surface [69]. The chemical reaction can be activated by heat (thermal CVD), UV radiation (photo-assisted CVD) or plasma (plasma-enhanced CVD) [70]. The crucial factor for control of the CVD process is that the role of process variables such as temperature, pressure, flow rate and input concentration on the reaction must be understood. By varying the experimental conditions — substrate temperature, gas flow rate, concentration of the reaction gas, total pressure gas flows, *etc.*— materials with different properties can be grown [69].

2.1.1 Gas flow and boundary layer

In the atmospheric-pressure thermally-activated CVD method gaseous reactants (or vapours obtained from the liquid reactants) are carried by an inert gas (H_2, N_2, argon or helium) and flow over substrates maintained at high temperatures in the reactor where the total pressure is 1 atm [71]. The main gas flow (the reaction gas mixture) that passes over the substrate surface undergoes a reaction at the substrate under the pre-determined conditions of temperature and pressure (T, P). From the fluid mechanics, in the case of the laminar flow, it is known that so-called boundary layers are developed near the substrate surface [72]. The boundary layers are defined as the region near the substrate surface where the gas

stream velocity, concentration of the vapour species and the temperature are not equal to those in the main gas stream. The gas velocity is zero at the substrate surface and increases to a constant value at some distance from the substrate [73]. The development of a velocity boundary layer in a laminar flow region is sketched in Figure 2.1.

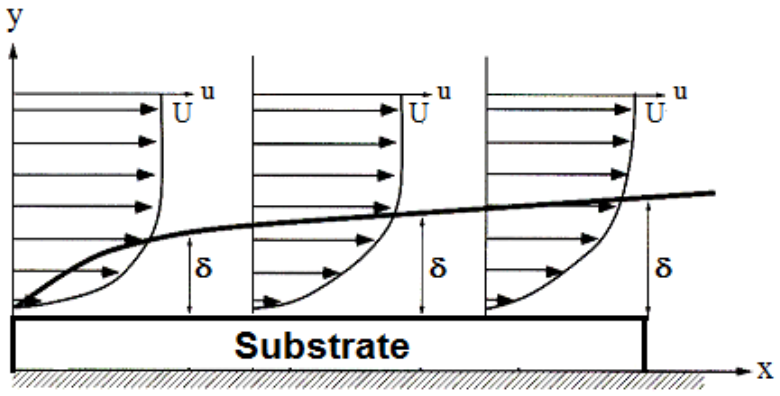

Figure 2.1: Boundary layer velocities along substrate. The δ is the thickness of the boundary layer. The boundary layer increases with distance in the direction of gas flow from Newton's second law [72].

The thickness δ of a boundary layer (laminar flow) at a position x on the substrate is given by:

$$\delta = a(\frac{\eta x}{\rho U})^{1/2}, \tag{2.1}$$

where a is a proportionality constant, η is the viscosity of the gas, U is the velocity of the gas and ρ is the density of the gas [72]. During the deposition process, the gaseous reactants and the gaseous reaction products are transported across this boundary layer by diffusion.

2.1.2 CVD growth rate model

The CVD process is developed according to the following steps: 1 - transport of reactant gases to the vicinity of the substrate; 2 - intermediate reactants form from reactant gases; 3 - diffusion of the reactants species through boundary layer to the substrate surface; 4 - reactant adsorption on the substrate surface; 5 - single or multi-step surface chemical reaction; 6 - desorption of product gases from the surface substrate; 7 - diffusion of the reaction products away from the substrate surface and 8 - transport of reaction products outside by the bulk gas flow [73]. Since all these steps occur sequentially, the slowest will be the rate determining step. Depending on the rate - determining step there are three control types of the CVD process: mass transport of first type, mass transport of second type and surface kinetics.

Mass transport of first type is an equilibrium process determined by mass input and occurs when step 1 or 8 (i.e. the reactant supply to the deposition zone or reaction product removal from the deposition zone) are the slow steps. Mass transport of second type is a process determined by diffusional mass transfer which occurs when step 3 or 7 (i.e. reactant transfer between the main gas flow and the substrate through the boundary layer, which usually occurs by diffusion or convection) are the slow steps.

Kinetic control, also called surface kinetics or chemical reaction control, implies that the rate – determining step is a surface process which occurs when one of steps 4 (reactant adsorption), 5 (chemical reaction), or 6 (product desorption) is a slow step. At lower temperature the deposition rate is generally surface

reaction limited. As the temperature increases (>700 °C), the surface reaction rate increases exponentially, resulting in the mass transport limited since the mass transport becomes the slowest step [71].

Overall, a CVD reaction can be categorized as either surface kinetics or mass transport controlled, Figure 2.2 [74].

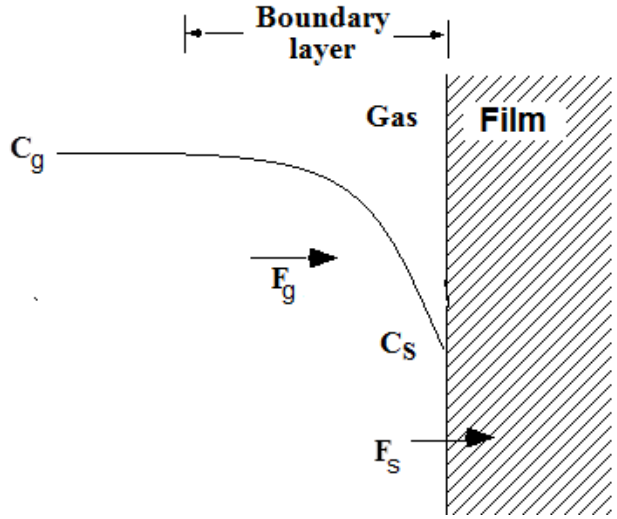

Figure 2.2: Schematic diagram of the growth process model [74].

There in a CVD process are two fluxes of the reactant species that coexist: flux of the reactant species through the boundary layer and the flux of the reactant species consumed in the film. The equations for these fluxes are given by:

$$F_g = h_g(C_g - C_s), \tag{2.2}$$

$$F_s = k_s C_s, \tag{2.3}$$

where the F_g is the flux of reactant species through the boundary layer, F_s is reactants flux consumed by reaction taking place at the surface of the growing film. The h_g is mass transport coefficient, k_s is the surface reaction constant, C_g

is bulk reactant concentration and C_s is reactant concentration at the substrate surface [73].

$$h_g = \frac{D_g}{\delta}, \tag{2.4}$$

where D_g is diffusivity of reactants in gas and δ is boundary layer thickness. In steady state conditions $F_g = F_s = F_{total}$, so

$$C_s = \frac{h_g C_g}{h_g + k_s}. \tag{2.5}$$

The total flux can be written:

$$F_{total} = (\frac{h_g k_s}{h_g + k_s})\ C_g. \tag{2.6}$$

Mathematically, three regimes arise: $h_g \gg k_s$, $h_g \sim k_s$ (mixed region), and $h_g \ll k_s$. If $k_s \gg h_g$ the process is mass transport controlled where low gas transport rate through the boundary layer limits the rapid surface reaction. In the case where $h_g \gg k_s$ (C_s approaches C_g) surface reaction control dominates, it is slow even though sufficient reactant gas is available. Additionally, surface kinetics control is ready achieved at low temperature, low pressure, low concentration of reactants and high gas flow rate. At high temperatures, under atmospheric pressure CVD (APCVD) conditions, mass transport is rate limiting *($h_g \ll k_s$)*. In these conditions total flux approximately can be written:

$$F_{total} \sim h_g C_g. \tag{2.7}$$

Since the growth rate is proportional to the total flux, in this case as it can be seen from Equation 2.7, it is also proportional to bulk reactant concentration C_g. By varying process variables the deposition process can be either limited by gas phase diffusion to the substrate surface or by reaction at the substrate.

2.1.3 Influence of the gas flow rate on control of a CVD process

Rapid deposition growth rates are dependent on the optimizing the flow of reactants through the system and the substrate [74]. Film growth rate can be expressed as a function of gas flow rate, which is outlined in Figure 2.3. The plot manifests the square root dependence of growth rate on flow rate. However, there is a point where the growth rate saturates and becomes independent of the flow rate, which means no matter how much the flow rate is increased it cannot anymore affect the film growth rate. Once this happens, surface reaction takes over the control of deposition.

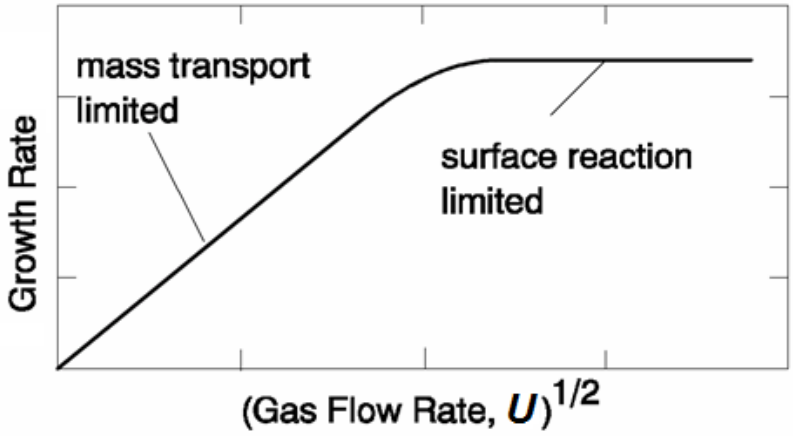

Figure 2.3: Dependence of the growth rate on the gas flow rate [69].

At low flow rates the gas stream has a sufficient residence time to equilibrate with the substrate surface. The reaction rate in this region is controlled by mass transport of the first type which, as mention above, is an equilibrium process determined by mass input. In this region the CVD rate increases linearly with total flow rate and the maximum efficiency will be attained. At medium flow

rate, the reaction rate is controlled by mass transport of second type, a process determined by diffusional mass transfer. In this region the CVD rate increases non-linearly with total flow rate and the process efficiency is lowered because of the conditions of an incomplete equilibrium a portion of the reactant will pass unreacted over the substrate. Whereas, at high flow rates, the reaction rate is controlled by surface kinetics becoming independent of the flow rate because the reactant partial pressure in the surface region is maintained constant. In this regime we have the highest deposition rate but the lowest efficiency of the process.

2.2 Magnetic hyperthermia

Magnetic hyperthermia is a cancer treatment method which uses the localized heat generated by magnetic nanoparticles in an alternating magnetic field to treat and destroy the cancer cells. It is based on the enhanced sensitivity of cancer cells to elevated temperature. By heating cancer tissues from 42 to 46 °C, cancerous cells can be damaged without much harm to the healthy surrounding tissue [1,75]. Penetrating the tumour tissue with magnetic nanoparticles, followed by application of an alternating external magnetic field, leads to controllable heating of the target tissue area, resulting in death of the cancer cells.

The majority of the current research is focused on the superparamagnetic iron oxide nanoparticles which have proven their feasibility in animal experiments [75] and are now under clinical trials [1]. However, metallic iron nanowires can produce heat more efficiently than superparamagnetic iron oxides due to their

particular magnetic properties, i.e. high coercivity and saturation magnetisation. The use of iron nanowires is hindered by oxidation in a biological environment. A possible solution of this problem is the use of iron nanowires encapsulated by carbon nanotubes. The carbon shells efficiently protect encapsulated iron from biological environment while its magnetic properties are maintained [4,56].

The most common parameters used to compare effectiveness of heating performed with different materials are the specific absorption rate (SAR) and the intrinsic loss power (ILP) [76,77].

SAR represents mass normalized rate of energy absorption. It is measured in watts per gram and can be determined according to equation:

$$\mathrm{SAR} = \frac{P}{m_{\mathrm{MNP}}} = c\frac{dT}{dt}|_{t\to 0}, \tag{2.8}$$

where P is the heating power measured in watts, m_{MNP} is the mass of the magnetic nanoparticles measured in grams, c is the specific heat capacity of the sample and dT is the temperature rise during the time interval dt.

ILP is an intrinsic parameter based on the heating capacity of the material that is measured in $\mathrm{Hm^2g^{-1}}$ and expressed by the equation:

$$\mathrm{ILP} = \frac{\mathrm{SAR}}{fH^2}, \tag{2.9}$$

where f and H are the frequency and the magnetic field strength respectively. The value of SAR depends on several factors related to materials (shape, size, composition) and external AC magnetic field (frequency, amplitude) whereas the ILP is an intrinsic parameter that depends only on the factors related to the materials used. The ILP is a system-independent parameter, designed to allow

more direct comparisons to be made between experiments performed in different laboratories and under different AC field strength and frequency conditions [76].

2.2.1 Heating mechanisms

There are several mechanisms for heating of magnetic particles in alternating magnetic fields: ferromagnetic (hysteresis) losses, superparamagnetic (relaxation) losses, eddy currents [78,79]. In comparison to magnetic losses, eddy current induced heating of magnetic particles used for hyperthermia is negligibly small [77].

Hysteresis losses appear in ferromagnetic particles which possess hysteretic magnetic properties when exposed to an alternating magnetic field. In this case, the alternating magnetic field induces magnetisation reversal that causes dissipation of energy. The dissipated power P_{FM} can be determined by multiplying the frequency f of the alternating magnetic field with the area of the hysteresis loop:

$$P_{\mathrm{FM}} = \mu_0 \, f \oint H \, dM. \tag{2.10}$$

In the particular case of single domain particles, no minor loops can be utilized for heating, so the hysteresis losses occur only if the external field exceeds the coersivity field, otherwise no reversal of the magnetic moments and consequently no losses occur. As is evident from Equation (2.10) the maximum realizable P_{FM} should involve a rectangular hysteresis loop. Single domain particles with uniaxial anisotropy and perfectly aligned with H, will dissipate the highest amount of hysteresis energy that can be expected. In the case of multi-domain particles, reversal of the magnetisation direction takes place via magnetic domain wall dis-

placement and the hysteresis energy is comparatively low since it takes relatively little field energy to make the domain walls move.

Superparamagnetic or relaxation loss is an alternative mechanism for magnetically induced heating in an alternating magnetic field. The term superparamagnetism was introduced by Elmore to describe the magnetic behaviour of colloidal systems containing iron oxide particles [80]. When such a colloidal system is removed from a magnetic field, its magnetization relaxes back to zero due to the thermal energy. This relaxation of the magnetization can be either associated with the physical motion of the particles (Brownian relaxation) or with the rotation of the magnetic moment within each particle (Néel relaxation) [77-79]. Both kinds of relaxation lead to the dissipation of the magnetic field energy and also have a characteristic Brown and Néel relaxation times that are given by:

$$\tau_{\mathrm{B}} = \frac{3\eta V_{\mathrm{H}}}{kT} \qquad \text{and} \qquad \tau_{\mathrm{N}} = \frac{\sqrt{\pi}}{2}\tau \, \frac{exp(\frac{KV}{kT})}{\sqrt{\frac{KV}{kT}}}, \tag{2.11}$$

where η is the viscosity of the medium, V_{H} is the hydrodynamic volume of the particle, (kT) is the thermal energy while V is the magnetic volume of particle, K the anisotropy constant and τ is the attempt time ($\tau \sim 10^{-9}$ s). When Néel and Brown relaxation processes occur in parallel, the characteristic relaxation time τ_{R} is given by the following equation:

$$\frac{1}{\tau_{\mathrm{R}}} = \frac{1}{\tau_{\mathrm{N}}} + \frac{1}{\tau_{\mathrm{B}}}. \tag{2.12}$$

Considering non-interacting superparamagnetic particles, the dissipated energy P_{SPM} in the alternating magnetic field of amplitude H and frequency f can be

determined by:

$$P_{\mathrm{SPM}} = \mu_0 \, \pi \, f \, \chi'' \, H^2, \tag{2.13}$$

where μ_0 is the permeability of free space and χ'' is the imaginary part of the complex magnetic susceptibility, χ. The out-of-phase χ'' component is frequency dependent and is given by the expression:

$$\chi''(f) = \frac{\chi_0 f\tau}{1+(f\tau)^2} \qquad \text{with} \qquad \chi_0 = \frac{\mu_0 M_{\mathrm{S}}^2 V}{kT}, \tag{2.14}$$

where the M_{S} is the saturation magnetization and τ is the characteristic relaxation time.

Physically, Equation (2.13) implies that if the M lags H there is a positive conversion of magnetic energy into internal energy [77].

2.2.2 Constraints on the choice of alternating field amplitude and frequency

Both heat mechanisms discussed above show that SAR is an increasing function of frequency f and field amplitude H. However, enhancement of SAR by increasing f and H is limited mainly for medical reasons. The frequency and strength of the externally applied alternating magnetic field used to generate the heat is limited by deleterious physiological responses to high frequency which includes stimulation of peripheral and skeletal muscles, possible cardiac stimulation and arrhythmia [81,82].

Also, the alternating magnetic field for heating up particles inside the patient body not only damages the cancerous tissues but also can cause an unwanted

non-selective heating of healthy tissue due to induction of eddy currents in the patient body [82]. The induced heating power according to the induction law is proportional to the square of *(H·f·D)* where H is the field amplitude, f frequency and D is the coil diameter. Generally, the usable range of the amplitude and frequency is considered to be $H = 0$ - 15 kAm^{-1} and $f = 0.05$ - 1.2 MHz [72].

In an experimental study, it was found that for a coil diameter of 30 cm, test patients were able to withstand the treatment for more than one hour without major discomfort if the product *(H·f)* did not exceed 4.85 $\times 10^8$ Am^{-1}s^{-1} [83]. This limit might be exceeded by a factor of ten for the smaller coil typically around 10 cm. Based on this it was suggested a limit for the acceptable product of frequency and amplitude of 5×10^9 Am^{-1}s^{-1} [84].

Pankhurst *et al.* stated that the eddy current threshold is the limiting threshold for frequency beyond several hundred kHz, the typical frequency range of the alternating magnetic fields for hyperthermia-based cancer therapy [85]. An appropriate combination of H and f resulting in maximum heating power has to be chosen taking into account the magnetic properties of the particles used.

To exploit heating potential of ferromagnetic particles, a frequency of several hundred kHz and a relatively high field amplitude that exceeds the coersive field (*circa* 100 kAm^{-1}) is required, since at this field strength the hysteresis loop is fully saturated. Only minor hysteresis loops can be utilized owing to the medical constraint of *circa* 15 kAm^{-1}, resulting to low SAR [77].

In case of superparamagnetic particles considering the Néel relaxation model valid for high frequencies, they are capable to generate impressive levels of heating at

relatively high field frequency (more than several hundred kHz) but with rather low field amplitude (several kAm^{-1}) since magnetic energy $E_{\mathsf{m}} = \mu_0 \cdot M \cdot H \cdot V$ must be smaller than thermal energy $E_{\mathsf{t}} = kT$; a condition which does not hold for large field amplitude [84].

2.3 Contrast agents for magnetic resonance imaging

Magnetic resonance imaging is one of the most important tools in clinical diagnostics and biomedical research. It is based on nuclear magnetic resonance and measures the relaxation rate of water proton spins exposed to a magnetic field. The term relaxation describes the numerous processes by which nuclear magnetization prepared in a non-equilibrium state, returns to the equilibrium distribution. The observed signal intensity in MRI depends on a number of factors that include proton density, T_1 and T_2 relaxation times, magnetic susceptibility and field gradient. The contrast primary arises from the local value of the longitudinal relaxation rate of water protons ($\frac{1}{T_1}$) and the transverse relaxation rate ($\frac{1}{T_2}$) [86]. Also, signal intensity tends to increase with increasing $\frac{1}{T_1}$ and decrease with increasing $\frac{1}{T_2}$.

Contrast agents (CA) have been frequently used to enhance the image contrast by reducing T_1 and/or T_2 relaxation times of surrounding water protons [86]. They reduce T_1 or T_2 in tissue by affecting the amplitude and time scale of magnetic field variation experienced by water molecules. MRI contrast agents in clini-

cal use are in the form of either paramagnetic complexes or superparamagnetic nanoparticles [87,88]. Paramagnetic complexes, which are usually gadolinium (Gd^{3+}) chelates, reduce the T_1 relaxation time to yield brighter images where localized [89]. Whereas, superparamagnetic agents based on iron-oxide nanoparticles reduce the T_2 relaxation time which produces darker images [89]. Advances in MRI have strongly favoured T_1 agents and thus Gd^{3+} complexes.

The efficiency of an MRI contrast agent is expressed in terms of its relaxivity ($r_{1,2}$) which describes the change in the relaxation rate of water protons per millimolar (mM) concentration of a given contrast agent.

As the paramagnetic contrast agents the lanthanide ion, Gd^{3+}, is usually chosen for MRI due to its peculiar magnetic properties. It has seven unpaired f-electrons, the greatest number of unpaired electrons exhibited by any atom or ion, a large magnetic moment ($\mu^2 = 63\mu_B^2$) and a symmetric electronic ground state,$^8S_{7/2}$. Accordingly, these ions form strong local magnetic fields and protons of water molecules near these ions experience a sufficient reduction in the relaxation time. As many rare earth metals, Gd^{3+} is a toxic material, consequently, it is crucially important that Gd^{3+} should be strongly attached to a chelate to avoid its toxic effects [90]. Indeed, chelated Gd^{3+} ions results in a complex that may be non-toxic, with improved bio-distribution but usually with a diminished ability of Gd^{3+} ion to affect the relaxation rate of water protons [90]. The clinically used Gd^{3+} complexes such as gadolinium-diethylenetriamine pentaacetic acid (Gd-DTPA), gadolinium-tetraazacyclododecanetetraacetic acid (Gd-DOTA) and their derivatives have low relaxivities with r_1 values of only 4-5 $mM^{-1}s^{-1}$ [91]. Furthermore,

the clinical applications of many macromolecular contrast agents are limited due to the potential toxicity of free Gd^{3+} ions released due to instability of Gd^{3+}-contrast agents [92,93]. Therefore, further development of contrast agents with high relaxivity and low toxicity are crucial for the early accurate diagnosis of the pathological tissues. Increasing relaxivity would enable contrast-enhanced MRI to be performed at lower doses and may lower the risk of gadolinium - induced toxicity.

Also, currently, the most efficient T_1 agents show a typical high-field relaxivity peak centred at 30–40 MHz (0.7 - 0.94 T) [94]. Above this frequency, the relaxivity quickly vanishes to very small values.

The need for higher spatial resolution, higher speed imaging and better sensitivity led to the development of clinical high-field MRI systems. The routine clinical use of 3 T MRI systems has raised the demand for MRI contrast agents working at this field or above. High magnetic field strengths of 9.4 T and 11.7 T are routinely used in pre-clinical small animal studies because of the major advantage of increased sensitivity of detection that translates to improve spatial resolution and higher spectral dispersion for resolving peaks [90].

New contrast agents need to be specifically tailored to fully exploit the benefits of high-field MRI. The design of new, more efficient MRI contrast agents requires the complete understanding of all factors and mechanisms that influence proton relaxivity, hence efficiency of Gd^{3+} complexes.

2.3.1 Relaxivity of Gd^{3+} complexes

The observed water proton longitudinal relaxation rate in a solution containing a paramagnetic Gd^{3+} complex is given by the sum of three contributions:

$$R_1{}^{obs} = R_1{}^{w} + R_{1p}{}^{is} + R_{1p}{}^{os}, \tag{2.15}$$

where $R_1{}^{w}$ is the water relaxation rate in the absence of the paramagnetic Gd^{3+} complex, $R_{1p}{}^{is}$ represents the contribution due to exchange of water molecules from the inner coordination sphere of the Gd^{3+} ion to the bulk water and $R_{1p}{}^{os}$ is the contribution of solvent molecules diffusing in the outer coordination sphere of the paramagnetic centre [95-97].

The overall paramagnetic relaxation enhancement ($R_{1p}{}^{is} + R_{1p}{}^{os}$) referred to by a 1 mM concentration of a given Gd^{3+} chelate is called its relaxivity.

A schematic representation of two relaxation mechanisms operating the relaxation enhancement of the water protons in solution by Gd^{3+} complexes is shown in Figure 2.4.

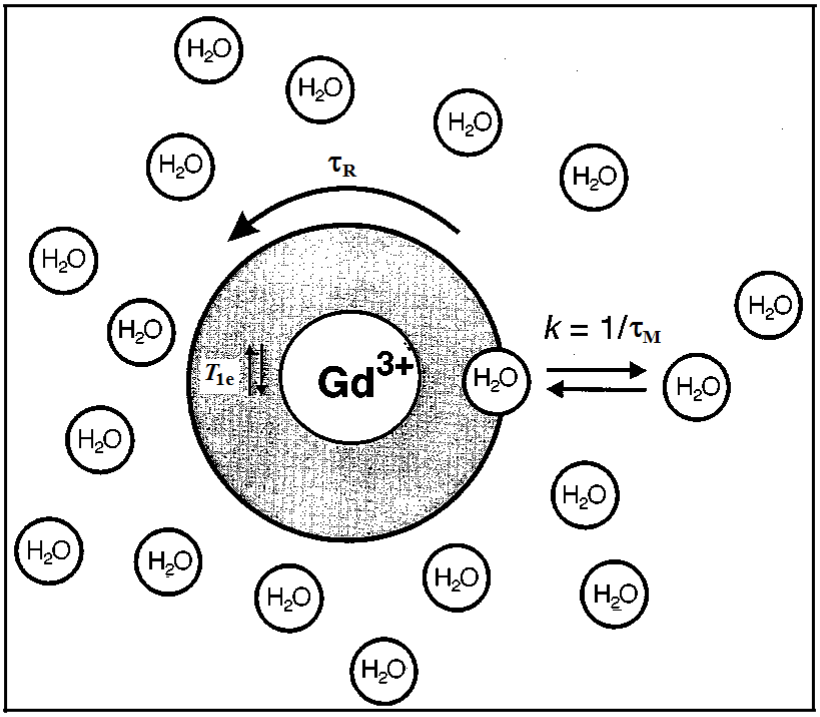

Figure 2.4: A schematic view of a Gd^{3+} complex with one inner sphere water molecule surrounded by bulk water. Inner sphere proton relaxivity is due to interaction between the Gd electron spin and the water protons on the inner-sphere water. Outer sphere relaxivity arises from interaction between the Gd electron spin and bulk water. τ_R is the rotational correlation time of the molecule, T_{1e} is electron spin relaxation time, τ_M is the residence lifetime of coordinated water molecules and k stands for water/proton exchange rate [98].

Inner-Sphere Relaxation - The longitudinal relaxation contribution from the inner-sphere mechanism results from the chemical exchange of the coordinated water protons with the bulk as shown in Equation (2.16):

$$R_{1p}{}^{is} = \frac{cq}{55.6} \frac{1}{T_{1M} + \tau_M}, \tag{2.16}$$

where c is the molar concentration of the Gd^{3+} complex, q is the number of water molecules coordinated to the Gd^{3+} ion, τ_M is the mean residence lifetime of coordinated water molecules and T_{1M} is their longitudinal relaxation time [95,96,99]. The relaxation of bound water protons is governed by the magnetic field dependent dipole-dipole and scalar or contact mechanism. The dipole-dipole interaction is modulated by reorientation of nuclear spin-electron spin vector, by electron spin relaxation and by water proton exchange. The scalar interaction is influenced by electron spin relaxation and water exchange and generally it represents a small contribution [100]. The value of T_{1M} which represent the sum of dipolar (through-space) and scalar, or contact (through-bonds) contributions is given by the Solomon-Bloembergen (SB) equations :

$$\frac{1}{T_{1M}} = \frac{2}{15}\frac{\gamma_I^2 g^2 S(S+1)\beta^2}{r^6}\left[\frac{7\tau_c}{(1+\omega_s^2\tau_c^2)} + \frac{3\tau_c}{(1+\omega_I^2\tau_c^2)}\right] + \frac{2}{3}\frac{S(S+1)A^2}{\hbar^2}\frac{\tau_e}{1+\omega_s^2\tau_c^2}, \tag{2.17}$$

where γ_I is the proton gyromagnetic ratio, g is the electronic g-factor, S is the total electron spin of the Gd^{3+} ion, β is the Bohr magneton, r is the proton-Gd^{3+} ion distance, ω_S and ω_I are the electronic and proton Larmor precession frequencies respectively, and A/h is the electron-nuclear hyperfine coupling constant [101, 102]. The dipolar and scalar relaxation mechanisms are modulated by the correlation times τ_c and τ_e, as given by equations 2.18 and 2.19:

$$\frac{1}{\tau_c} = \frac{1}{T_{1e}} + \frac{1}{\tau_M} + \frac{1}{\tau_R}, \tag{2.18}$$

$$\frac{1}{\tau_e} = \frac{1}{T_{1e}} + \frac{1}{\tau_M}, \tag{2.19}$$

where T_{1e} is the longitudinal electron spin relaxation time, τ_M is the water residence time as mentioned above, and τ_R is the rotational tumbling time of the entire Gd^{3+} ion- water unit. For S > 1/2 ions, collisions between the complex and solvent molecules are thought to induce distortions from octahedral symmetry that lead to transient zero-field splitting (ZFS) of the electronic spin levels. Electronic relaxation occurs due to this ZFS modulation, with $1/T_{1e}$ given by equation 2.20:

$$\frac{1}{T_{1e}} = B\ [\frac{\tau_\nu}{(1+\omega_s^2\tau_\nu^2)} + \frac{4\tau_\nu}{(1+4\omega_s^2\tau_\nu^2)}], \tag{2.20}$$

where the constant B is related to the magnitude of the transient ZFS and τ_ν is the correlation time characterizing the fluctuations. The inclusion of this expression in the standard SB approach constitutes the Solomon-Bloembergen-Morgan (SBM) equations. The inner sphere relaxivity in the high magnetic field region is mainly controlled by the rotational correlation time, τ_R, which mainly depends upon the molecular dimension of the complexes, as shown by the good correlation between relaxivity and molecular weight for a number of structurally similar complexes [98]. The Solomon-Bloembergen-Morgan theory predicts that an increase in τ_R by slowing the molecular tumbling of the contrast agent in solution will results in an increase in relaxivity. At low field, electronic relaxation time usually dominates inner sphere relaxivity.

Outer-Sphere Relaxation - The outer-sphere contribution to solvent relaxation has received less attention than the inner sphere mechanism. The most general form of the theory for outer-sphere relaxivity incorporates the effects of fluctuations due to electronic relaxation as well as that due to translational diffusion.

Bulk solvent molecules diffusing around the paramagnetic centre also experience the paramagnetic effect. The outer-sphere relaxivity, which depends on the electronic relaxation time of the Gd^{3+} ion, on the distance of closest approach of solute and solvent (d) and on the sum of solvent and solute diffusion coefficients (D) is usually treated on the base of the set of equations developed by Freed [103]. These set of equations have some similarity with the SB equations, with the longitudinal relaxivity given by equation 2.21 :

$$(\frac{1}{T_1})_{OS}=\frac{C\pi N_S\gamma_I^2\gamma_S^2\hbar^2S(S+1)}{d^3\tau_D}[7I(\omega_s\tau_D\,T_{1e})+3I(\omega_I\tau_D\,T_{1e})], \tag{2.21}$$

where C is a numerical constant, N_S is the number of Gd^{3+} ions per cubic centimetre and τ_D the relative translational diffusion time, is given by:

$$\tau_D = \frac{d^2}{3(D_I + D_S)}, \tag{2.22}$$

where D_I and D_S are diffusion coefficients of water and the Gd^{3+} complex, respectively. (Note the other symbols have their usual meaning as described above.) Diffusion coefficients can be estimated if the motion is described by the diffusion of rigid spheres in a medium of viscosity η as shown in equation 2.23:

$$D = \frac{kT}{6\pi a\eta}, \tag{2.23}$$

where a is the molecular radius.

Since the outer sphere contribution to relaxivity can hardly be modified, the development of high relaxivity contrast agents mainly involves increasing the inner sphere term.

2.3.2 Principal parameters for relaxivity optimization

There are several major physical and chemical parameters that can affect relaxivity such as: the number of coordinated water molecules directly to the Gd^{3+} ion (q), distance between the water protons and the unpaired electron spin (r), rotational correlation time (τ_R), electron spin relaxation time (T_{1e}) and the residence lifetime of coordinated water molecules (τ_M). These parameters might be optimized to enhance the efficiency of paramagnetic agents and thereby minimize the effective dose. The parameters q and r are important in governing the strength of the electron-nuclear dipolar interaction, whereas τ_R and T_{1e} determine the time scale of the fluctuations in the unpaired electron′s magnetic field at the nucleus. Finally τ_M can be important in modulating the efficiency of the chemical exchange of water between complex-bound and bulk environments.

Number of coordinated water molecules (q) - As indicated by equation 2.16 relaxivity is highly dependent on the number of coordinated water molecules. Gadolinium ions themselves have $q = 9$ in aqua [90,104]. As many rare earth metals, Gd^{3+} is a toxic material. Accordingly, to reduce metal toxicity, improve solubility and bio-distribution of material compared to lone Gd^{3+} ion, chelators are routinely used to deliver paramagnetic materials such as Gd^{3+}. Depending on the chelator structure most chelated paramagnetic ions show lower relaxitivities than do free ions, largely due to the loss of some, if not all, of the coordinated water molecules. Both DOTA and DTPA are octodentate ligands, and such, the complex removes 8 out 9 water sites, leaving $q = 1$ [90]. For all clinically

approved commercial agents $q = 1$ and their relaxivities are small compared to what is theoretically possible, with r_1 values of only 4-5 $mM^{-1}s^{-1}$ [91]. Certainly, in attaining the high relaxivity values it is important the presence of more than one coordinated water molecules which can be achieved only through ligand structural modification while maintaining efficient thermodynamic stability of the Gd^{3+} complex.

Distance between the water protons and the unpaired electron spin (r) – The ability of Gd^{3+} to enhance the relaxation of neighboring protons is dependent on the sixth power of the inverse of the distance ($\frac{1}{r^6}$) between the paramagnetic centre of the complex (Gd^{3+}) and water molecules [97,101,102]. Thus, water molecules must be closed to the paramagnetic centre (inner sphere) for the contrast agent to have a sufficient effect on relaxivity and ideally bind directly to the Gd^{3+}.

Rotational correlation time (τ_R) – The Solomon-Bloembergen-Morgan theory predicts that an increase in τ_R by slowing the molecular tumbling of the agent in solution will result in an increase in relaxivity. Indeed, it has been demonstrated that the relaxivity of a Gd^{3+} chelate will increase upon slowing down of molecular tumbling (increasing its molecular weight) insofar as its water residence time is close to optimal [105-107]. The most common approach to reduce the rotational mobility of Gd^{3+} chelate and consequently increase τ_R is by attaching Gd^{3+} chelate to a macromolecule such as linear polymers, dendrimers and biological molecules [97]. Rigidly attached Gd^{3+} chelates to these macromolecules experience lower molecular tumbling behaviour due to molecular size and high

molecular weight and would exhibit the highest possible relaxivity, limited largely by the values of T_{1e}, and τ_M. Any motion of the Gd^{3+} chelate independent of the macromolecule, however, can reduce relaxivity considerably [97]. At high magnetic fields relaxivity is mainly controlled by rotational correlation time (τ_R) and shows an almost linear dependence upon τ_R [98], consequently increasing τ_R of Gd^{3+} chelate is of critical importance.

Electron-spin relaxation time, T_{1e} – The influence of electron spin relaxation on the relaxivity of Gd^{3+} complexes is essentially governed by the decay of the electron spin magnetization in the direction parallel to the external magnetic field described by the longitudinal electronic relaxation time, T_{1e}. The choice of Gd^{3+} ion as optimal relaxation agent stem from its long T_{1e} and large magnetic moment. In general, increasing T_{1e} will yield higher relaxivity, limited by the values of τ_M and τ_R. The electronic relaxation rate is related to transient zero-field splitting (ZFS) of the spin levels which is induced from collision between the chelate and solvent molecules. The magnitude of the transient ZFS is given by a term denoted B (see equation 2.20). In general an increase in B will lead to shorter T_{1e} values and reduced relaxivity. At low fields T_{1e} contributes significantly to the overall correlation time (see equation 2.18). However T_{1e} will increase with the square of the applied field, so at high fields, the contribution of T_{1e} to the overall correlation time τ_c becomes smaller, and the importance of B on relaxivity decreases with increasing field. The need for long T_{1e} translates into a demand to minimize ZFS in Gd^{3+} complexes. This parameter may be tuned through changes in ligand field strength and symmetry [97].

Residence lifetime of coordinated water molecules, τ_M - The residence lifetime, τ_M has a dual importance in relaxivity. It can contribute to the overall correlation time (τ_R) and it also modulates the efficiency of the chemical exchange between water molecules from inner sphere of the Gd^{3+} and the bulk ($k_{ex} = 1/\tau_M$) [108]. In order for water protons to be efficiently relaxed by Gd^{3+}, water from bulk solvent must be in rapid exchange with water molecules reaching the inner-sphere of Gd^{3+} (Figure 2.4) but the maximal relaxivity values never can be achieved if water exchange is either too slow or too fast. If τ_M is too short (<1 ns), relaxivity is limited because each water molecule isn't bound to the paramagnetic center long enough to become fully relaxed. Conversely, if τ_M is too long (> 1 μs), relaxivity is also limited because fewer water molecules reach the inner-coordination sphere of Gd^{3+} per unit time to have the maximum possible impact on the T_1 of bulk water protons [109]. As predicted by theory and experimentally observed, there is an optimal range for τ_M with respect to relaxivity. This has important implications when considering the design of an optimal MRI contrast agent. There is a parabolic dependence of relaxivity on τ_M as illustrated on Figure 2.5.

For all contrast agents in clinical use ($q = 1$), the exchange is primarily determined by the residual electric charge and the structural properties of the complex [98]. Since, for the Gd complexes with $q = 1$ the exchange mechanism is dissociative, the exchange rate is determined by the difference in energy between the nine-coordinated ground state and the eight coordinated activated state [98]. The Gd^{3+} ion has a low energy barrier between the eight-and nine-coordination states, favouring a fluxional state between the two and resulting in the fast water

exchange rates.

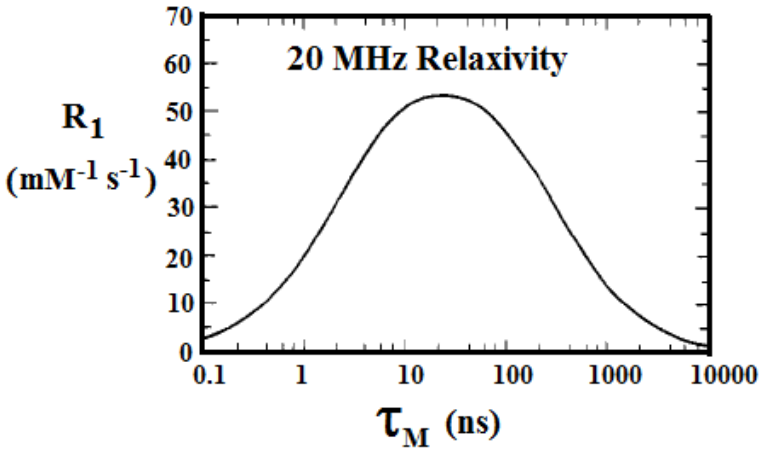

Figure 2.5: Calculated relaxivity at 20 MHz (SBM theory) for a typical Gd^{3+} complex [97].

The rate of water exchange of Gd^{3+} complex, however, is slowed significantly relative to that of the free ion, often to the extent that it is no longer in the optimal range for high relaxivity [110]. Recent attempts to increase water exchange rates by destabilizing nine coordinate ground state have resulted in less stable complexes [110]. Helm and Merbach (2005) reported that the exchange rate of water molecules can be influenced by modification of the chelating ligand [111]. It has been shown that increasing the steric hindrance on the first sphere water will increase the water exchange in case of Gd (III) complexes with dissociative exchange mechanism.

To achieve a practical high-relaxivity agent, the optimal combination of all relevant parameters must be accomplished while maintaining solubility and chelate stability. The optimization of one parameter will often hamper that of another, making the goal of high-relaxivity, practical agents a major challenge.

Chapter 3

Experimental methods and techniques

3.1 Synthesis

3.1.1 Length and α-Fe content control, synthesis method

The Fe-MWCNTs were grown on smooth Si/SiO_2 substrates held within the second zone of a two-zone horizontal CVD reactor. The reactor comprised a horizontal quartz tube inside coil preheater and reaction-zone (furnace) heating elements. The dimensions of the quartz tube used were as following : length: 2 m, outer diameter: 22 mm, and wall thickness: 1.5 mm.

A photograph of the important parts of the reactor used for the synthesis of the Fe-MWCNTs is shown in Figure 3.1.

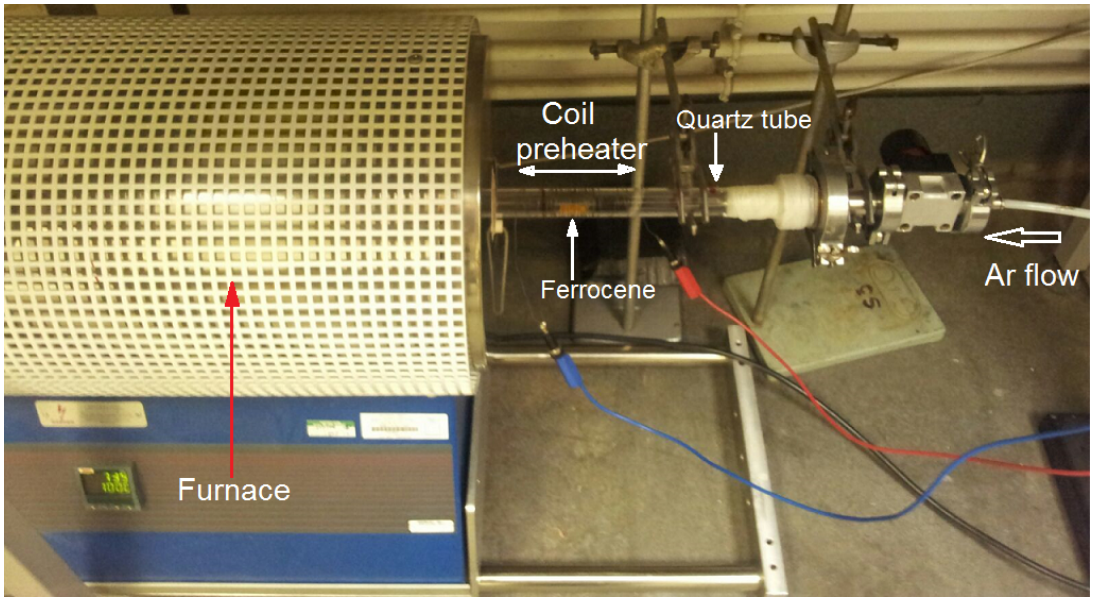

Figure 3.1: The experimental CVD reactor used for Fe-MWCNTs production. The Fe-MWCNTs nucleate and grow perpendicular to the substrate located inside the furnace.

The source vapour was produced by evaporation of ferrocene powder (98%) supplied by Sigma–Aldrich, in the first zone using a coil preheater of low thermal mass to minimise vapour-flow on-off times. The temperature of the preheater was kept constant at 185 °C by manually adjusting the electrical power delivered to the preheater. The ferrocene vapour was carried from the preheater to the reaction zone (furnace) in an argon flow of 10 ± 2 ccm (cubic centimetres per minute) at atmospheric pressure. The substrates were placed inside the furnace in a region in which the lateral temperature gradient was 10 °C/cm from 880 °C to 950 °C. The rates of ferrocene vapour mass flow used here (30−50 mg/min) were calculated by dividing the mass of ferrocene powder loaded into the preheater by the duration time as measured from onset of supply of power to the preheater to the time at

which complete evaporation occurred (determined by visual inspection). Different mass flow rates (duration time in brackets) 30 mg/min (1.16 min), 34 mg/min (1.16 min), 39 mg/min (1.5 min), 44 mg/min (1.5 min), and 50 mg/min (1.5 min) which I used in my experiments turned to have an approximately linear relationship with the nominal length of Fe-MWCNTs produced : 3 μm, 5 μm, 10 μm, 15 μm, and 20 μm, respectively.

After the synthesis, the reactor was cooled to room temperature at the natural rate of the furnace (11 h) and the structures were mechanically removed from the substrates. I used the slow cooling method since it guarantees a low relative abundance of Fe_3C single crystals inside MWCNTs. It is known that Fe_3C is not stable in contact with the MWCNTs walls and in slow cooling conditions the carbon atoms will migrate from the Fe_3C single crystals-core toward the single crystal-MWCNTs walls interfaces, forming additional graphitic layers.

3.1.2 Synthesis method of Fe-MWCNTs used for Gd^{3+} functionalization and SAR measurement

The reactor for Fe-MWCNT production comprised a horizontal quartz tube inside coil preheater and reaction-zone (furnace) heating elements, Figure 3.1. Ferrocene vapour was produced by sublimation of 58 mg of ferrocene powder (98%) supplied by Sigma–Aldrich, in the coil preheater stage (185 °C). The vapour was carried in a 14 ccm argon flow into the reaction zone (890–940 °C) at atmospheric pressure. The Fe-MWCNTs formed by self-organisational process on smooth quartz substrates placed inside the tube within the furnace. The vapour flow time was 1.5

min; the reactor was then cooled to 500 °C and the samples were annealed at this temperature for 12 h. Finally, the reactor was cooled to room temperature at the natural rate of the furnace. The Fe-MWCNT structures were then mechanically removed from the quartz substrates.

3.1.3 Synthesis method of textured arrays

Arrays of Fe-MWCNTs were grown on smooth Si/SiO_2 substrates held in the reaction zone of a horizontal CVD reactor, Figure 3.2. The source vapour was produced by the sublimation of 58 mg of ferrocene powder (98%) supplied by Sigma–Aldrich, in a downstream coil preheater held at $\sim$ 185 °C. The ferrocene powder was arranged in rows of approximately equal width and separation arranged parallel to the flow of argon carrier gas. Flow rate of the argon was 10 ccm. Two flat substrates (A and B in Figure 3.2), area $\sim$1 cm^2, used for the nucleation and growth of the array were placed in different temperature gradients within the reaction zone (furnace). The first (A) was placed in the gradient 885-940 °C and the second (B) in 940-970 °C. The duration of the reaction, measured from the onset of power supply to the coil preheater to the complete sublimation of the ferrocene powder, was 1.5 minutes.

The downstream divergence of the sublimated vapour, represented by one shaded triangular beam per ferrocene row, is inferred from examination of the reaction products on substrates A and B (see Figure 3.2). The broken circles in substrate A represent the inferred static cells of vapour produced by the interaction of the modulated vapour flow and the shear forces produced by the diffusion gra-

dient within the reaction zone; the solid circles in B represent similar, but less structured, cells in a region of diminished modulation.

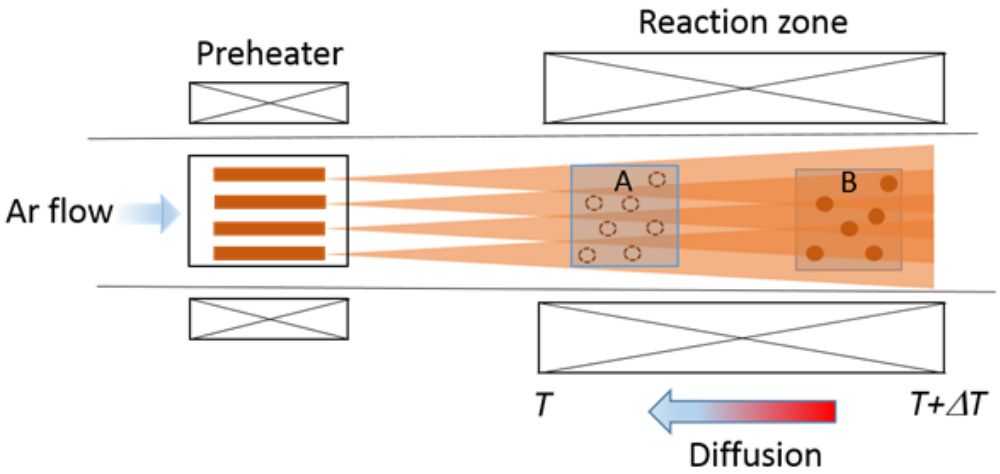

Figure 3.2: A schematic diagram of the horizontal CVD reactor (top view) used for production of textured Fe-MWCNTs.

The substrates, conditions of temperature, and flow rate chosen for the growth of textured arrays were those previously used to produce uniform, close-packed arrays of constant height in an unmodulated vapour flow. After the synthesis, the reactor was cooled to room temperature at the natural rate of the furnace.

3.2 Gd^{3+} functionalization

For Gd^{3+} functionalization of Fe-MWCNTs, 50 mg of Fe-MWCNT powder and 75 mg of anhydrous gadolinium chloride ($GdCl_3$) were stirred together in 75 ml deionized water and sonicated in an 80 W ultrasonic cleaner for two hours. The solution was left undisturbed overnight whereupon the Gd^{3+} loaded Fe-MWCNTs flocculated from the solution. The supernatant solution was then decanted. The

sample was washed by mild sonication in 19 ml of deionized water to remove any unabsorbed $GdCl_3$. The Gd^{3+} loaded Fe-MWCNTs flocculated again from solution and the supernatant solution was decanted. The washing procedure was repeated three times before the sample was dried in air.

Anhydrous gadolinium chloride (99.99%) used for the functionalization of Fe-MWCNTs was supplied by Sigma-Aldrich.

3.3 Characterization techniques

Transmission electron microscopy (TEM), High-resolution TEM (HRTEM), scanning electron microscopy (SEM) and X-ray diffraction (XRD) were used to analyse the morphology, structure and composition of the Fe-MWCNTs. Heating functionality in an alternating applied magnetic field was quantified through the measurement of SAR. Characterization by electron paramagnetic resonance (EPR), electron energy loss spectroscopy (EELS) and HRTEM confirmed the presence of Gd^{3+} ions on the sidewall surface of MWCNTs. In particular, EPR spectroscopy was used to assess the presence of Gd^{3+} ions since this method is sensitive to paramagnetic ion content. Nuclear magnetic resonance (NMR) spectroscopy was used to measure the relaxation time T_1 by the inversion-recovery method.

3.3.1 X - ray diffraction

XRD analyses were performed using a Siemens D5000 diffractometer and an Xpert-Pro diffractometer (both with Cu Kα sources with $\lambda = 0.154$ nm) which

are capable of measuring diffraction of powders and thin films. The Rietveld refinement method, which applies the least-squares approach to match a theoretical line profile to the diffractogram, was used to identify, and estimate the relative abundances of the phases contained within the sample from the area enclosed by diffraction peaks. The software GSAS (General Structure Analysis System) was used to refine a theoretical line profile until it matched with the measured one. A schematic diagram of a diffractometer is depicted in Figure 3.3.

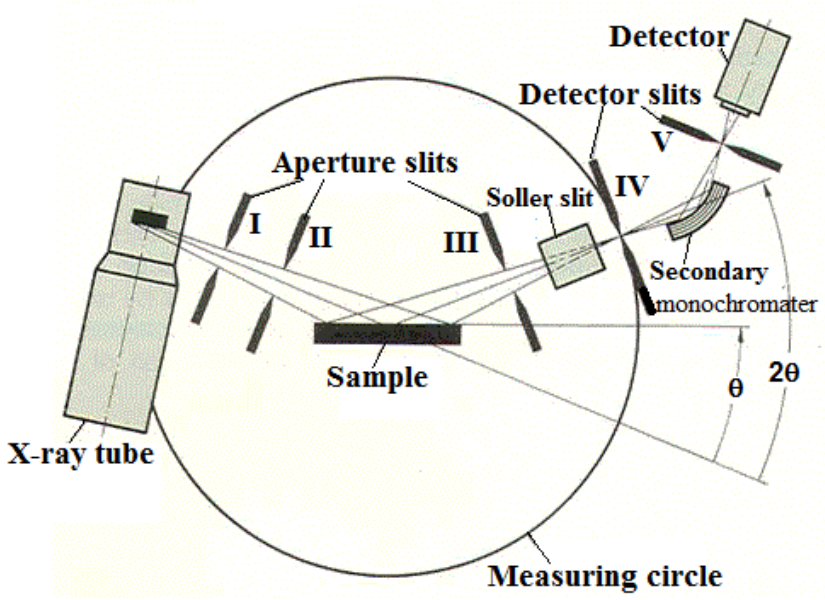

Figure 3.3: Schematic representation of a X-ray diffractometer [112].

The sample is positioned in the center of the diffractometer and the probing x-ray beam is directed to the sample surface at an angle θ. At the same angle the detector monitors the scattered radiation. The diffraction pattern is collected by varying the incidence angle of the incoming x-ray beam by θ and the scattering angle by 2θ while measuring the scattered intensity $I(2\theta)$ as a function of the latter. The crystalline phases present in the material are then manifested by the

Bragg peaks. In order to obtain a diffraction peak the Bragg equation (3.1) has to be obeyed.

$$2d \sin\theta = n\lambda, \tag{3.1}$$

where the integer n has the meaning of a reflection order and the other terms are shown in Figure 3.4.

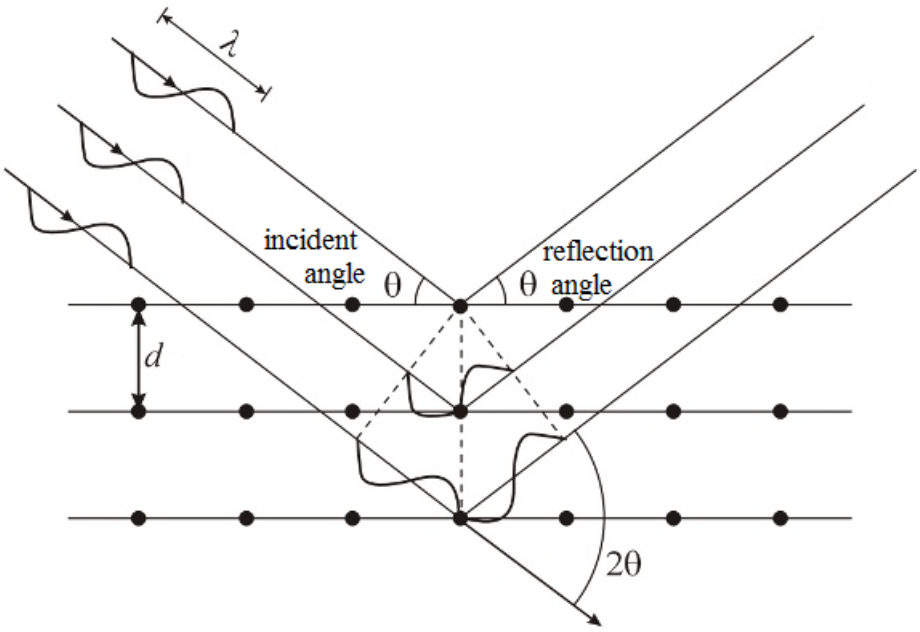

Figure 3.4: Visualization of the Bragg equation. X-rays diffracting from the atomic planes of a crystal [112].

3.3.2 Electron Microscopy

Scanning electron microscopy (SEM), energy dispersive X-ray spectroscopy (EDX) and backscattered electron investigations were performed using an FEI Inspect F system. SEM provides detailed high resolution images of the sample by rastering a focussed electron beam across the surface and detecting secondary or backscattered electron signal. The normal image is formed by secondary electrons expelled

from the surface and collected by the two lens detector. Primary electrons which are reflected are called backscattered electrons, their intensity is dependent on the atomic number of the element, therefore the backscattered electron detector (BSED) allows one to identify iron nanowires enclosed within the nanotubes and roughly measure their dimensions.

Ionized atoms can relax by electron shell-to-shell transitions, which lead to X-ray emission. The X-rays emitted are characteristic of the elements present in the sample and are measured by the EDX detector.

From the SEM normal images I observed the alignment of Fe-MWCNTs on silicon substrates and estimated their length, whereas from the backscattered images I roughly measured the dimension of iron nanowires inside MWCNTs.

For textured Fe-MWCNTs, EDX analyses were performed on substrate-supported samples to investigate the distribution of the elements present in the product.

Transmission electron microscopy (TEM) and selective area electron diffraction (SAED) were performed using a 200 kV Jeol Jem 2010.

HRTEM was performed using both a 200 kV Jeol Jem 2010 microscope and a 100 kV Nion UltraSTEM 100, C_S corrected.

The image acquisition and processing software used in all the TEM investigations was Gatan Digital Micrograph.

The samples for TEM were prepared by dropping small volumes of material dispersed in ethanol onto carbon-coated copper grids followed by drying in ambient conditions.

The maximum spatial resolution available from the TEM was 0.15 nm. The lattice spacings extracted from the SAED analyses are reported with an accuracy of 0.01 nm.

From the TEM images I measured the length and the diameter of the iron nanowires encapsulated by MWCNTs. More than 150 individual Fe-MWCNTs were investigated. Also, the crystal orientation and phase distribution within the iron nanowires were investigated by HRTEM and SAED images.

Scanning transmission electron microscopy-annular dark-field (STEM-ADF) imaging, a technique that is atomic number sensitive in an aberration-corrected STEM with chemical mapping by EELS were used to investigate the spatial distribution of gadolinium in Gd^{3+} functionalized Fe-MWCNTs.

STEM-ADF and EELS were performed on the Nion UltraSTEM 100, Cs corrected, dedicated scanning transmission electron microscope equipped with a Gatan Enfina EELS spectrometer. The acceleration voltage used for the experiments was 100 kV, with a probe size of 0.09 nm. The data were acquired at a collection angle of 31 mrad.

The samples for EELS were prepared by transferring the structures to carbon-coated copper grids and baked at 135 °C for 6 h. There was no time variation of the EELS chemical mapping signals, taken using a 100 keV probe, on a time scale of several hours.

EELS involves measurement of the energy distribution of electrons that have interacted with a specimen and lost energy due to inelastic scattering.

The atomic electrons that are located in inner shells (labelled K, L, M *etc* from the nucleus outwards) have binding energies that are mostly hundreds or thousands of electron volts and their excitation by a transmitted electron gives rise to ionization edges in the energy-loss spectrum. Since each ionization edge occurs at an energy loss that is characteristic of a particular element, EELS can be used to identify the elements present within the region of specimen defined by the electron beam. The ionization edges occur superimposed on a background that represents energy loss due to valence electrons (for example, the high-energy tail of a plasmon peak) or ionization edges of lower binding energy.

This background contribution can be extrapolated and subtracted, for quantitative elemental or structural analysis. Extrapolation usually assumes a power-law energy dependence: AE^{-r}, where A and r are determined from least squares fitting to the pre-edge background [113].

The energy-loss intensity is then integrated over an energy range Δ beyond the edge threshold; for $\Delta > 50$ eV, the near-edge fine structure is averaged out and the resulting integral $I_c(\beta, \Delta)$ represents the amount of the element, independent of its atomic environment (Figure 3.5); β represents the collection semi-angle.

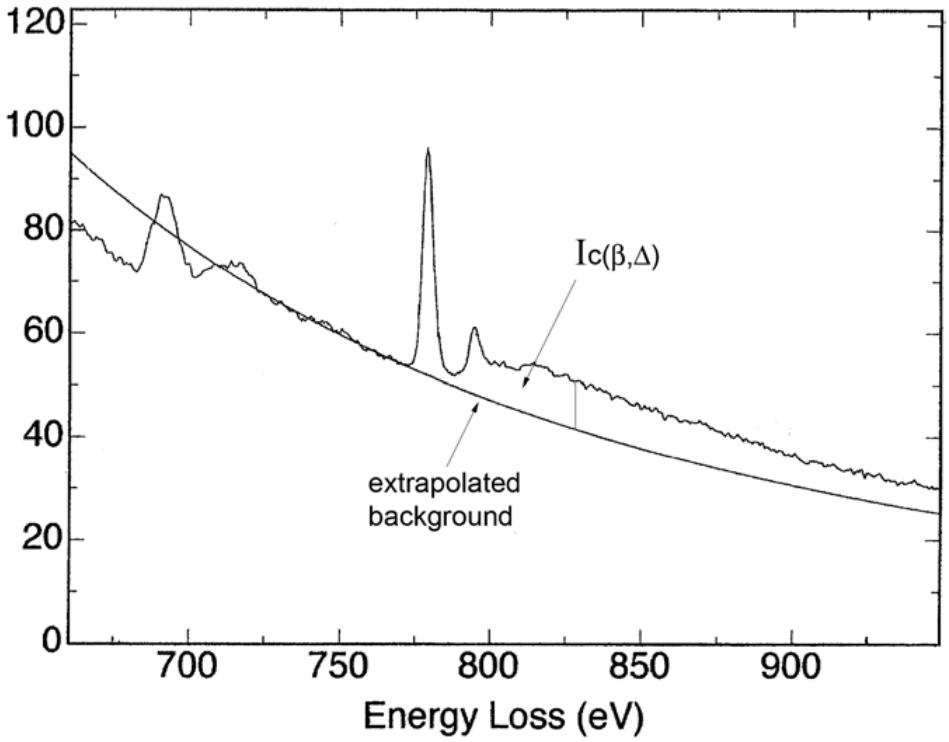

Figure 3.5: Procedure for elemental quantification, based on background extrapolation and integration of the intensity (above background) over a range Δ beyond the edge threshold [113].

Figure 3.6 shows the procedure used for background subtraction in the EELS spectrum taken at an individual Fe-MWCNT in the energy range of the iron L-edge. The background was subtracted by fitting a decaying power-law function to the energy window below the edge onset (see Figure 3.6).

In Figure 3.7 is shown the EELS spectrum taken at an individual Fe-MWCNT in the energy range of the iron L-edge after background subtraction.

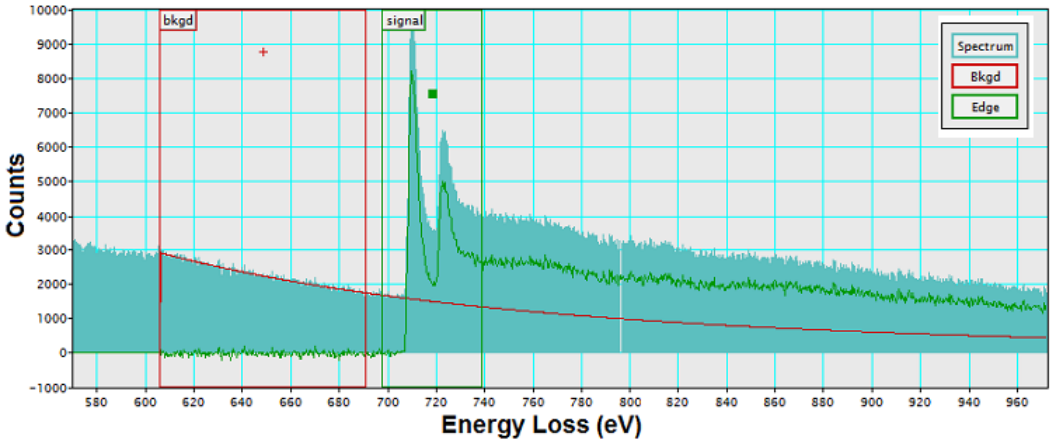

Figure 3.6: EELS spectrum taken at an individual Fe-MWCNT in the energy range of the iron L-edge before background subtraction.

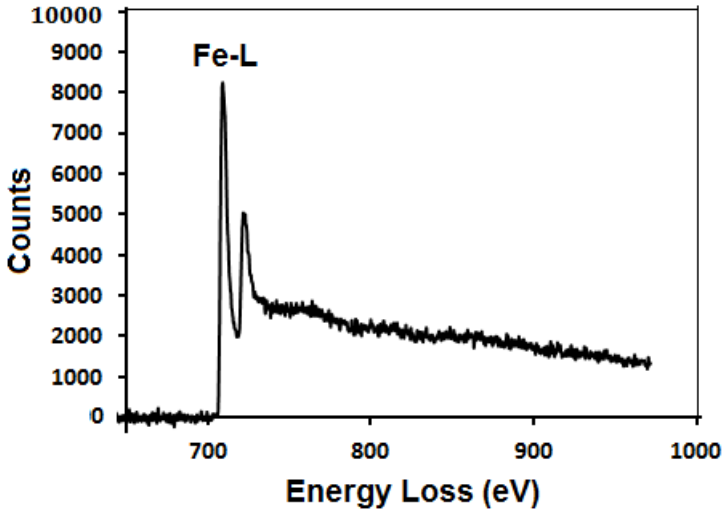

Figure 3.7: EELS spectrum taken at an individual Fe-MWCNT in the energy range of the iron L-edge after background subtraction.

3.3.3 Magnetic characteristics

Magnetic properties of Fe-MWCNTs and Gd^{3+} functionalized Fe-MWCNTs were investigated with a Quantum Design MPMS-7 SQUID magnetometer. The field

dependence of DC magnetization *M(H)* was measured at 5 and 300 K in magnetic field up to 50 kOe. The samples were investigated as dry powders.

For magnetic measurements the mass and susceptibility of the sample holder should be as small as possible in order to minimize its background contribution and signal distortion. Therefore, during this measurement a plastic straw was used as the sample holder due to its minimal magnetic susceptibility and small mass. A plastic disc about 2 mm thick with an outside diameter equivalent to the diameter of the plastic straw is inserted and twisted into the small straw segment. The powdered sample was poured inside the small straw segment and a second disc with a diameter slightly less than the inside diameter of the plastic straw was placed on top to help provide the desired symmetry. Then the small straw segment was located approximately in the middle of a large plastic straw. After that the large plastic straw was attached to the sample rod which is used to insert the sample into the SQUID magnetometer.

3.3.4 Electron paramagnetic resonance spectroscopy

The presence of Gd^{3+} ions in the Fe-MWCNTs surface-functionalized with paramagnetic Gd (III) samples was investigated by using electron paramagnetic resonance (EPR) spectroscopy because the technique is sensitive to paramagnetic ion content.

EPR measurements were performed at room temperature using a Bruker Elexsys E 580 spectrometer, in the X frequency band (9.4 GHz).

There are various advantages of going to higher and lower frequencies, depending

on the paramagnetic system in question, but X - band offers the best compromise for resolution, intensity and ease of use.

The experimental setup is based on a monochromatic radiation source coupled with a variable magnetic field. The EPR spectrum is essentially a plot of microwave absorption (at constant frequency) as a function of applied magnetic field.

Since the electron has a magnetic moment, it acts like a bar magnet when it is placed in a magnetic field, B_0. The energy difference we study in EPR spectroscopy are predominately due to the interaction of unpaired electrons present in the sample with a magnetic field produced by a magnet in the laboratory. This effect is called Zeeman effect. The existence of two Zeeman levels, and the possibility of inducing transitions from the lower energy level to the higher energy level is the basis of EPR spectroscopy. The two energy levels of the electron with a parallel and an anti-parallel spin is written as:

$$E = \pm \frac{1}{2} g \mu_B B_0, \tag{3.2}$$

where g is the electron factor, μ_B the Bohr magneton and B_0 is the applied magnetic field. This is called the electron Zeeman energy. Application of an oscillating magnetic field perpendicular to an applied magnetic field B_0 in z direction induces transition of the electron spins when the resonance condition:

$$\Delta E = h\nu = g \mu_B B_0 \tag{3.3}$$

is satisfied.

3.3.5 Relaxivity measurement of Gd^{3+} functionalized Fe-MWCNTs

The relaxation times of Gd^{3+} functionalized Fe-MWCNTs samples were measured at two different magnetic field strengths: 9.4 and 14 T with Bruker AVIII 400 and Bruker AV600 spectrometers respectively. The inversion-recovery method was used to measure T_1.

The samples were prepared by sonicating Gd^{3+} functionalized Fe-MWCNTs in solution consisting of heavy water (D_2O) and 2% by weight sodium dodecyl benzene sulfonate (SDBS). SDBS was supplied by Sigma-Aldrich.

A control sample solution contain pristine, unfunctionalized Fe-MCWNTs was prepared using the same methodology as above.

After relaxation rate measurement, the concentration of the gadolinium in the sample solutions was determined by inductively coupled plasma optical emission spectrometry (ICP-OES, Varian Vista-PRO CCD).

The longitudinal relaxivity (r_1) of the samples was determined by:

$$T_{1obs}{}^{-1} = T_{1d}{}^{-1} + r_1[Gd^{3+}], \tag{3.4}$$

where T_{1obs} and T_{1d} are the relaxation times (in seconds) of the sample and the matrix (D_2O + SDBS) respectively, and $[Gd^{3+}]$ is the gadolinium concentration in mM.

3.3.6 Heating of Gd^{3+}-functionalized Fe-MWCNTs in alternating magnetic field

The heating functionality of Gd^{3+}-functionalized Fe-MWCNTs was studied using a MagneTherm system (NanoTherics) which has been designed to operate at a wide range of frequencies from 50 kHz to 1 MHz with field strengths up to 20 kA/m (25 mT). The water - cooled copper coil used during my measurements had 6 turns with an outer diameter of 54 mm and the height of 24 mm. The sample was inserted in an eppendorf tube which was then placed inside an expanded styrofoam cover and finally positioned within the sample aperture tube in the center. The sample aperture tube was then placed inside the coil. The temperature of the sample during the measurements was determined by a type T thermocouple connected to a digital multimeter.

The sample was prepared by mixing gadolinium-functionalized Fe-MWCNTs in 1:1 weight ratio with human serum albumin and dispersed in phosphate buffered saline using ultrasonication. Both human serum albumin and phosphate buffered saline were supplied by Sigma-Aldrich.

The volume of the sample was 2 ml and the concentration was 5 mg/ml. Calorimetrical measurements were done in an alternating applied magnetic field of frequency of 696 kHz and strength of 8 kA/m.

Chapter 4

Results and discussion

4.1 Length and α-Fe content control of self-organised ferromagnetic nanowires encapsulated by multiwalled carbon nanotubes by low flow-rate CVD

Ferromagnetic iron nanowires encapsulated by multiwalled carbon nanotubes have been synthesised by CVD method in which the species produced by the thermal decomposition of ferrocene provide nucleating metal droplets and the chemical feedstock for self-organised growth of structures perpendicular to the Si/SiO_2 substrates at elevated temperature [25].

Confinement of the nanowire within the central capillary of the nanotube can result in unusual compositions not readily obtainable in the bulk. The carbon nanotube chemically passivates the nanowire and prevents its mechanical degradation. Applications follow from the ability to tune the magnetic response through the composition and shape anisotropy of the nanowire [59]: microwave absorp-

tion materials [114], nanocomposite filler particles [115], biomedical [4,116-119], nanoscale inductors [120], magnetic force microscopy probes [121], and magnetic paper [122].

As outlined in Chapter 1 the majority of effort has been focussed on encapsulation of elemental α-Fe, owing to both the characteristically high saturation magnetisation and coercivity, however the most commonly observed encapsulated nanowires contain crystallites of α-Fe, γ-Fe, and Fe_3C [18,19,22 - 24].

In many reports, the nanowires are not continuous but comprise isolated 10s-100s nm length crystallites with a much greater intermediate spacing and the nanotubes have low graphitic quality (as judged by the straightness of the structure). A continuous, completely α-Fe nanowire is desirable for magnetic hyperthermia application, as is control of both nanowire and nanotube length and diameter.

In this section it is shown a systematic study of length-diameter, and nanowire content based on a low vapour flow-rate and a constant close-to-melting-point temperature for the evaporation of ferrocene. The latter consideration is intended to avoid dispersion in the diameter of the nucleating Fe droplet. I contend that in view of the evidence for the open-tip temperature gradient model at $\sim$10 ccm flow rates, synthesis conditions which favour this condition are desirable since, freed of the necessity to provide a temperature gradient which drives vapour feedstock to the growth front, it facilitates fine-tuning of the synthesis temperature to favour decomposition of Fe_3C into α-Fe and graphitic carbon [26]. The synthesis temperature is fixed in narrow range 880-950 °C to encourage C-diffusion but

minimise damping of the tip temperature gradient by the natural gradient in the reactor. Under these constrains, the key variable is the mass flow rate of ferrocene vapour into the second zone of the reactor. Low rates of supply of vapour feedstock favour low carbide content and the desirable γ-α transition owing to the associated longer residence times (time exposed to elevated temperature). Here it is demonstrated that this regime guarantees nanowire continuity by providing a local, rather than global, temperature gradient to drive the vapour feedstock to the active growth front.

The low vapour flow-rate and constant evaporation temperature method achieved continuous α-Fe nanowires on the same scale as the nanotube for lengths greater than 10 μm without the necessity of post-synthesis heat-treatment or introduction of other precursor elements. Whereas, for initially mixed-phase nanowires of length less than 10 μm, the continuous α-Fe nanowires were achieved by post-synthesis heat treatment.

4.1.1 Morphology and structural composition analysis

Figure 4.1 shows typical SEM images of as-grown structures vertically aligned on smooth Si/SiO_2 substrates. Mass flow rates (duration time in brackets) 30 mg/min (1.16 min), 34 mg/min (1.16 min), 39 mg/min (1.5 min), 44 mg/min (1.5 min), and 50 mg/min (1.5 min) have an approximately linear relationship with the nominal length obtained from visual inspection: 3 μm, 5 μm, 10 μm,

15 μm, and 20 μm, respectively. From these results, I certainly can say that by increasing the mass flow rate of ferrocene, the growth rate of Fe-MWCNTs was increased. This suggests that the growth rate of the Fe-MWCNTs was mass transport controlled during the deposition process. Length control of Fe-MWCNTs was achieved by using a low flow-rate CVD process with high synthesis temperature, constant evaporation temperature and systematically changing the mass flow rate of ferrocene.

Indeed, at low flow rates regime, high synthesis temperature (880-950 °C) and under atmospheric pressure, conditions used in our experiments, the growth rate in CVD processes is controlled by mass transport of the first type which as it is described in Chapter 2 is an equilibrium process determined by mass input.

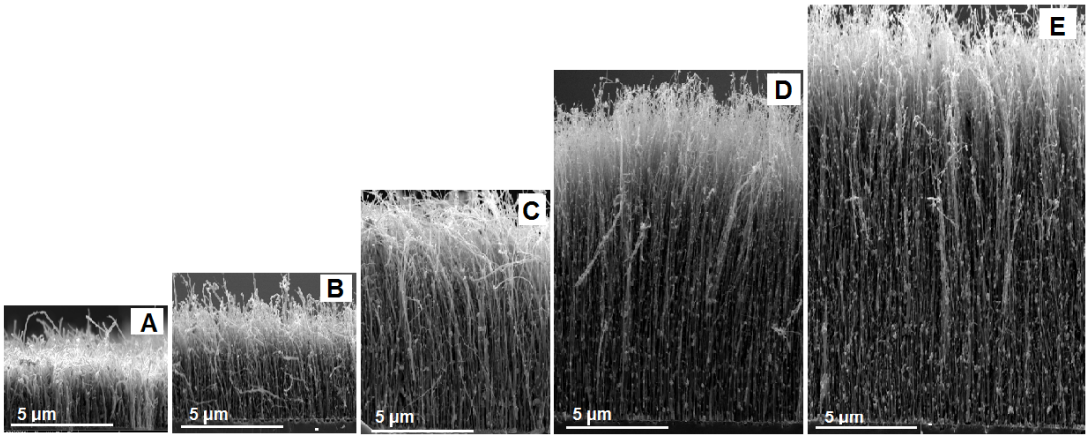

Figure 4.1: Representative SEM micrographs of structures produced by various rates of ferrocene mass flow: (A) 30 mg/min, (B) 34 mg/min, (C) 39 mg/min, (D) 44 mg/min, and (E) 50 mg/min. The image is of a cross-section through the silicon produced by cleaving through the centre of the substrate.

At the low flow rates, the vapour stream has a sufficient residence time to

equilibrate with the substrate surface, whereas the high synthesis temperature would not allow the surface kinetics to control the growth rates which happened at low temperature (<700 °C) [71]. In this regime, based on the theory associated to the CVD growth rate model (equations and details are given in Chapter 2), the growth rate is proportional to the bulk reactant concentration. This is why it is managed to grow Fe-MWCNTs with different length by only changing the mass flow rate of ferrocene.

Compositional analysis of as-grown structures was performed by Rietveld analyses of XRD data, Figure 4.2. The Rietveld refinement was made with the following components α-Fe (Im-3m, Crystal Open Database Ref.64998), γ-Fe (Fm-3m, Crystal Open Database Ref.9008469), Fe_3C (Pmna, Crystal Open Database Ref.16593), graphitic carbon (P63/mmc, Crystal Open Database Re.53781), Fe_3O_4 (space group Fd-3m). The origin of oxide components is oxidation of residual elemental iron when the sample is removed from the reactor and handled in air.

The common peak at 26.2° corresponds to the characteristic 002 reflection of graphitic carbon structure of the multiwalled carbon nanotube, the symmetry and the narrowness of this peak is indicative of the high degree crystallinity. This conclusion is supported by the uniformity and integrity of the nanotube walls directly imaged by HRTEM, Figure 4.4 (D,E). The main encapsulated phases were revealed to be those commonly observed, namely α-Fe, γ-Fe and Fe_3C. The presence of the α-Fe in the samples is revealed by observation of the 110 reflection at 44.8° while the presence of the γ-Fe is revealed by the 111 and 200 reflections at 43.8° and 50.8°, respectively. Multiple reflections indicative of Fe_3C were observed

along with 200, 121 and 211 reflections at 35.3°, 37.7° and 42.9°, respectively.

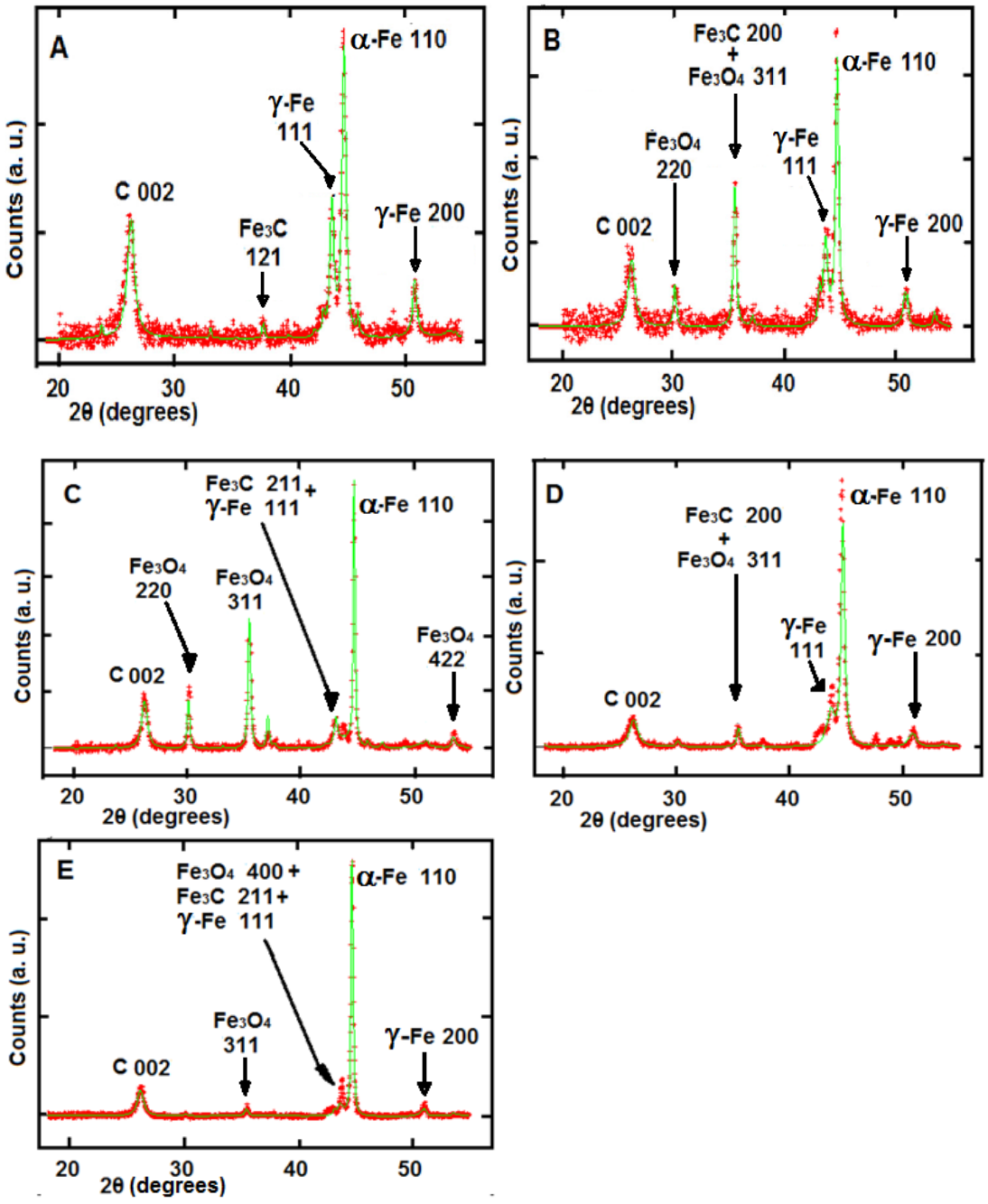

Figure 4.2: Typical X-ray diffraction data (red), and Rietveld refinement (green) of Fe-MWCNTs, for lengths 3 μm (A), 5 μm (B), 10 μm (C), 15 μm (D), and 20 μm (E).

The dependence of the nanowire composition on length is summarised in Table 1.

Table 1. Relative abundances of the nanowire phases extracted from the Rietveld refinement of the XRD data in Figure 4.2.

Length (μm)	α-Fe (wt. %)	γ-Fe (wt. %)	Fe_3C (wt. %)
3	70	24	6
5	74	22	4
10	94	3	3
15	87	10	3
20	94	5.7	0.3

Clearly, there is a step change in α-Fe content, from $\sim$70% to $\sim$90%, as the length increases from 5 μm to 10 μm. The diminution of the γ-Fe and carbide with increasing length is likely to be the consequence of the longer residence time (the length of time at elevated temperature) increasing the probability of γ-α transitions and facilitating carbon diffusion from nanowire to nanotube.

An alternative explanation for the diminution of γ-Fe is that these crystallites occur at the ends of the nanowire where confinement effects could be expected to dominate.

The nanowire and nanotube diameter distributions of the 5 μm and 10 μm length were determined from TEM micrographs (examples in Figure 4.4) of the 5 μm and 10 μm length, Figure 4.3.

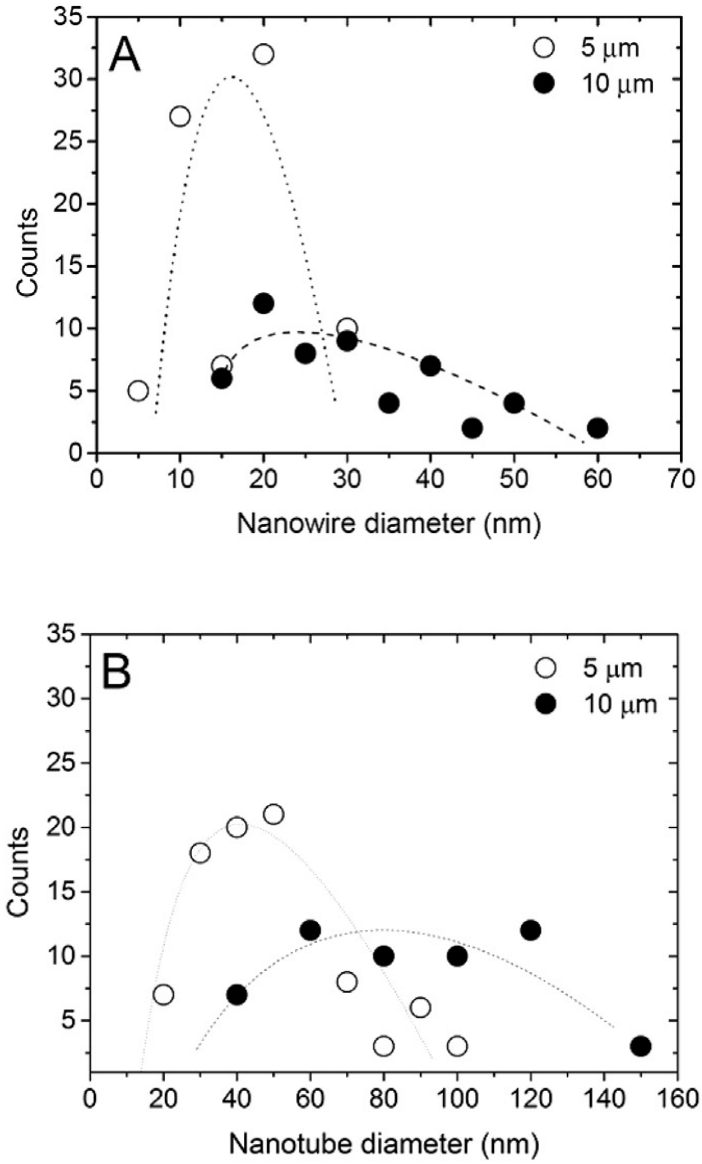

Figure 4.3: Diameter distributions for lengths 5 μm and 10 μm obtained from direct observation of TEM micrographs: (A) nanowire and (B) nanotube, the dotted lines are guides to the eye. For length 5 μm, the average nanowire diameter is 18 nm and that of the nanotube is 48 nm. For the 10 μm structure, the average nanowire diameter is 30 nm and that of the nanotube is 90 nm.

Clearly, there is approximate doubling of both the nanowire and nanotube diameters as the length increases from 5 μm to 10 μm, which is likely to result

from the larger nucleating droplet diameter that is the consequence of ferrocene vapour partial pressure as the mass flow rate is increased from 36 mg/min to 44 mg/min.

The encapsulating nanowires in the 5 μm and 10 μm length structures are continuous for at least 3 μm and 6 μm, respectively, Figure 4.4 (A-C); the latter value was confirmed by back-scattered electron images of randomly oriented structures, an example is given in Figure 4.4 (C); the upper encapsulated nanowire (bright region) is continuous for 6 μm.

HRTEM images Figure 4.4 (D,E) show detail of the crystalline structure of the nanowires and nanotube. Note that in contrast to previous reports of intermediate amorphous layers, there is an abrupt interface between the nanowire and nanotube, Figure 4.4 (E) [19].

In the HRTEM image, Figure 4.4 (E) the inter-planar distances of in the nanowire and nanotube, 2 Å and 3.4 Å, correspond to the (110) planes of α-Fe and (002) planes of graphitic carbon, respectively.

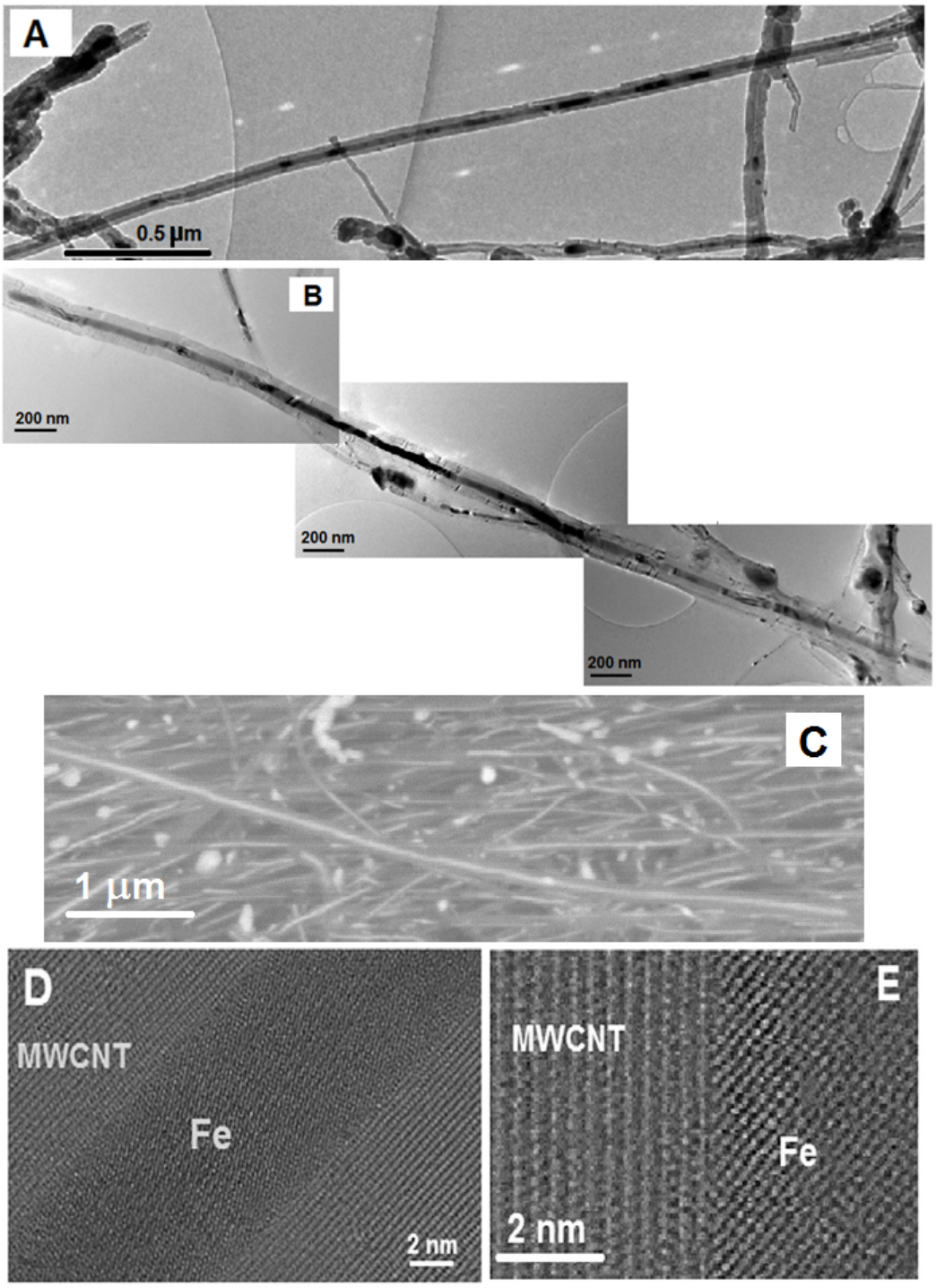

Figure 4.4: TEM images 5 μm long structures showing the continuity on the nanowire (A). (B) A sequence of transmission electron micrographs following an individual filled MWCNT; the filling is continuous for $\sim$5 μm. (C) Back-scattered electron image of randomly oriented 10 μm long structures showing the encapsulated nanowire (bright regions), and (D,E) typical HRTEM images of the 5 μm and 10 μm long samples, respectively.

The principle of carbide and γ-Fe reduction through postsynthesis heat-treatment mixed-phase nanowires was demonstrated by annealing a powder of 10 μm-long structures at 500 °C and for 12 h. The post-heat treatment XRD and Rietveld analyses revealed a slight increase of α-Fe content from 94% to 98.4% but reduction of the other phases to negligible amounts, γ-Fe (0.65%) and Fe_3C (0.95%) (Figure 4.5).

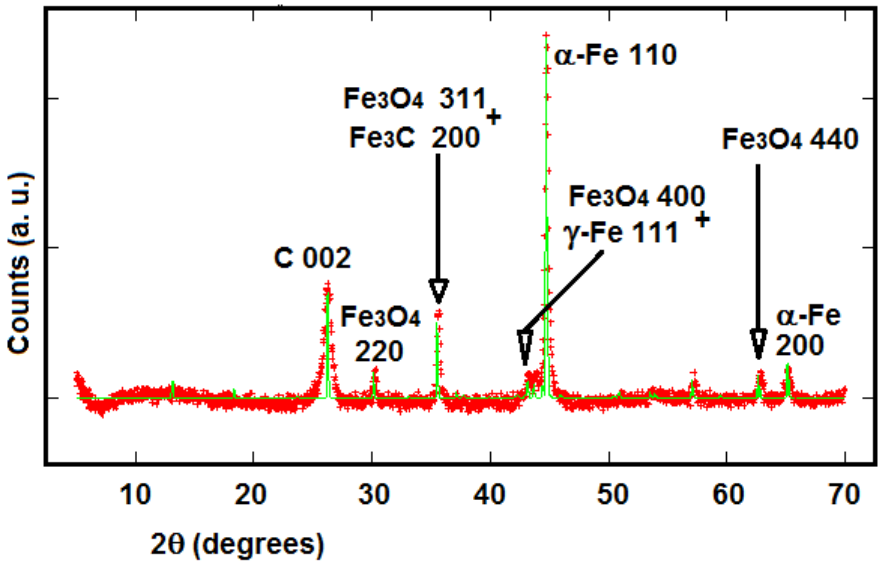

Figure 4.5: Typical X-ray diffraction data (red), and Rietveld refinement (green) of 10 μm long structures after heat treatment at 500 ^{0}C for 12 h. The refinement was made with the following components α-Fe (Im-3m, Crystal Open Database Ref.64998), γ-Fe (Fm-3m, Crystal Open Database Ref.9008469), Fe_3C (Pmna, Crystal Open Database Ref.16593), graphitic carbon (P63/mmc, Crystal Open Database Re. 53781), Fe_3O_4 (space group Fd-3m). The origin of oxide components is oxidation of residual elemental iron when the sample is removed from the reactor and handled in air.

TEM and SAED investigations of annealed Fe-MWCNTs, also confirm the presence of continuous α-Fe nanowires inside MWCNTs (see Figure 4.6). In the

TEM micrographs it is possible to notice the high morphological quality of the MWCNT filling. In the SAED, the red circles indicate the 002 diffraction spots of the graphitic MWCNT (space group P63/mmc) corresponding to a lattice spacing of 0.34 nm. The yellow circles indicate the 101 and 10-1 diffraction spots of α-Fe corresponding to a lattice spacing of 0.20 nm.

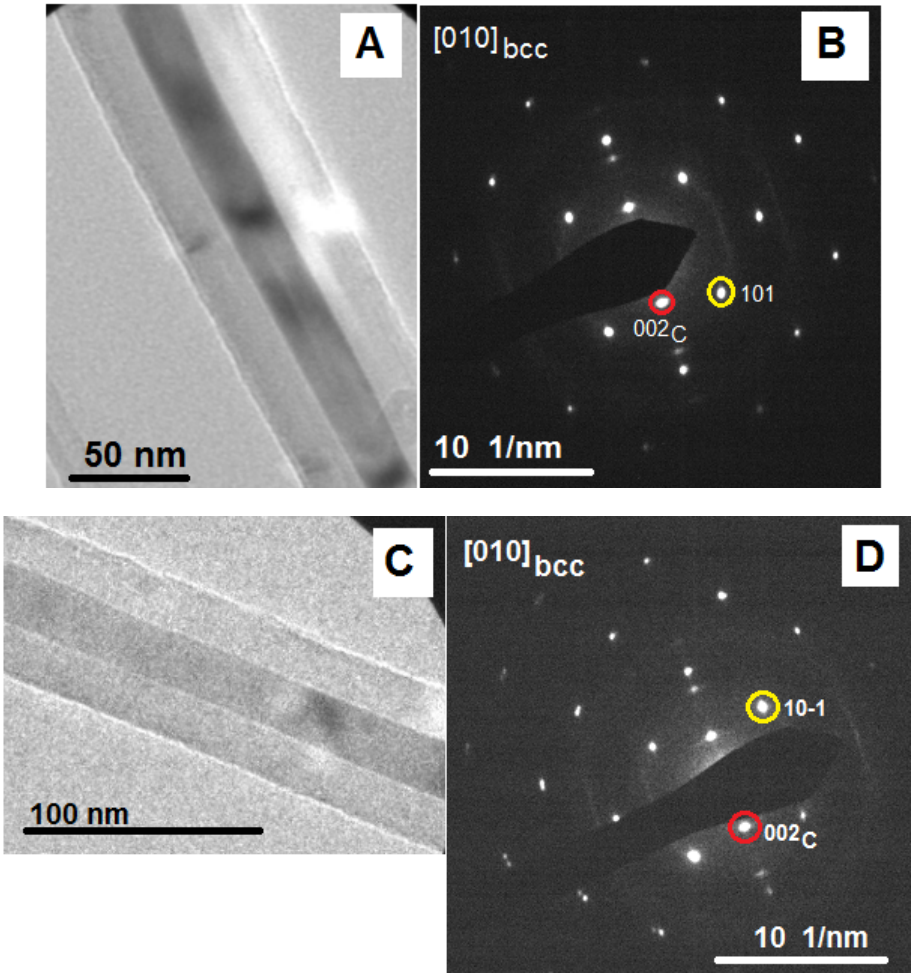

Figure 4.6: Transmission electron micrographs (A, C) showing typical MWCNTs continuously filled with α-Fe and (B, D) corresponding selected area electron diffractions. The diffraction patterns can be readily indexed to bcc iron single crystals viewed along [010] zone axes. The 002 spots originate from the graphitic tubular layers of MWCNTs.

In conclusion, here it is shown a low vapour flow-rate and constant evaporation temperature method which achieves continuous α-Fe nanowires on the same scale as the nanotube for lengths >10 μm without the necessity of post-synthesis heat-treatment or introduction of other precursor elements. The low vapour flow-rate regime has the advantage of sustaining the intrinsic temperature gradient at the tip of the forming structure which drives the vapour feedstock to the growth front to guarantee continuous nanowire formation.

For initially mixed-phase nanowires of length less than 10 μm, continuous α-Fe nanowires can be achieved by post-synthesis heat treatment.

4.1.2 Magnetic properties

The magnetic field dependence of the magnetization of as grown material in randomly oriented powder form exhibited ferromagnetic hysteresis at 5 K, Figure 4.7. The saturation magnetization,M_S and coersivity H_C show length dependence. It is observed a slight increase of the saturation magnetization with increasing length and a slight decrease of the coercivity, M_S (5 μm) = 42 emu/g and M_S (10 μm) = 51.5 emu/g, H_C (5 μm) = 910 Oe and H_C (10 μm) = 846 Oe. Using the same Rietvelt refinement method outlined in Figure 4.2, the relative abundances of the components found in the powder comprising 5 μm long structures expressed as wt.% are 65% carbon nanotube, 24% α-Fe, 0.4% γ-Fe, 0.6% Fe_3C, and 10% Fe_3O_4, whereas for 10 μm long structures, 53% carbon nanotube, 32% α-Fe, 0.39% γ-Fe, 0.49% Fe_3C, and 14% Fe_3O_4. Note that the oxide components are a consequence of the oxidation of residual external elemental iron when the sample

is removed from the reactor and handled in air; this conclusion follows from direct observation of unencapsulated, approximately spherical, external Fe_3O_4 crystallites by TEM. Based on these result I can say that the increase of the saturation magnetization with increasing the length may be attributed to the greater abundance of ferromagnetic phases (α-Fe, Fe_3C, and Fe_3O_4) in the 10 μm structures compared to that of the 5 μm length sample. The coercivity difference can be explained with the increase of the nanowire diameter since the external oxide particles are approximately spherical. A coercivity increase with reduced the diameter has been previously reported [123,124].

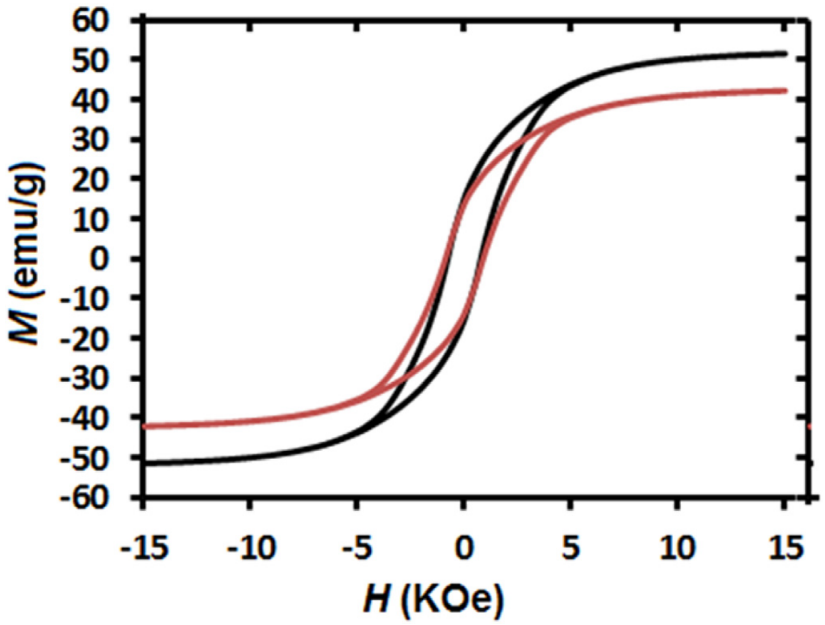

Figure 4.7: The magnetic field dependence of dc magnetization at T = 5 K for powder comprising 5 μm long structures (red line) and 10 μm long structures (black line).

The observed coercivities of 846 Oe and 910 Oe are much higher than that for the bulk polycrystalline Fe (∼1 Oe) and nanocrystalline Fe (∼23 Oe). The large

shape anisotropies of the nanowires can account for the large coercivity. As can the well-known dependence on crystallite dimension (d); for $d > 30$ nm, coercivity is proportional to $1/d$ and for $d < 30$ nm, coercivity varies as d^6 [125,126]. The saturation magnetisation (M_S = 51.5 emu/g) is found for the 10 μm length sample at an applied field of 15 kOe. Likodimos *et al.* reported that pure MWCNTs have a diamagnetic behaviour with M_S = -0.7 emu/g at 50 kOe [57]. Subtracting the weighted diamagnetic contribution of the carbon nanotube walls, I calculated the combined saturation magnetization of the ferromagnetic material present in our sample (α-Fe, Fe_3C and Fe_3O_4) to be $M_S \sim 112$ emu/g at 5 K. This value is lower than the estimated saturation magnetization M_S ~181 emu/g at 5 K for a bulk sample corresponding to the same fraction of ferromagnetic components calculated by taking the weighted sum of the saturation magnetization of bulk α-Fe (M_S ~220 emu/g; T_C = 1043 K), Fe_3C (M_S ~169.3 emu/g; T_C = 483 K), and Fe_3O_4 (M_S = 92-100 emu/g; T_C = 850 K) [127-129]. The lower than expected value of the saturation magnetization has been attributed to the presence of the γ-Fe, which is reported to be antiferromagnetic below 50 K [12,13,56]. Since in this work it is observed quite low relative abundances of γ-Fe, I suggest that geometric factors (grain size, shape, high surface/volume ratio), structural disorder, and surface effects, could contribute to the lowering of M_S below the expected value [130]. Furthermore, superparamagnetism in α-Fe crystallites below the critical dimension would tend to decrease the measured M_S. Nevertheless the measured M_S values are comparable to those reported in literature by Karmakar *et al.*, Dillon *et al.*, and Leonhardt *et al.* [51,56,59].

4.2 Iron-filled multiwalled carbon nanotubes surface functionalized with paramagnetic Gd (III): A candidate dual-functioning MRI contrast agent and magnetic hyperthermia structure

In addition to filling the central capillary of CNTs with magnetic structures, benefits can be gained by surface functionalization of the inert sidewalls. Generally, covalent and non-covalent modifications are frequently used to functionalize the CNT surface [28].

In this section it is shown a simple wet chemical method involving only sonication in aqueous $GdCl_3$ solution to functionalize Fe-MWCNTs with gadolinium. Mild sonication of MWCNTs in deionized water is known to oxidise existing –CHn groups on outer walls, initially to –OH then to -C=O and finally to –COOH depending on the degree of local energy density delivered to the surface by the sonication [32]. Functional groups on the sidewalls produced by the sonication provide active nucleation sites for the loading of Gd^{3+} ions. Characterization by EPR, EELS, and HRTEM confirmed the presence of Gd^{3+} ions on the sidewall surface. The room temperature ferromagnetic properties of the encapsulated iron nanowire, saturation magnetization of 40 emu/g and coercivity 600 Oe, were

maintained after surface functionalization.

The advantage of mild pH and sonication conditions has the benefits; (i) the magnetic properties of Fe-MWCNTs are maintained after surface functionalization, which will otherwise be destroyed if a conventional acid treatment process was applied, and (ii) the method does not involve the additional use of amphiphilic surfactant molecules or polymers which could affect the biological response.

Also, it is demonstrated that Fe-MWCNTs surface-functionalized with gadolinium are candidate hybrids for dual-functioning magnetic hyperthermia cancer therapy and MRI contrast agent structures owing to integration of both the heating element (Fe) and the paramagnetic Gd (III). The claim of suitability for the magnetic hyperthermia application is made on the basis of measurement of SAR and ILP, whereas the claim of suitability for the MRI contrast agent functionality is made on the basis of direct observation of a room temperature electron paramagnetic resonance (EPR) signal that is the signature of lanthanide ions with a half filled sub-shell [33,34] and on the basis of measurement of relaxivity (r_1).

The presence of Gd^{3+} was assessed using EPR spectroscopy since the method is sensitive to paramagnetic ion content. Figure 4.8 shows the EPR spectra for gadolinium functionalized Fe-MWCNTs and unfunctionalized Fe-MWNTs, both measured at room temperature. The unfunctionalized Fe-MWCNTs signal exhibits a very weak and wide resonance in agreement with previous reports [131]. The gadolinium-functionalized Fe-MWCNTs signal is of the so-called U-spectrum type characterised by broad features [33].

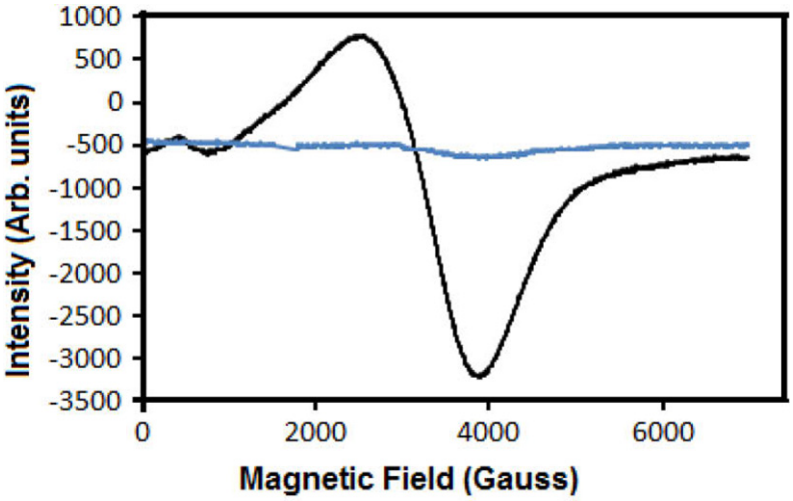

Figure 4.8: EPR spectra from powder samples of gadolinium-functionalized Fe-MWCNTs and unfunctionalized Fe-MWCNTs (blue line) at 300 K.

Only for lanthanide ions with a half filled sub-shell, $4f^7$ (Eu^{2+}, Gd^{3+}, Tb^{4+}), L = 0, S = 7/2, can an EPR signal be observed at room temperature [34]. I conclude that some gadolinium present in our sample is in the Gd^{3+} state. The signal broadening is usually attributed to the dipole–dipole interaction between the Gd^{3+} ions [132]. The spectrum can be considered as the superposition of two distinct signals arising: (i) isolated ions trapped at the defect sites of MWCNTs, (ii) and clustered ions [133]. It is reported that the shape of EPR spectrum for clusters is smeared by strong dipole–dipole interaction as well as exchange coupling between closely spaced Gd^{3+} ions [132].

To investigate the spatial distribution of gadolinium in the modified Fe-MWCNTs, it is performed scanning transmission electron microscopy-annular dark-field (STEM-ADF) imaging (a technique that is atomic number sensitive) in an aberration-corrected STEM with chemical mapping by EELS. The bright-field STEM images and high-angle annular dark field (HAADF) images confirm the presence of

gadolinium atoms in a surface layer of several nanometres thickness, Figure 4.9.

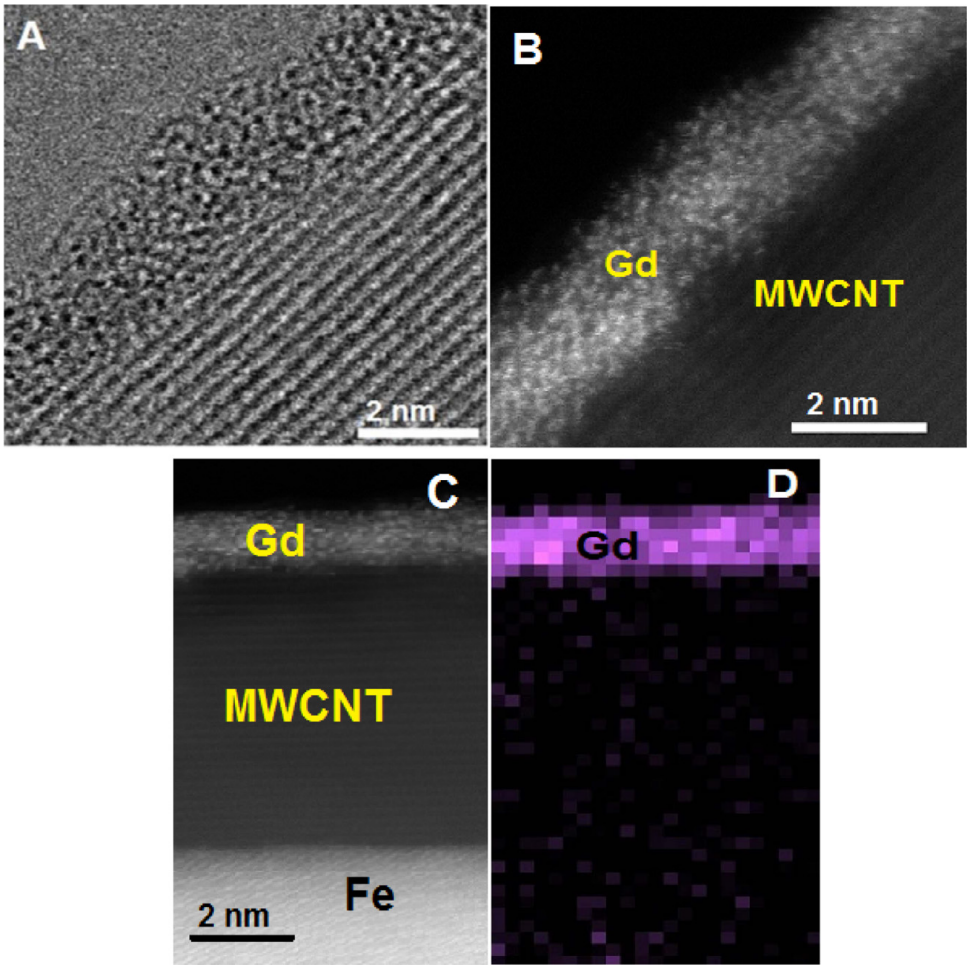

Figure 4.9: (A) Typical bright-field STEM image of a gadolinium-functionalised MWCNT surface, the parallel linear features are the pristine concentric graphitic sidewalls, the surface layer of several nanometres thickness is disordered. (B) Typical HAADF image of a similar view, the image contrast is an indication of an atomic number mismatch between the pristine MWCNT regions and the surface layer. (C) Typical HAADF image of the encapsulated Fe nanowire/pristine MWCNT/surface layer. (D) The chemical map for gadolinium of the area of image (C), the bright regions indicate high density.

Figure 4.10 (A) represent a HAADF image of the encapsulated Fe nanowire, pristine MWCNT and a surface layer which confirms the presence of gadolinium atoms in the surface layer of several nanometres thickness. In Figure 4.10 (B) is given the EELS spectrum taken on the area of the image (A) that shows the energy range of the gadolinium M-edge and the energy range of the iron L-edge.

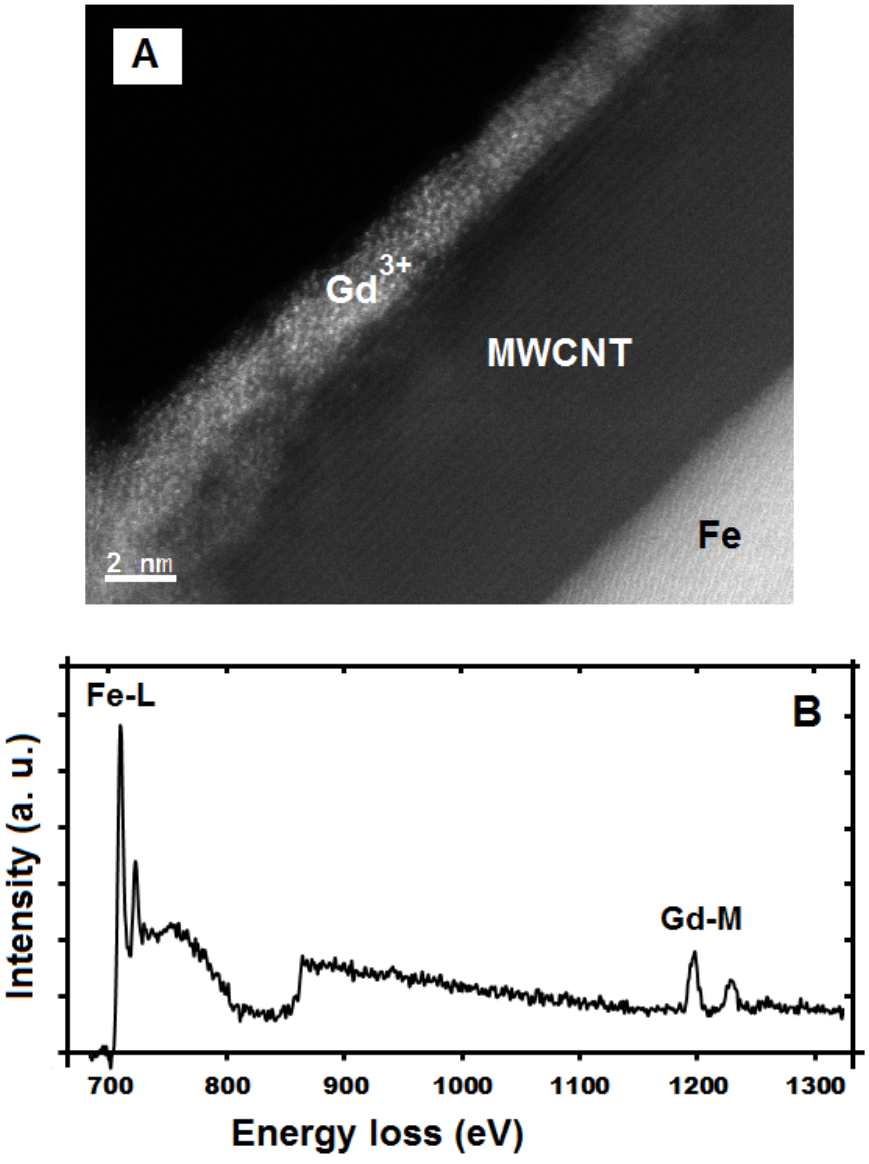

Figure 4.10: (A) Typical HAADF image of a gadolinium-functionalized Fe-MWCNT. (B) EELS spectrum taken at the area of the image A in the energy range of the gadolinium M-edge and iron L-edge.

Figure 4.11 (A) shows a bright-field image of a gadolinium-functionalized Fe-MWCNT; the EELS spectra taken from locations labelled 1 and 2 and in the clearly defined pristine MWCNT walls, labelled 3, Figure 4.11 (B and C).

The background to all spectra was subtracted by fitting a decaying power-law function to the energy window below the edge onset. The background subtraction is described in more details in Chapter 3.

The EELS spectrum obtained from the pristine MWCNT wall region closely corresponds with those reported in the literature [135]. The spectrum exhibits the spectral fingerprint of sp^2-hybridized carbon with high intensity peaks at 285 eV and 292 eV, corresponding to the excitation of a 1s core electron to the unoccupied π^* and σ^* orbitals, respectively.

In the spectrum obtained from location 1, both π^* and σ^* peaks from the carbon are also present but in contrast with the spectrum from pristine MWCNT region, the π^* peak intensity is reduced relative to the σ^* peak. A similar behaviour was observed in single-walled carbon nanotubes by X-ray absorption spectroscopy and was associated with the incorporation and release of C–O and C–H bonds [136]. This is consistent with a destruction of C–C π and σ bonds during the sonication treatment and the attachment of functional groups on the MWCNT sidewalls [27,32]. Furthermore, the decrease of the π^* peak intensity is accompanied by the smearing of the σ^* peak to the higher energy features at 293 eV characteristic of the pristine MWCNT. The slight decrease of the π^* peak could indicate that a small fraction of the carbon atoms form sp^3-type bonds with gadolinium atoms.

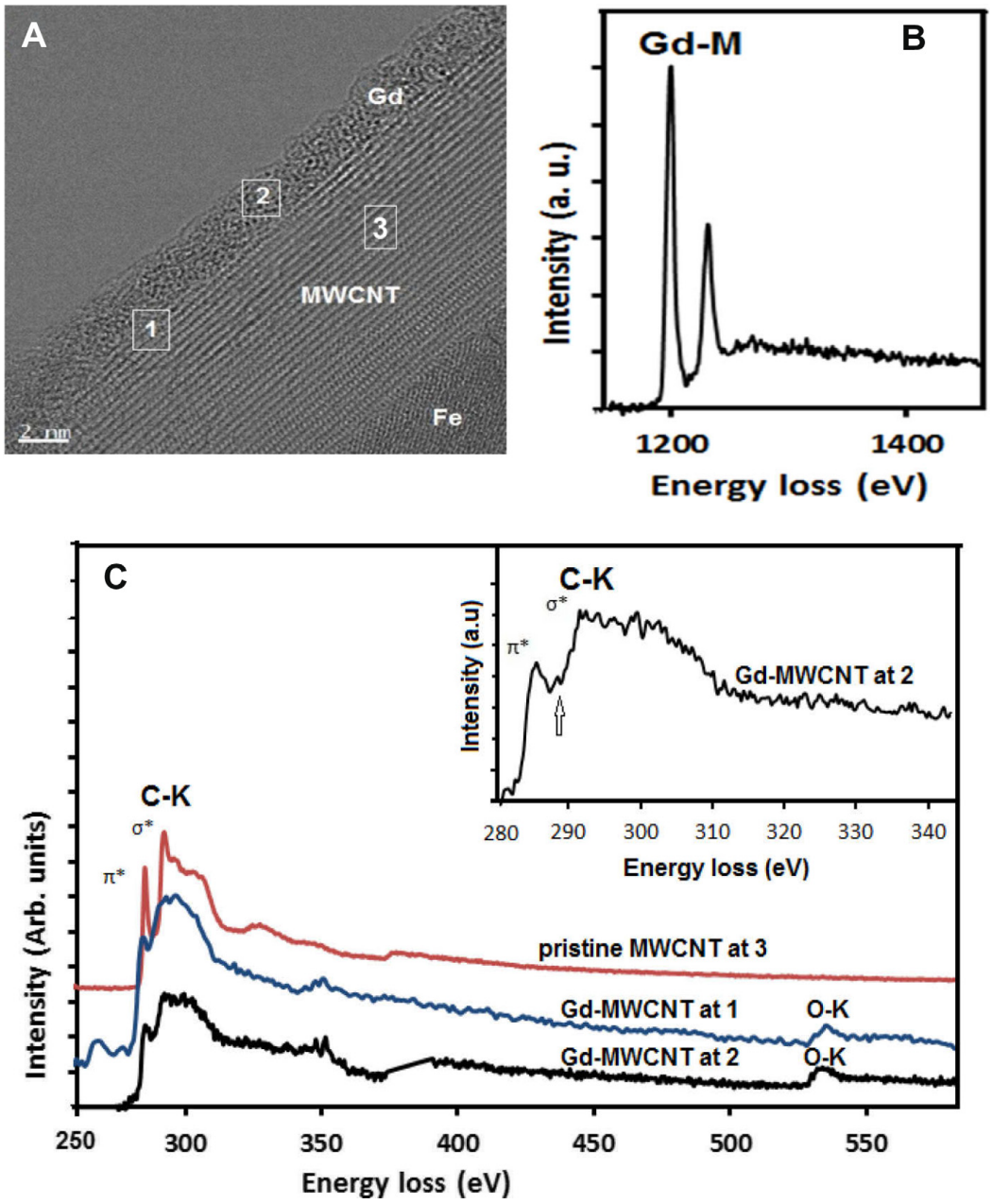

Figure 4.11: (A) Bright-field image of a gadolinium-functionalized Fe-MWCNT. (B) EELS spectrum taken at location 2 in the energy range of the gadolinium M-edge features (1.185 and 1.216 eV [134]) and (C) EELS spectra that shows the energy range close to the carbon K-edge and including the oxygen K-edge features recorded from the locations 1–3; the inset is an expansion of the location 2 spectrum, the arrow indicates the presence of a small peak at 288.4 eV. The signals were offset for ease of comparison.

This is consistent with the presence of the gadolinium in this location and with X-ray diffraction measurement which showed the presence of a small quantity (0.3%) of the gadolinium carbide phase, Figure 4.12.

A large decrease of the π^* and σ^* peaks intensity accompanied by a large broadening of the σ^* peak it is evident in the spectrum taken at location 2. Another interesting feature of this spectrum is the presence of a small peak at 288.4 eV, between the π^* and σ^* peaks which is shown with an arrow in the inset of Figure 4.11(c). Similar behaviour has been observed on previous X-ray absorption spectroscopy (XAS) studies of graphite oxide and doped graphene [137,138]. This observation supports the presence of the oxygenated groups on the sidewalls of the sonicated MWCNTs [27,32]. This is consistent with the presence of the broad oxygen K-edge feature at 535 eV which has been attributed to convolved signals from carboxyl and hydroxyl groups [139].

In contact with the water these functional groups deprotonate, thus leaving a negatively charged carbon surface [140]. The surface charge significantly improves the interaction between the MWCNTs and metal cations [140]. Since the functional groups attract the M^{x+} ions and the gadolinium in the sample is in the Gd^{3+} state, I conclude that it is the ionic interaction between the deprotonated carboxyl groups and Gd^{3+} ions that attaches the gadolinium to the MWCNT surface.

The X-ray diffraction (XRD) pattern obtained from gadolinium-functionalized Fe-MWCNT powder is shown in Figure 4.12.

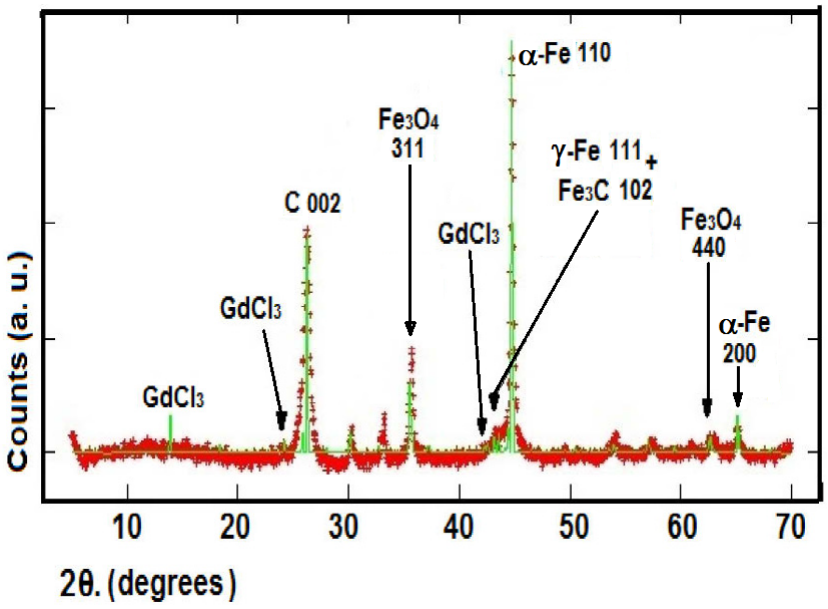

Figure 4.12: Typical X-ray diffractogram data (red line), and Rietveld refinement (green line) for gadolinium functionalized Fe-MWCNTs: the refinement was made with the following components γ-Fe (Fm-3 m, Crystal Open Database Ref. 9008469), α-Fe (Im-3 m, Crystal Open Database Ref. 64998), Fe_3C (Pmna, Crystal Open Database Ref. 16593), graphite (representing MWCNTs) (P63/mmc, Crystal Open Database Re. 53781), Fe_3O_4 (space group Fd-3 m), $GdCl_3$ (P63/m, Crystal Open Database Ref. 15387), and Gd_2C_3 (I-43d, Crystal Open Database Ref. 109323).

Rietveld analyses of the XRD diffractogram was used to determine the relative abundances of the components of the sample revealed α-Fe (bcc) as the dominant encapsulated Fe phase and minor presence of γ-Fe (fcc) and iron carbide (Fe_3C). The analysis also revealed the presence of the iron oxide (Fe_3O_4), gadolinium chloride ($GdCl_3$), and a small amount of gadolinium carbide (Gd_2C_3): there is no HAADF evidence for these compounds as encapsulated phases or surface- bound groups; I conclude that these components are external to the Fe-MWCNTs. The

relative weight abundances were found to be: 0.5% γ-Fe, 24% α-Fe, 0.6% Fe_3C, 65% MWCNTs, 8% Fe_3O_4, 1.5% $GdCl_3$, 0.3% Gd_2C_3.

Magnetic properties of Gd^{3+}-functionalized Fe-MWCNTs powder were investigated at 5 and 300 K. The magnetic field dependence of the magnetization is presented in Figuren 4.13. At both temperatures 5 and 300 K, the encapsulated iron exhibited ferromagnetic hysteresis. The results indicate that saturation magnetization and coercivity of the the encapsulated iron at 5 K were 42 emu/g and 930 Oe respectively whereas at room temperature a saturation magnetization of 40 emu/g and a coercivity of 600 Oe were observed.

These results show a decrease in saturation magnetization and coercivity with increasing temperature from 5 to 300 K. The main reason of this temperature dependence must originate from thermal fluctuations. Some of the encapsulated nanowires can become superparamagnetic at room temperature.

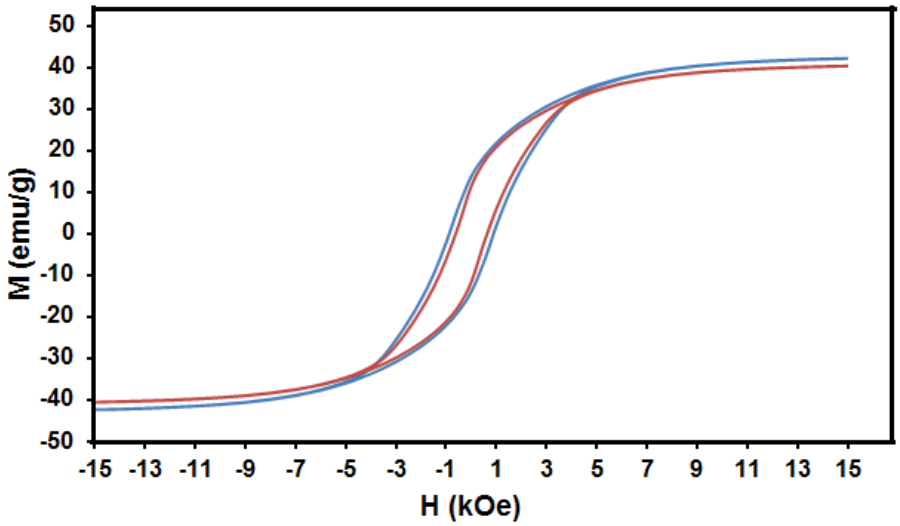

Figure 4.13: The field dependence of dc magnetization for Gd^{3+}-functionalized Fe-MWCNTs powder at $T = 5$ K (blue line) and at $T = 300$ K (red line).

Maintaining ferromagnetic properties of the encapsulated iron after the surface functionalization is crucial for application of this material in magnetic hyperthermia cancer therapy.

In conclusion, in this subsection it is demonstrated a simple wet chemical method involving only sonication in aqueous $GdCl_3$ solution to functionalize Fe-MWCNTs with gadolinium. This method results in loading of Gd^{3+} ions on the MWCNTs surface due to the ionic interaction between the Gd^{3+} ions and the deprotonated carboxyl groups created on the MWCNT sidewalls during the sonication process. The ferromagnetic properties of the encapsulated iron nanowires maintained after surface functionalization.

4.2.1 Gd^{3+}-functionalized Fe-MWCNTs potential high relaxivity contrast agents for high-field imaging

The clinically used Gd^{3+} complexes such as Gd-DOTA, Gd-DTPA and their derivatives, have low relaxivities with r_1 values of only 4-5 $mM^{-1}s^{-1}$ measured at magnetic field strength of 1.5 T [91]. Further development of contrast agents with high relaxivity and low toxicity are crucial for the early accurate diagnosis of the pathological tissues. Also, currently, the most efficient T_1 agents show a typical high-field relaxivity peak centred at 0.7 - 0.94 T [94]. Above this field, the longitudinal relaxivity (r_1) of current MRI contrast agents strongly decreases with increasing field.

With increasing field strength, the level of image signal in relation to image noise, known as the signal-to-noise ratio (SNR) improve significantly [8]. The increase in

the SNR may be used either to acquire images with increased spatial resolution, to accelerate the sequence acquisition, or some combination thereof.

The need for higher spatial resolution, higher speed imaging and better sensitivity led to the development of clinical high-field MRI systems. The highest field strength utilized in the clinical routine today is 3 T. Recently, human whole body scanners with field strengths beyond 7 T have been installed, but these are still utilized primarily for experimental, preclinical purposes. The preliminary results of the first human images at the new high-field benchmark of 9.4 T have been reported by Vaughan and co-workers [8]. These results demonstrated the feasibility of safe and successful human imaging at 9.4 T [8].

So new contrast agents need to be specifically tailored to fully exploit the benefits of high-field MRI.

In this subsection it is demonstrated that, Gd^{3+} functionalized-Fe-MWCNTs are powerful proton relaxation centres with relaxivity r_1 value of 50 times greater than any Gd^{3+} - based contrast agents in clinical use. The measurement was performed using magnetic field strengths 9.4 T and 14 T to assess viability as contrast agent for high-field imaging.

The relaxation times were measured at two different magnetic field strengths: 9.4 T and 14 T and the inversion-recovery method was used to measure T_1. Figure 4.14 (A,B) and Figure 4.15 show the magnetisation recovery curves of the main peak (4.596 ppm) of [(D_2O + SDBS) + Gd^{3+} functionalized-Fe-MWCNTs], (D_2O + SDBS) and [(D_2O + SDBS) + Fe-MWCNTs] at 9.4 T and the obtained T_1 values were 9 s, 14.08 s and 13.3 s respectively.

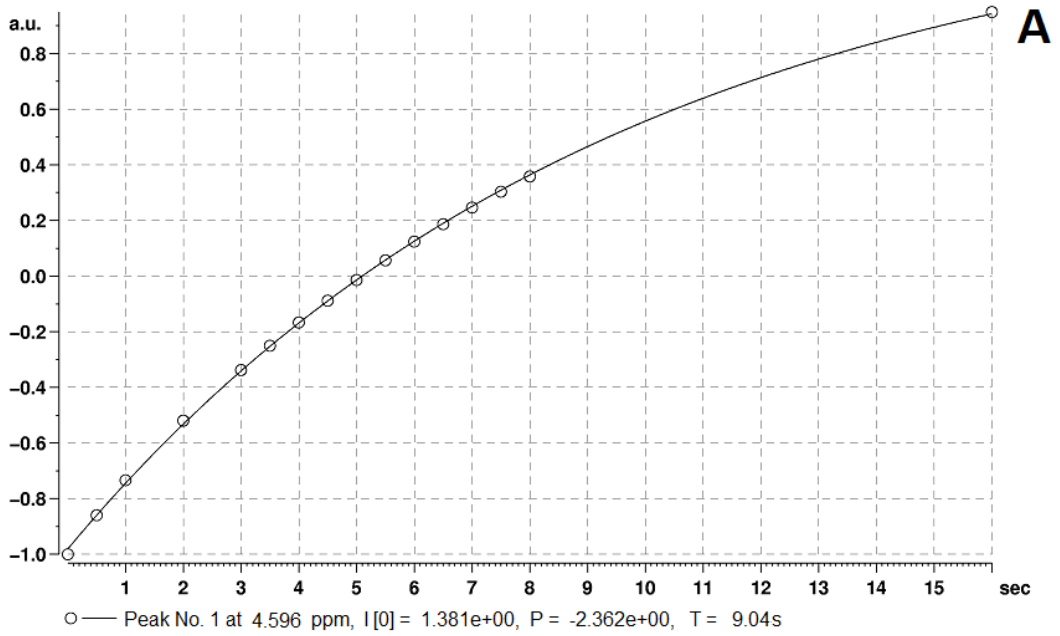

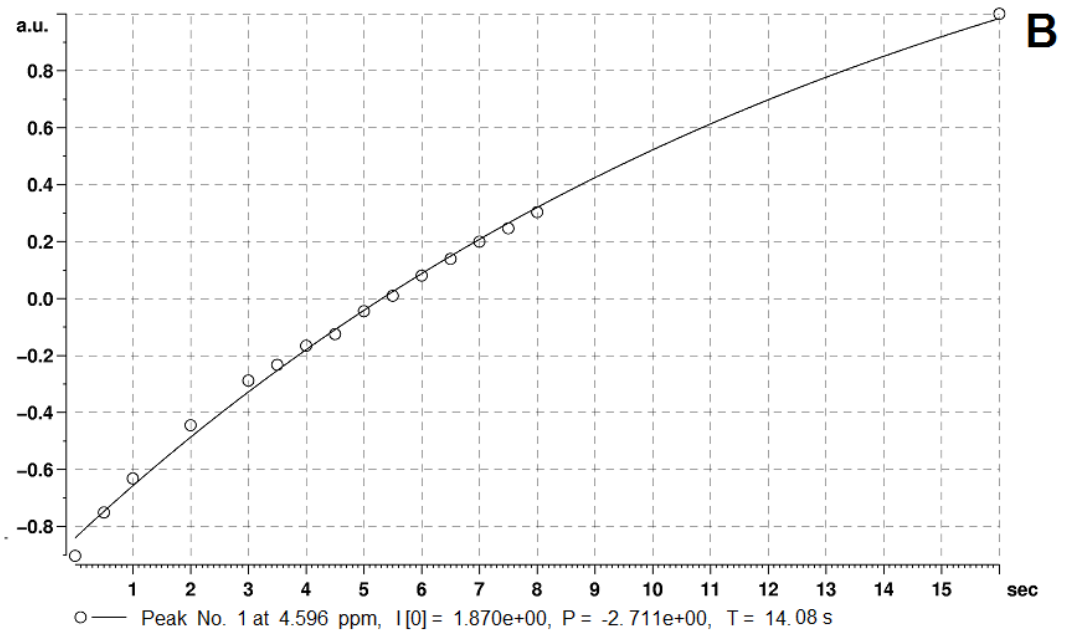

Figure 4.14: The magnetization recovery curve plot of [(D_2O + SDBS)+ Gd^{+3} functionalized-Fe-MWCNTs] (A) and (D_2O + SDBS) (B) by inversion recovery method at 9.4 T. The solid line is the fit to equation: $I[t] = I[0] + \mathrm{P} \times \exp(\frac{-t}{T_1})$ where $I[0]$ is the magnetisation intensity in equilibrium and $I[t]$ is the magnetisation at time t.

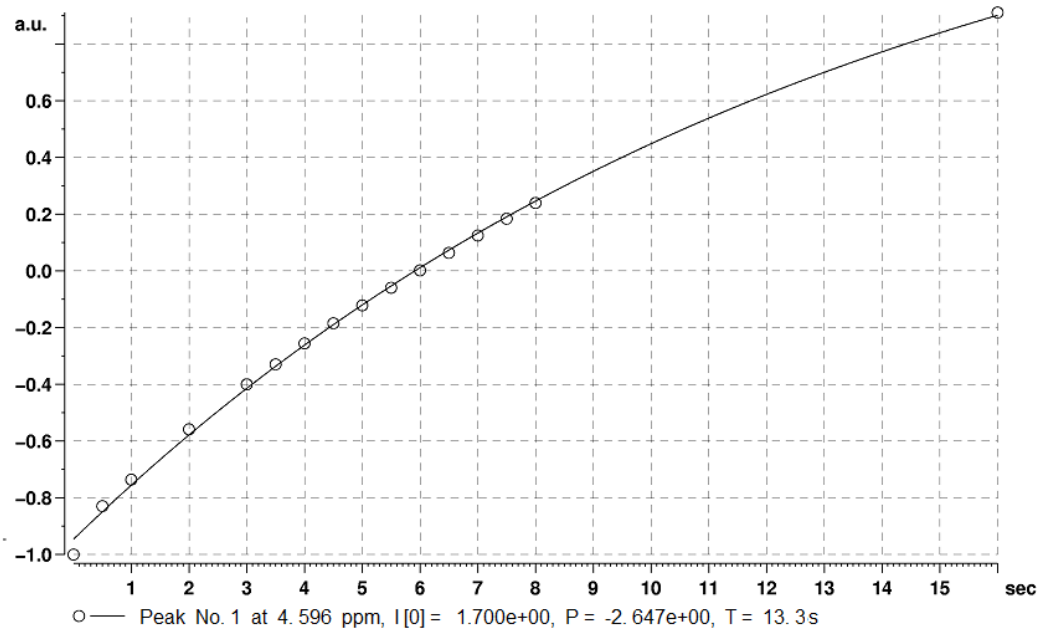

Figure 4.15: The magnetization recovery curve plot of [(D_2O + SDBS)+ Fe-MWCNTs] by inversion recovery method at 9.4 T. The solid line is the fit to equation: $I[t] = I[0] + \mathrm{P} \times \exp(\frac{-t}{T_1})$ where $I[0]$ is the magnetisation intensity in equilibrium and $I[t]$ is the magnetisation at time t.

The longitudinal relaxivity (r_1) was calculated by:

$$T_{1\mathrm{obs}}{}^{-1} = T_{1\mathrm{d}}{}^{-1} + r_1[\mathrm{Gd}^{3+}], \tag{4.1}$$

where $T_{1\mathrm{obs}}$ and $T_{1\mathrm{d}}$ are the relaxation times (in seconds) of the sample and the matrix (D_2O + SDBS) respectively, and [Gd^{3+}] is the Gd concentration in mM. The results of the relaxation time measurements and relaxivity calculation are given in the tables below.

Table 2. Proton relaxivity r_1 of the sample solutions at 9.4 T and 30 ^{0}C.

Sample	[Gd^{3+}](mM)	T_{1obs}(s)	T_{1d}(s)	r_1($mM^{-1}s^{-1}$)
Gd^{3+}-Fe-MWCNTs	0.2×10^{-3}	9	14.08	200.5
Fe-MWCNTs	-	13.3	14.08	-

Table 3. Proton relaxivity r_1 of the sample solutions at 14 T and 30 ^{0}C.

Sample	[Gd^{3+}](mM)	T_{1obs}(s)	T_{1d}(s)	r_1($mM^{-1}s^{-1}$)
Gd^{3+}-Fe-MWCNTs	0.2×10^{-3}	9.8	14.30	160.5
Fe-MWCNTs	-	13.4	14.30	-

As can be seen from results shown on the tables, the Gd^{3+} functionalized Fe-MWCNTs significantly decrease T_1 relative to that of pure solution. It should be noted that the only Fe-MWCNTs without Gd^{3+} do not have a sufficient influence on the longitudinal relaxation rate of the surfactant solution. I observed that the relaxivities slightly decrease with increasing field strength from 9.4 T to 14 T but the order of magnitude was always the same.

The r_1 value of the Gd^{3+} functionalized Fe-MWCNTs is 50-60 times greater than Gd^{3+} - based contrast agents in clinically use, such as Gd-DOTA and Gd-DTPA with r_1 values of only 3-4 mM^{-1} s^{-1} measured at high magnetic field (9.4 T) and twenty times greater than that for metallostar $\{Fe[Gd_2bpy(DTTA)_2(H_2O)_4]_3\}^{4-}$, $r_1 \sim 9$ mM^{-1} s^{-1} at 9.4 T [7], much greater than superparamagnetic iron oxide (Resovist) clinically approved contrast agent with $r_1 \sim 1.67$ mM^{-1} s^{-1} measured

at field strength of 9.4 T [141]. Furthermore, to my knowledge a relaxiviy value of 200 Mm^{-1} s^{-1} is greater than that of any reported relaxivity r_1 values measured at high magnetic fields (9.4 - 14 T). The high magnetic field relaxivity value for superparamagnetic gadonanotubes reported by Sitharaman *et al.* was $r_1 \sim 170$ mM^{-1} s^{-1} [62]. The comparable value reported here is likely to be underpinned by similar factors, namely, the large number of the co-ordinated water molecules per Gd^{3+} ion and short Gd–H distances [68,142]. The greater relaxivity observed for Gd^{3+} functionalized Fe-MWCNTs is likely to be a consequence of the greater molecular weight resulting in an increase in the rotational correlation time and therefore in proton relaxivity [100].

In conclusion, I have shown in this subsection, that Gd^{3+} functionalized Fe-MWCNTs are high relaxivity MRI contrast agents for high field imaging with $r_1 \sim 200$ mM^{-1} s^{-1} at magnetic field 9.4 T.

4.2.2 Gd^{3+}-functionalized Fe-MWCNTs potential candidates for magnetic hyperthermia cancer therapy

The heating of tissue using magnetic nanoparticles has a great potential as a new treatment approach for cancer therapy, involving the targeted administration of magnetic nanoparticles into the body, accumulation of those nanoparticles at sites of cancer, and the local heating of those magnetic nanoparticles with an externally applied AC magnetic field.

In this subsection it is shown the potential of Gd^{3+}-functionalized Fe-MWCNTs for magnetic heating in hyperthermia cancer treatment.

The claim of suitability for the magnetic hyperthermia application is made on the basis of measurement of SAR and ILP.

The heating efficiency of the sample was tested in an alternating magnetic field of frequency 696 kHz and strength of 8 kA/m. The inductive heating study shown in Figure 4.16 reveals a substantial heating effect of Gd^{3+}-functionalized Fe-MWCNTs in AC magnetic field.

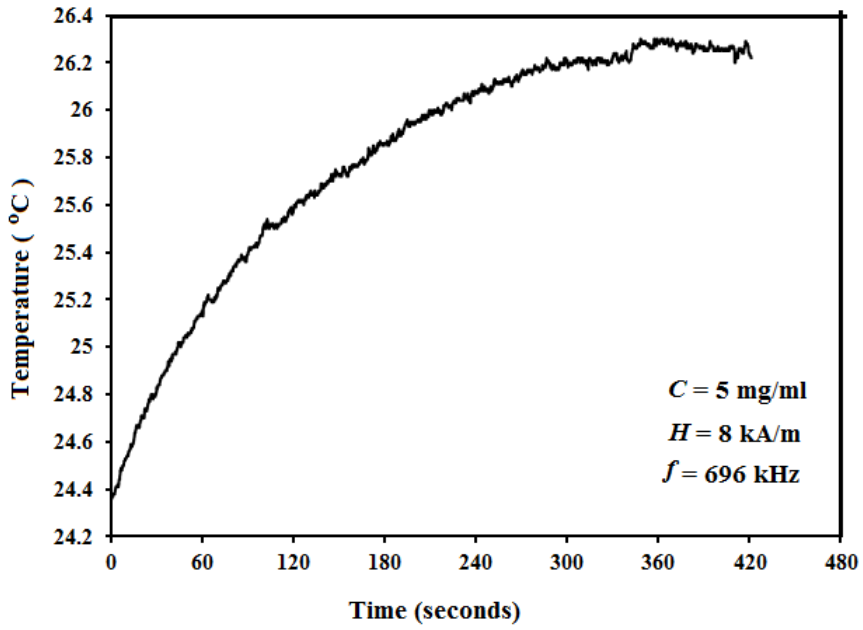

Figure 4.16: The heating effectiveness of Gd^{3+}-functionalized Fe-MWCNTs in AC magnetic field. C is the sample concentration.

SAR was calculated from Equation (2.8) using c, the specific heat capacity of the sample, set equal to that of water (4.186 J g^{-1} K^{-1}) and $\frac{dT}{dt}|_{t\to 0}$ determined from the initial slope of the temperature versus time curve (see Figure 4.16), to be 50 W/g_{Fe}, where the g_{Fe} denotes the mass of the iron obtained through the relative abundances determined by Rietveld analyses of the XRD diffrac-

togram (Figure 4.12). The estimated value of ILP from Equation (2.9), was 1.12 nHm^2kg^{-1}.

At 5 K the encapsulated iron exhibited ferromagnetic hysteresis with the saturation magnetization of 42 emu/g (42 Am^2/kg) and a coercivity of 930 Oe (74 kAm^{-1}). Theoretically, the generated heat is quantitatively described by the equation SAR $= A \times f$ in which f is the frequency of the applied field and A is the hysteresis area. Based on the Stoner-Wohlfarth (SW) model for magnetic nanoparticles with their easy axes randomly oriented in space, the hysteresis area is calculated by $A = 2\mu_0 H_C M_S$ [143]. The H_C and M_S for our sample were 74 kAm^{-1} and 42 Am^2/kg respectively. (Note the 42 Am^2 is per kg sample of Gd^{3+}-functionalized Fe-MWCNTs). According to the above equations and assuming $f = 120$ kHz I found the theoretical value of SAR for my sample to be 4260 $W/g_{\alpha-Fe}$ where the g_{Fe} denotes the mass of the iron obtained through the relative abundances determined by Rietveld analyses of the XRD diffractogram (Figure 4.12). The estimated theoretical value of ILP from Equation (2.9) was 6 nHm^2kg^{-1} which is much higher than experimental value.

In case of ferromagnetic particles produced in this work, to exploit their heating potential it is required a frequency of few hundred kHz and a relatively high field amplitude that exceed their coersivity field (>74 kAm^{-1}), since at this field strength they approach a fully saturated loop (previously described in Chapter 2). At field strength of 8 kAm^{-1} used in my measurements, only minor hysteresis loops can be utilized for heating, resulting to lower ILP than theoretical value. However, my ILP value of 1.12 nHm^2kg^{-1} is comparable with that of some tested

commercial ferrofluids such as Chemicell fluidmag-D50nm with a ILP value of 1.31 nHm^2kg^{-1} [77] and Chemicell fluidmag NY-D200nm with ILP value of 1.53 nHm^2kg^{-1} [144], lower than the ILP value of 3.1 nHm^2kg^{-1} obtained from Bayer-Schering's Resovist, but much higher with respect to the ILP values obtained for samples from Micromod such as Nanomag-D-spio-250nm and Nanomag-D-spio-130nm with ILP values of 0.37 and 0.23 nHm^2kg^{-1} respectively [76].

In conclusion, I have demonstrated in this subsection that Gd^{3+}-functionalized Fe-MWCNTs are potential candidates for magnetic hyperthermia cancer therapy with a SAR value of 50 W/g_{Fe} and a ILP value of 1.12 nHm^2kg^{-1}.

4.3 A facile method for self-organized texturing of iron-filled multiwalled carbon nanotube arrays

One of the objectives of this project was the development of MWCNTs for magnetic hyperthermia application which is achieved by filling them with continuous α-Fe nanowires. As discussed earlier, besides filling MWCNTs with continuous, completely α-Fe nanowires, length and diameter control of both nanowire and nanotube of Fe-MWCNTs is desirable for magnetic hyperthermia application. In section 4.1, it is outlined a systematic study of length-diameter, and nanowire content based on a low vapour flow-rate and constant evaporation temperature CVD method.

In this section I demonstrate a facile CVD-based method for the texturing of

Fe-MWCNTs vertical arrays by exploitation of the interplay of temperature gradients and modulated vapour flow which imposed annular height variation and a vertical-array-to-spherulitic morphological transformation. The method imposed well-defined annular features on the height of the vertical array, while continuity of the iron nanowire on the micrometre scale was maintained.

The substrates, conditions of temperature, and flow rate chosen for the growth of these textured arrays were those previously used to produce uniform, close-packed arrays of iron-filled carbon nanotubes of constant height in an unmodulated vapour flow. I speculate that the observed annular height variation results from creation of stationary cells of feedstock vapour above the growth front. In conditions of higher substrate temperature and less modulated vapour flow the presence of the stationary cells impacts on the iron island formation process to produce a morphological transformation from array to spherulitic agglomeration.

Arrays of Fe-MWCNTs were grown on smooth Si/SiO_2 substrates held in the reaction zone of a horizontal CVD reactor. The source vapour was produced by the sublimation of ferrocene powder arranged in rows of approximately equal width and separation arranged parallel to the flow of argon carrier gas. The schematic diagram of the reactor and the experimental details of the growth process are discussed in Chapter 3.

Figure 4.17 and Figure 4.18 (A-C) show representative SEM images of the top view of the array found on substrate A showing 150 μm – 400 μm diameter annular features. These are found in random locations with a mean separation of

500 μm. Figure 4.18 (D, E) are two example cross-sectional SEM images taken through the outer ring of the annular features: D and E clearly indicate a stepwise variation of height of which can be greater or less than that of the neighboring array.

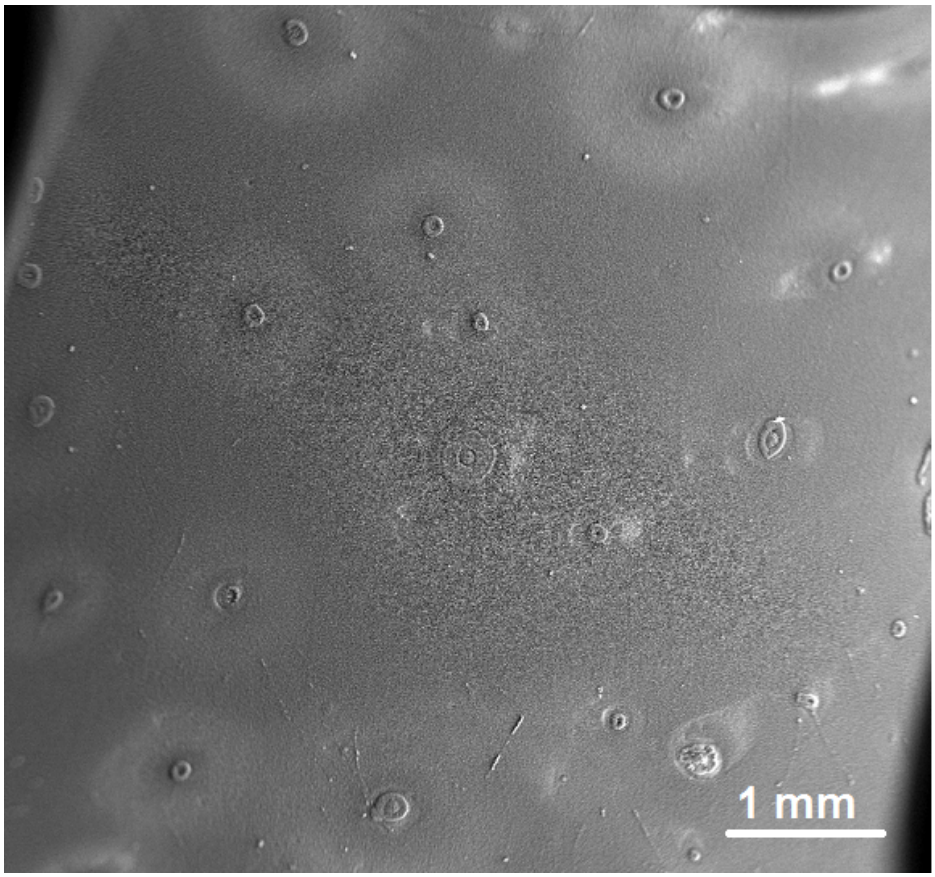

Figure 4.17: Example SEM image of as grown Fe-MWCNTs arrays showing the top-view of the annular features imposed on the array.

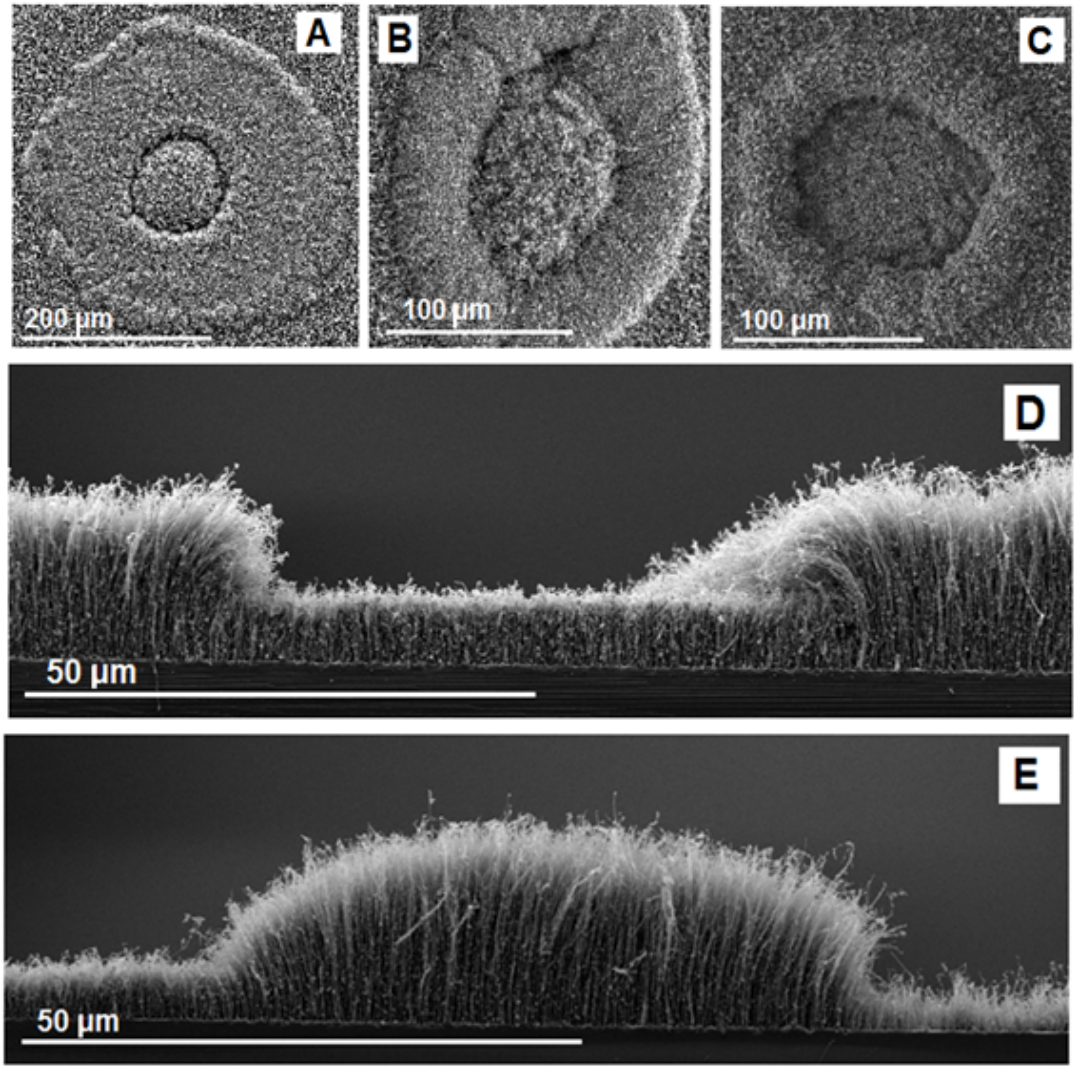

Figure 4.18: Example SEM images of as grown Fe-MWCNTs arrays. A-C show the top-view of the annular features imposed on the array. D and E are example array/substrate interface cross-sectional views taken through the ring of two annuli. The stepwise variation of height in the closely packed vertically aligned filled MWCNTs clearly indicates that the height of the annulus ring can be greater or lower than that of the neighboring array.

Filling of the MWCNTs on micrometre length-scale was confirmed by SEM and TEM investigation of material mechanically removed from the substrate, Figure 4.19.

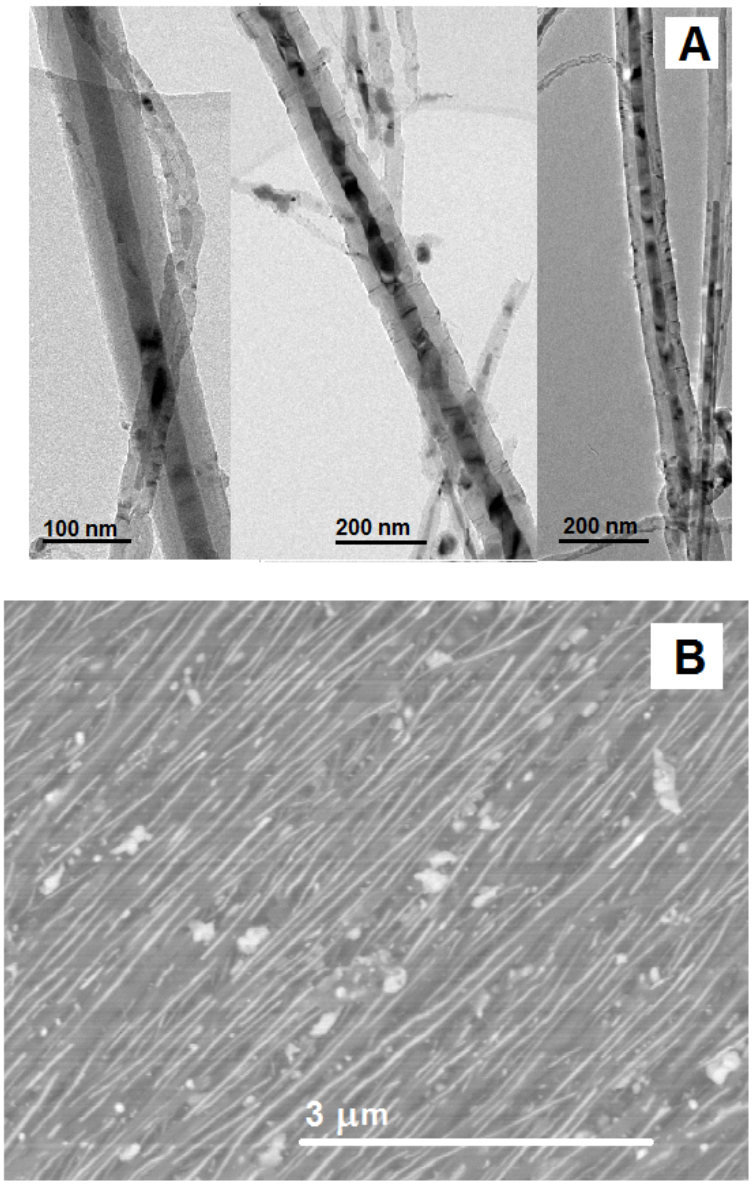

Figure 4.19: TEM image of structures mechanically removed from substrate A showing contrast between the encapsulated iron nanowires and the outer MWCNTs (A). The iron-filling of MWCNTs was also confirmed by backscattered SEM image (B) (brighter regions).

Compositional analysis of as-grown structures was performed by Rietveld analyses of XRD data, Figure 4.20. The common peak at 26.2° corresponds to the characteristic 002 reflection of graphitic carbon structure of the MWCNTs, the

symmetry and the narrowness of this peak are indicative of the high degree crystallinity. The main encapsulated phases were revealed to be: α-Fe, γ-Fe and Fe_3C. The presence of the α-Fe in the sample is revealed by observation of the 110 and 200 reflections at 44.8° and 65°, respectively, while the presence of the γ-Fe is revealed by the 111 reflection at 43.8°. The 200 reflection which indicates Fe_3C phase was observed at 35.3°. The relative weight abundances were found to be: 3% γ-Fe, 7% Fe_3C, 30% α-Fe, 51% MWCNTs and 9% Fe_3O_4.

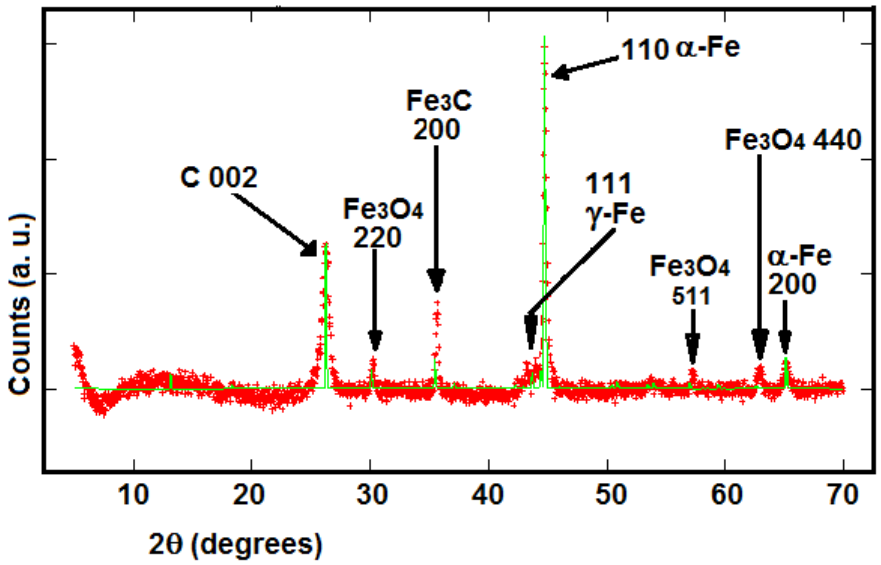

Figure 4.20: Typical X-ray diffraction data (red) and Rietveld refinement (green) of iron-filled MWCNTs arrays. The refinement was made with the following components α-Fe (Im-3m, Crystal Open Database Ref. 64998), γ-Fe (Fm-3m, Crystal Open Database Ref.9008469), Fe_3C (Pmna, Crystal Open Database Ref. 16593), graphitic carbon (P63/mmc, Crystal Open Database Ref. 53781), Fe_3O_4 (space group Fd-3m). The origin of oxide components is oxidation of residual elemental iron when the sample is removed from the reactor and handled in air.

TEM and SAED investigations of Fe-MWCNTs arrays, also confirm the presence of α-Fe nanowires inside MWCNTs (see Figure 4.21). In the SAED, the yellow circles indicate the 002 and 004 diffraction spots of graphitic MWCNTs corresponding to a lattice spacing of 0.34 and 0.17 nm respectively. The red circles indicate the 211 diffraction spots of α-Fe corresponding to a lattice spacing of 0.12 nm, while the green circles indicate the 310 diffraction spots of α-Fe corresponding to a lattice spacing of 0.09 nm.

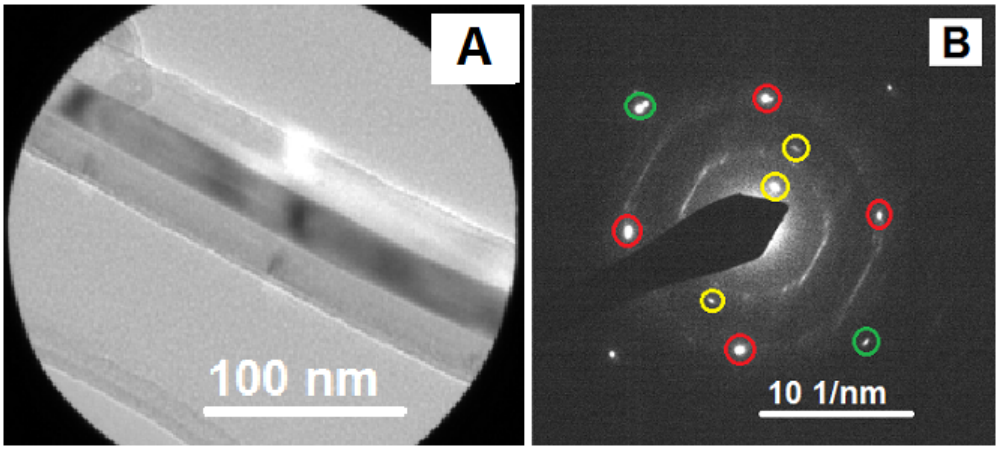

Figure 4.21: Transmission electron micrograph (A) showing typical MWCNT filled with α-Fe and (B) corresponding selected area electron diffraction. In (B) the SAED pattern of the filling structure reveals the reflections of the bcc iron: the red and green circles indicate the 211 and 310 reflections of α-Fe, respectively. The yellow circles indicate the 002 and 004 reflections originated from MWCNTs.

The morphology of the array deposited on substrate B showed aggregated regions of clustered spherulites ($\sim$10 μm diameter radial structures comprising hundreds of nanotubes departing from a central particle) in an otherwise vertically aligned array, Figure 4.22. The clustered regions were of several hundred

micrometres diameter (Figure 4.22 A and B). Details of individual spherulites are given in Figure 4.23 A and B.

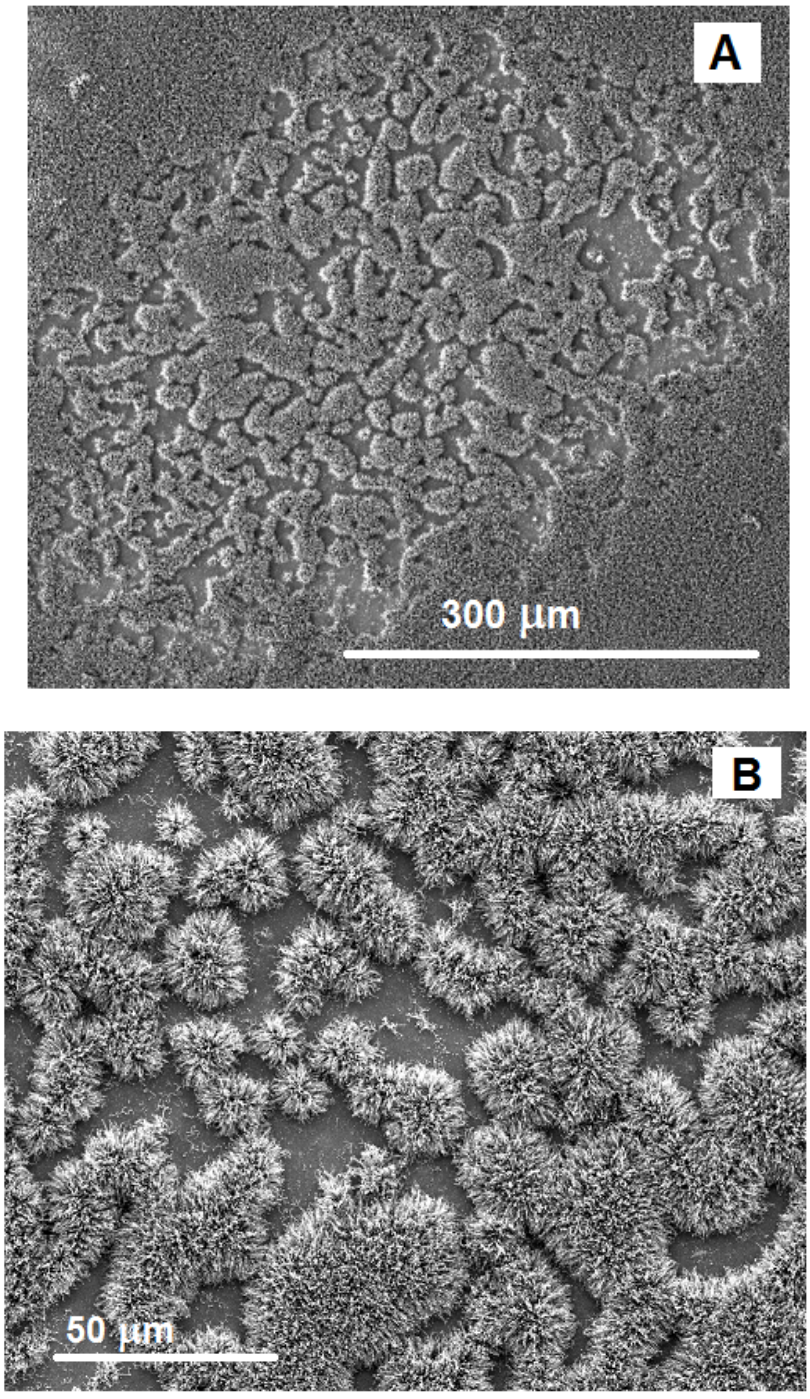

Figure 4.22: SEM images of the aggregated regions found on substrate B: (A) at low magnification and (B) at high magnification.

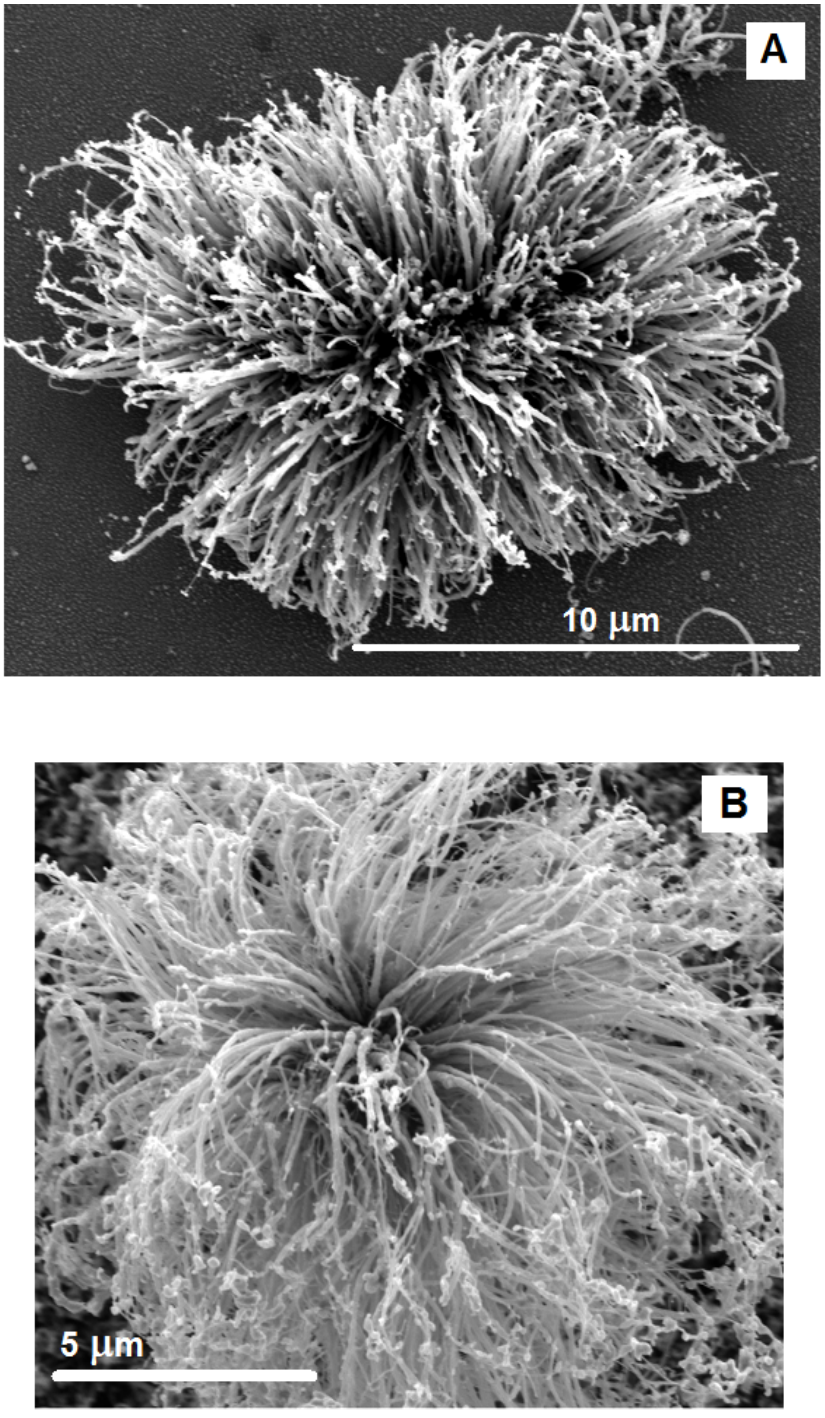

Figure 4.23: SEM images of individual spherulites (A and B) comprising hundreds of nanotubes departing from a central particle, found on substrate B.

EDX analyses of the aggregated regions were performed on substrate-supported samples to investigate the distribution of the elements present in the product. Fig-

ure 4.24 is an example of an aggregated region (A) and associated EDX spectrum (B). The relative abundances were found to be carbon (56%), iron (29%); the remaining 15% embraces the silicon and oxygen signals from the substrate and trace levels of dysprosium which might be the contamination from microscope.

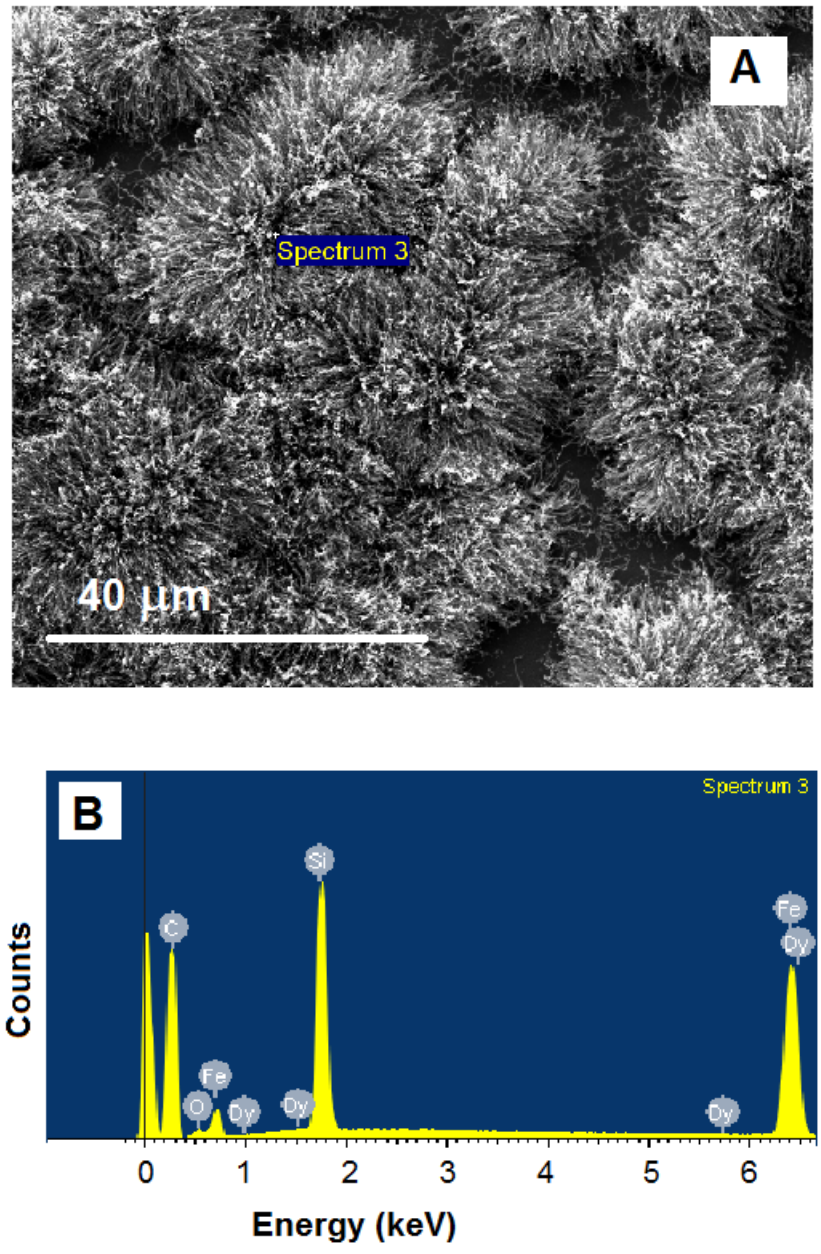

Figure 4.24: Example SEM image of aggregated spherulite region (A) and associated EDX spectrum (B).

Individual and aggregated regions of unfilled carbon nanotube spherulites were first reported by Zhang *et al.* [145]. Here, the iron-to-carbon ratio revealed by the EDX analysis (∼1:2) is greater than that in the source ferrocene molecule (1:10) suggesting that the central particle a nucleating iron island.

MWCNTs filled with iron nanowires on micrometre length-scale were also observed by backscattered SEM images of as grown carbon nanotube spherulites on substrate (Figure 4.25) and TEM investigation of material mechanically removed from the substrate (Figure 4.26).

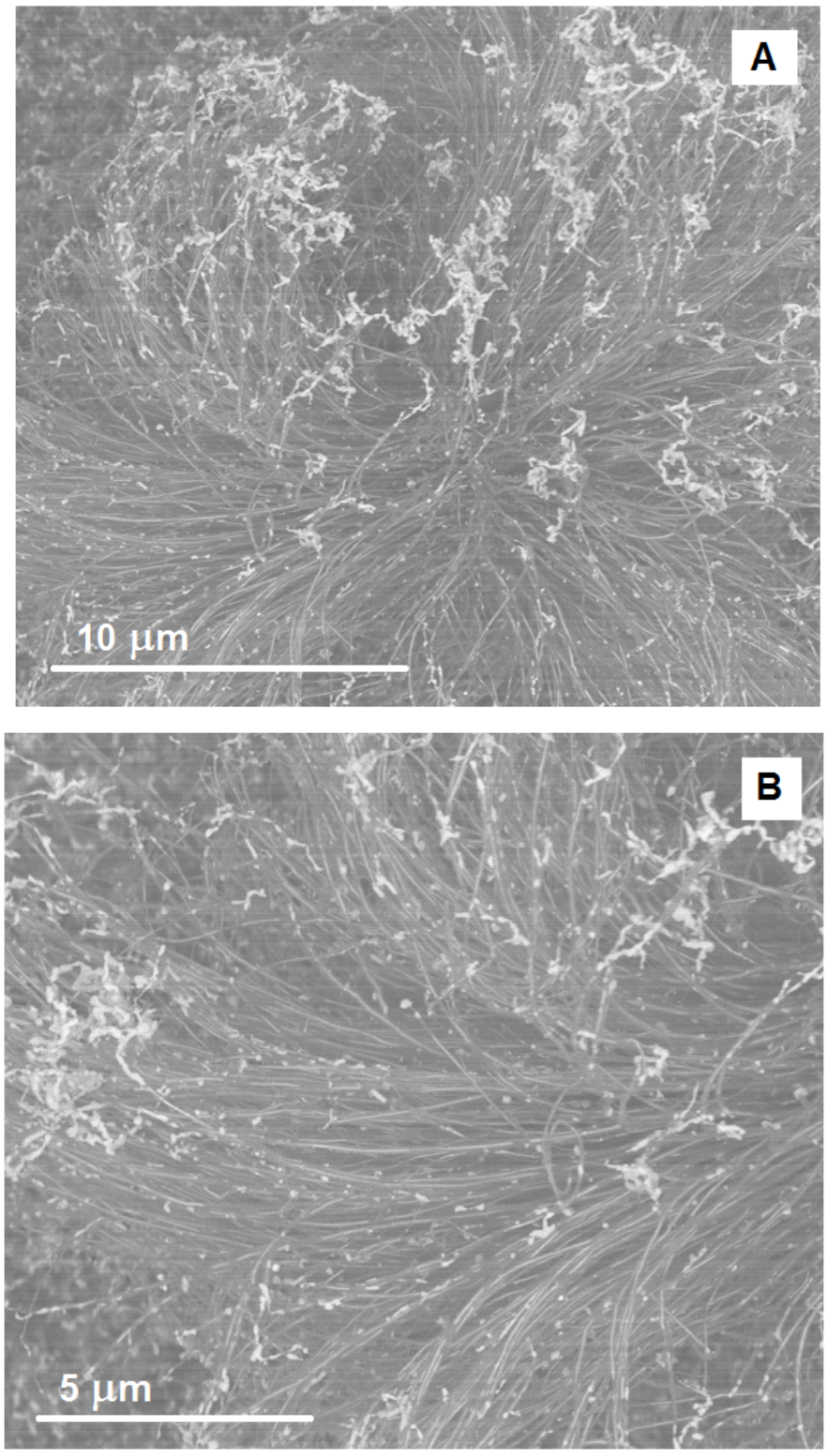

Figure 4.25: Backscattered SEM images of Fe-MWCNTs spherulites showing the encapsulated iron nanowires (brighter regions): (A) at low magnification and (B) at high magnification.

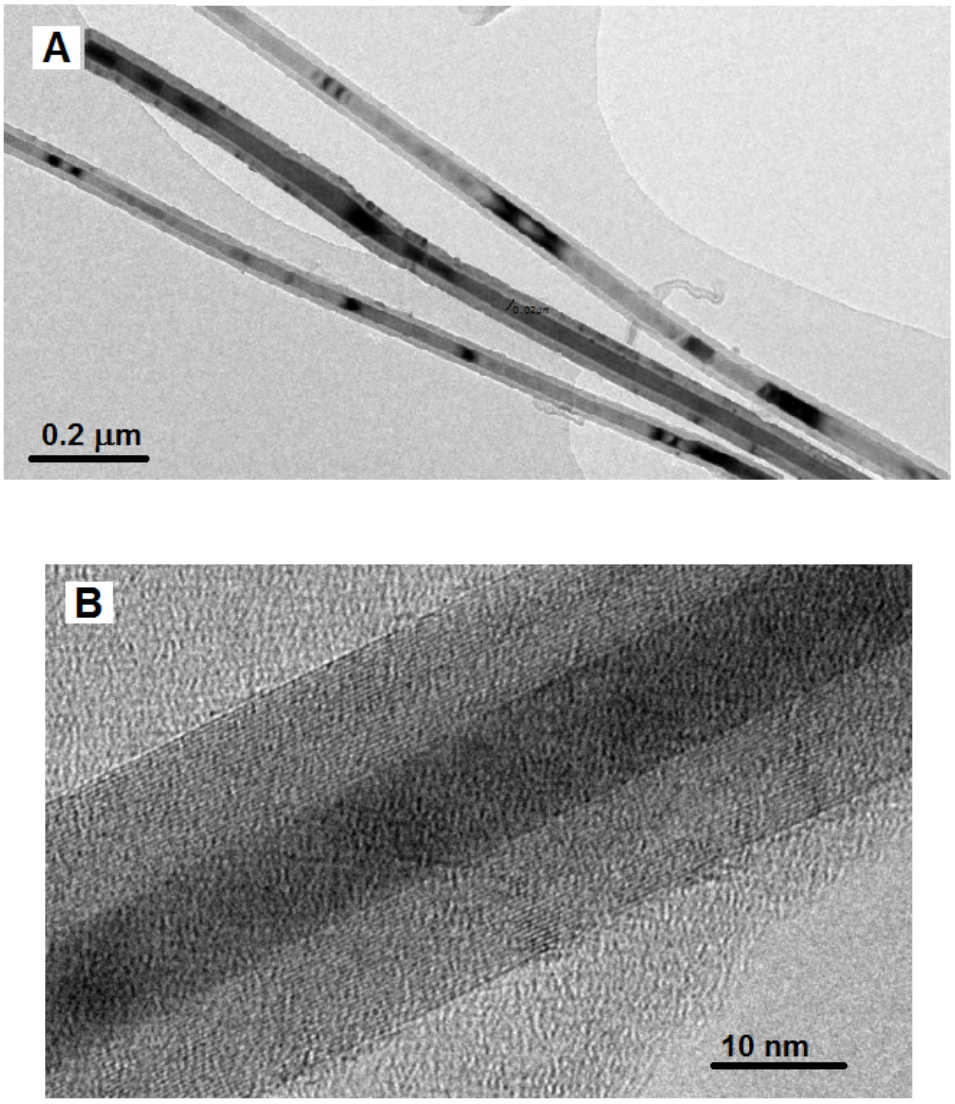

Figure 4.26: TEM images (A, B) at low and high resolutions respectively of structures mechanically removed from substrate B showing contrast between the encapsulated iron nanowires and MWCNTs.

To reconcile the observation of annuli with the knowledge that the substrates, conditions of temperature, and flow-rate were those previously used to produce uniform, close-packed arrays of Fe-MWCNTs of constant height in an unmodulated vapour flow, I speculate the presence of a static, well-defined cell of vapour possessing circular symmetry and an abrupt across-diagonal variation of vapour

density and/or temperature, analogous to the well-known cell structure produced by convection, close to the substrate for the duration of the synthesis [146]. The combination of undulating vapour density in the global flow produced by the structuring of the sublimation process and the temperature gradient across the substrate could, in principle, be the source of the shear forces necessary for the formation of these static cells. The stepwise height variation could therefore be explained by the variation of conditions in the cell driving differential rates of growth. In the schematic diagram, Figure 3.2, substrate A is therefore placed in the position of undulating vapour density.

The morphology of the spherulites resembles that of flower-like structures comprising Fe-MWCNTs radiating from a substrate supported, half-spherical iron island; the array to radial transformation being the result of the increased dimensions of the nucleating iron island [48].

Since the regions away from the agglomerated spherulite areas are vertical arrays, the temperature differences between substrate A and substrate B cannot explain the morphological transformation. However, a static cell model with diffuse across-diagonal variation of conditions could be the basis of the observed differential nucleation; therefore, substrate B is placed in the position of less undulating but higher vapour density in the schematic diagram, Figure 3.2.

In conclusion, in this section it is demonstrated a facile method for self-organized texturing of Fe-MWCNTs arrays by vapour flow modulation capable of imposing annular height variation and vertical-array-to-spherulitic morphological transformation.

Chapter 5

Conclusions

At present two of the key challenges in cancer research are the early stage accurate detection of cancer and delivering the best possible treatment at the right place. The former requires advances in diagnostics and imaging and the latter would benefit from new modalities of treatment.

In this thesis I have presented my research into the development of CNTs as candidate hybrids for dual-functioning magnetic hyperthermia cancer therapy and MRI contrast agent structures. The development of CNTs was achieved by filling the central capillary with continuous ferromagnetic α-Fe nanowires and their surface was funtionalized with paramagnetic Gd(III).

This work has demonstrated the viability of Gd^{3+} functionalized Fe-MWCNTs as high-relaxivity contrast agents for high-field MRI through direct measurement of a relaxivity value of $r_1 \sim 200$ mM^{-1} s^{-1} at high magnetic field (9.4 T). The trend in biomedical MRI is toward high-field imaging owing to better spatial resolution which can lead to early stage detection of cancer. The relaxivity value reported here is the highest among all the candidate high-field T_1 contrast agents. Using these structures as contrast agent for high-field MRI will greatly enhance the ability to detect cancer in its earliest stages.

Also, Gd^{3+} functionalized Fe-MWCNTs exhibited a SAR of 50 W/g_{Fe} in an alternating magnetic field of frequency 696 kHz and field strength of 8 kA/m and a ILP value of 1.12 nHm^2kg^{-1} was estimated. Although at field strength of 8 kA/m the true heating potential of Gd^{3+} functionalized Fe-MWCNTs is not exploited, their ILP value is higher than the ILP values of some tested commercial ferrofluids [76].

Gd^{3+} functionalized Fe-MWCNTs are therefore candidate hybrids for MRI imaging and magnetic hyperthermia cancer therapy with both heating functionality and integrated paramagnetic Gd (III), the most common MRI contrast agent in clinical usage.

The MRI contrast agent functionality will enhance the ability not only to image cancer but also to observe the distribution of Gd^{3+} functionalized Fe-MWCNTs to ensure that they are mainly localized in the tumour and metastases prior to the application of hyperthermia.

This thesis describes a series of methods employed to develop CNTs as a candidate for dual-functioning magnetic hyperthermia structure and MRI contrast agent. These methods allow to obtain CNTs filled with continuous ferromagnetic α-Fe nanowires and surface functionalised with paramagnetic Gd (III). Also, length control of both nanowire and nanotube was achieved.

Firstly, in this thesis it is shown a low vapour flow-rate and constant evaporation temperature CVD method which achieved continuous α-Fe nanowires on the same scale as the nanotube for lengths greater than 10 μm without the necessity of post-synthesis heat-treatment or introduction of other precursor elements.

The low vapour flow-rate regime has the advantage of sustaining the intrinsic temperature gradient at the tip of the forming structure which drives the vapour feedstock to the growth front to guarantee continuous nanowire formation.

The magnetic response was comparable to those for structures produced by more complicated syntheses. For initially mixed-phase nanowires of length less than 10 μm, I confirmed that continuous α-Fe nanowires can be achieved by post-synthesis heat treatment.

The Fe-MWCNTs were grown on smooth Si/SiO_2 substrates held within the second zone of a two-zone horizontal CVD reactor.

In all reactions, the source vapour was produced by evaporation of ferrocene in the first zone using a coil preheater. The temperature of the preheater was kept constant at 185 °C. The ferrocene vapour was carried from the first to the second zone (furnace) in an argon flow of 10 $\pm$ 2 ccm at atmospheric pressure. The substrates were placed in the reaction zone in a region in which the lateral temperature gradient was 10 °C/cm from 880 °C to 950 °C. After the synthesis, the reactor was cooled to room temperature at the natural rate of the furnace. Under these constrains, the key variable was the mass flow rate of ferrocene vapour into the second zone of the reactor. Different mass flow rates (duration time in brackets) 30 mg/min (1.16 min), 34 mg/min (1.16 min), 39 mg/min (1.5 min), 44 mg/min (1.5 min), and 50 mg/min (1.5 min) which I used in the reactions turned to have an approximately linear relationship with the nominal length of Fe-MWCNTs produced : 3 μm, 5 μm, 10 μm, 15 μm, and 20 μm, respectively. From these results it can be concluded that the growth rate of Fe-MWCNTs was

mass transport controlled during the deposition process, since in the low flow rate regime the growth rate is proportional to bulk reactant concentration.

There was a step change in α-Fe content, from $\sim$70% to $\sim$90%, as the length increased from 5 μm to 10 μm whereas γ-Fe and carbide diminished with increasing length. For Fe-MWCNTs with length 20 μm we found an α-Fe content of 94% and very low content of γ-Fe and Fe_3C; 5.7% and 0.3% respectively.

As the length increases from 5 μm to 10 μm it is observed an approximate doubling of both the nanowire and nanotube diameters. For length 5 μm, the average nanowire diameter was 18 nm and that of the nanotube was 48 nm. For the 10 μm structure, the average nanowire diameter was 30 nm and that of the nanotube was 90 nm. The encapsulating nanowires in the 5 μm and 10 μm length structures were continuous for at least 3 μm and 6 μm, respectively.

For length less than 10 μm, continuous α-Fe nanowires were achieved by post-synthesis heat treatment at 500 °C for 12 hours in Ar flow.

The saturation magnetization, M_S and coersivity H_C show length dependence. I observed a slight increase of the saturation magnetization with increasing length and a slight decrease of the coercivity, M_S (5 μm) = 42 emu/g and M_S (10 μm) = 51.5 emu/g, H_C (5 μm) = 910 Oe and H_C (10 μm) = 846 Oe.

Secondly, in this thesis it is demonstrated a simple wet chemical method involving only sonication in aqueous $GdCl_3$ solution to functionalize Fe-MWCNTs with gadolinium; 50 mg of Fe-MWCNT powder and 75 mg of anhydrous gadolinium chloride ($GdCl_3$) were stirred together in 75 ml deionized water and sonicated in an 80 W ultrasonic cleaner for two hours. This method results in loading of Gd^{3+}

ions on the MWCNTs surface due to the ionic interaction between the Gd^{3+} ions and the deprotonated carboxyl groups created on the MWCNT sidewalls during the sonication process. Characterization by EPR, EELS, and HRTEM confirmed the presence of Gd^{3+} ions on the sidewall surface. The ferromagnetic properties of the encapsulated iron nanowire maintained after surface functionalization. At room temperature a saturation magnetization of 40 emu/g and a coercivity of 600 Oe were observed.

Finaly, in this thesis it is described a facile method for self-organized texturing of iron-filled multiwalled carbon nanotube arrays by vapour flow modulation capable of imposing annular height variation and vertical-array-to-spherulitic morphological transformation.

The source vapour for the growth of textured Fe-MWCNTs was produced by the sublimation of 58 mg of ferrocene powder arranged in rows of approximately equal width and separation arranged parallel to the flow of argon carrier gas (flow rate was 10 ccm) in a downstream preheater held at ∼185 °C. Two smooth Si/SiO_2 substrates used for the nucleation and growth of the array were placed in different temperature gradients within the reaction zone (furnace). The first was placed in the gradient 885-940 °C and the second in 940-970 °C. The duration of the reaction, measured from the onset of power supply to the preheater to the complete sublimation of the ferrocene powder, was 1.5 min.

The stepwise variation of height in the closely packed vertically-aligned filled carbon nanotubes was revealed by SEM investigation. Annular features with diameter of 150 μm – 400 μm are found in random locations of the first substrate

with a mean separation of 500 μm. SEM and TEM investigation of material confirmed continuous filling of the multiwalled carbon nanotubes on micrometre length-scale. XRD analyses performed on the samples revealed that the main encapsulated phases were α-Fe, γ-Fe and Fe_3C. The relative weight abundances were found to be: 3% γ-Fe, 7% Fe_3C, 30% α-Fe, 51% MWCNTs and 9% Fe_3O_4. The aggregated regions of clustered spherulites ($\sim$10 μm diameter radial structures comprising hundreds of nanotubes departing from a central particle) were observed on the second substrate. The clustered regions were of several hundred micrometres diameter. EDX analyses performed on substrate-supported samples revealed that the elements present in the product were carbon (56%), iron (29%); the remaining 15% embraces the silicon and oxygen signals from the substrate and trace levels of dysprosium which might be the contamination from microscope.

Backscattered SEM and TEM investigation confirmed that spherulite structures consist of MWCNTs filled with iron nanowires on micrometre length-scale.

Chapter 6

Future work

In addition to the work presented in this thesis, it would be interesting to investigate the potential of Gd^{3+}-functionalized Fe-MWCNTs as a thermometer, by measuring the temperature dependence of NMR parameters like the spin-lattice or the spin-spin relaxation, resonance frequency *etc.* The thermometer will be useful for the magnetic hyperthermia cancer therapy application, to control overheating of normal cells.

The low vapour flow-rate and constant evaporation temperature CVD method can be used to produce long continuous FeNi nanowires encapsulated by MWCNTs. These permalloy nanowires show typical ferromagnetic properties and are attractive candidates for the new types of microwave absorber with thinner coating thickness.

Also, permalloy $Fe_{73}Ni_{27}$ that it is known to tune the Curie temperature, can be used in magnetic hyperthermia cancer therapy to self-control heating in temperature ranges of interest (42 - 46 °C).

Testing the heating efficiency of Gd^{3+}-functionalized Fe-MWCNTs in an alter-

nating magnetic field with a relatively high field amplitude that exceeds their coersivity field (>74 kAm^{-1}) will enable to estimate their true heating potential.

Since the iron nanowires encapsulated by MWCNTs exhibited ferromagnetic hysteresis with high saturation magnetization and relatively high coersivity field $\sim$ 930 Oe (74 kAm^{-1}) we suggest that Fe-MWCNTs produced in this work, may be suitable for developing magnetic memory storage devices.

Further investigation should be done on self-organized textured Fe-MWCNTs such as the structural characterizations with X-ray diffraction and magnetic-structure characterization with magnetometry.

Production of large-area arrays of substrate-supported, self-organized textured Fe-MWCNTs can be of interest for sensor, electrochemical, and electromagnetic absorption applications owing to the anisotropy of mechanical, electrical, and optical properties.

Further studies of the modulated vapour flow would allow to produce larger or smaller annular features and spherulite structures by creating larger or smaller rows of ferrocene powder. Arranging the ferrocene powder in certain ways will enable the production of complex textured Fe-MWNTs, which may be promising for the use in sensors as well as functional elements.

Bibliography

[1] M. Johannsen, U. Gneveckow, K. Taymoorian, B. Thiesen, N. Waldofner, R. Scholz, K. Jung, A. Jordan, P. Wust, S.A. Loening, Morbidity and quality of life during thermotherapy using magnetic nanoparticles in locally recurrent prostate cancer: results of a prospective phase I trial, Int. J. Hyperth. 23 (2007) 315-323.

[2] R.K. Gilchrist, R. Medal, W.D. Shorey, R.C. Hanselman, J.C. Parrot, C.B. Taylor, Selective inductive heating of lymph nodes, Annals of Surgery 146 (1957) 596-606.

[3] B. Thiesen, A. Jordan, Clinical applications of magnetic nanoparticles for hyperthermia, Int J Hyperthermia 14 (2008) 467-474.

[4] R. Klingeler , R.B. Sim , editors, Carbon nanotubes for biomedical applications, Springer (2011).

[5] F. Yang, J. Hu, D.Yang, J. Long, G. Luo, C. Jin, X. Yu, J. Xu, C. Wang, Q. Ni and D. Fu, Pilot study of targeting magnetic carbon nanotubes to lymph nodes, Nanomedicine 4 (2009) 317-30.

[6] K.M. Krishnan, Biomedical nanomagnetics: A spin through possibilities in imaging, diagnostics, and therapy, IEEE Transactions on Magnetics 46 (2010) 2523–2558.

[7] J.B. Livramento, C. Weidensteiner, M.I.M. Prata, P.R. Allegrini, C.F.G.C. Geraldes, L. Helm, R. Kneuer, A.E. Merbach, A.C. Santos, P. Schmidt and E. Toth, First in vivo MRI assessment of a self-assembled metallostar compound endowed with a remarkable high field relaxivity, Contrast Med. Mol. Imaging 1 (2006) 30–39.

[8] T. Vaughan, L. DelaBarre, C. Snyder, J. Tian, C. Akgun, D. Shrivastava, W. Liu, C. Olson, G. Adriany, J. Strupp, P. Andersen, A. Gopinath, P.F. van de Moortele, M. Garwood, and K. Ugurbil, 9.4 T human MRI: Preliminary results, Mag. Reson. Med. 56(6) (2006) 1274–1282.

[9] Y.L. Hsin, J.Y. Lai, K.C. Hwang, S.C. Lo, F.R. Chen, J.J. Kai, Rapid surface functionalization of iron-filled multi-walled carbon nanotubes, Carbon 44 (2006) 3328–35.

[10] H. Zhang, N. Du, P. Wu, B. Chen, D. Yang, Functionalization of carbon nanotubes with magnetic nanoparticles: general nonaqueous synthesis and magnetic properties, Nanotechnology 19 (2008) 3156-04.

[11] C. Cunha, S. Panseri, D. Iannazzo, A. Piperno, A. Pistone, M. Fazio, et al, Hybrid composite made of multiwalled carbon nanotubes functionalized with Fe_3O_4 nanoparticles for tissue engineering applications. Nanotechnology 23 (2012) 4651-02.

[12] J.F. Marco, J.R. Gancedo, A. Hernando, P. Crespo, C. Prados, J.M. Gonzalez, N. Grobert, M. Terrones, D.R.M. Walton, H.W. Kroto, Mossbauer

study of iron containing carbon nanotubes, Hyperfine Interact. 139(140) (2002) 535-542.

[13] C. Prados, P. Crespo, J.M. Gonzalez, A. Hernando, J.F. Marco, Gancedo, et al., Hysteresis shift in Fe-filled carbon nanotubes due to γ-Fe, Phys. Rev. B 65 (2002) 113405-113409.

[14] A. Leonhardt, M. Ritchel, R. Kozhuharova, A. Graff, T. Muhl, R. Huhle, et al., Synthesis and properties of filled carbon nanotubes, Diam. Relat. Mater. 12 (3-7) (2003) 790-793.

[15] K. Kuwana, K. Saito, Modelling CVD synthesis of carbon nanotubes: nanoparticle formation from ferrocene, Carbon 43 (10) (2005), 2088-95.

[16] A. Leonhardt, S. Hampel, C. Muller, I. Monch, R. Koseva, M. Ritschel, et al., Synthesis, properties and application of ferromagnetic-filled carbon nanotubes, Chem. Vap. Depos. 12 (2006) 380-387.

[17] S. Hampel, A. Leonhardt, D. Selbmann, K. Biedermann, D. Elefant, C. Muller, et al., Growth and characterization of filled carbon nanotubes with ferromagnetic properties, Carbon 44 (2006) 2316-2322.

[18] C. Muller, D. Golberg, A. Leonhardt, S. Hampel, B. Buchner, Growth studies, TEM and XRD investigations of iron-filled carbon nanotubes, Phys. Status Solidi (A) 203 (2006) 1064-1068.

[19] D. Goldberg, M. Mitome, C. Muller, C. Tang, A. Leonhardt, Y. Bando, Atomic structures of iron-based single-crystalline nanowires crystallized in-

side multi-walled carbon nanotubes as revealed by analytical electron microscopy, Acta Mater. 54 (2006) 2567-2576.

[20] T. Ruskov, I. Spirov, M. Ritschel, C. Muller, A. Leonhardt, R. Ruskov, Mossbauer morphological analysis of Fe-filled multiwalled carbon nanotubes samples, J. Appl. Phys. 100 (2006) 084326.

[21] X. Gui, J. Wei, K. Wang, W. Wang, R. Lv, J. Chang, et al., Improved filling rate and enhanced magnetic properties of Fe-filled carbon nanotubes by annealing and magnetic separation, Mater. Res. Bull. 43 (2008) 3441-3446.

[22] U. Weissker, M. Loffler, F. Wolny, M.U. Lutz, N. Scheerbaum, R. Klingeler, et al., Perpendicular magnetization of long iron carbide nanowires inside carbon nanotubes due to magnetocrystalline anisotropy, J. Appl. Phys. 106 (2009) 054909.

[23] M.U. Lutz, U. Weissker, F. Wolny, C. Muller, M. Loffer, T. Muhl, et al., Magnetic properties of α-Fe and Fe_3C nanowires, J. Phys. Conf. Ser. 200 (2010) 072062.

[24] U. Weissker, S. Hampel, A. Leonhardt, B. Buchner, Carbon nanotubes filled with ferromagnetic materials, Materials 3 (2010) 4387-4427.

[25] M.S. Shamsudin, N.A. Asli, S. Abdullah, S.Y.S. Yahya, Effect of synthesis temperature on the growth iron-filled carbon nanotubes as evidenced by structural, micro-raman, and thermogravimetric analyses, Adv. Condens. Matter Phys. (2012) 420619.

[26] F.S. Boi, G. Mountjoy, M. Baxendale, Boundary layer chemical vapor synthesis of self-organized radial filled-carbon-nanotube structures, Carbon 64 (2013) 516-526.

[27] M.D. Rossell, C. Kuebel, G. Ilari, F. Rechberger, F.J. Heiligtag, M. Niederberger, et al, Impact of sonication pre-treatment on carbon nanotubes: a transmission electron microscopy study, Carbon 61 (2013) 404–11.

[28] L. Meng, C. Fu, Q. Lu, Advanced technology for functionalization of carbon nanotubes, Prog. Nat. Sci. 19 (2009) 801–10.

[29] S. Lefrant, J.P. Buisson, J. Schreiber, et al, Raman studies of carbon nanotubes and polymer nanotube composites, Mol. Cryst. Liq. Cryst. 415 (2004) 125–32.

[30] N. Nakayama-Ratchford, S. Bangsaruntip, X.M. Sun, et al, Noncovalent functionalization of carbon nanotubes by fluorescein-polyethylene glycol: supramolecular conjugates with pH-dependent absorbance and fluorescence, J. Am. Chem. Soc. 129 (2007) 2448–9.

[31] J.G. Yu, K.L. Huang, S.Q. Liu, et al, Preparation and characterization of polycarbonate modified multiple-walled carbon nanotubes, Chin. J. Chem. 26 (2008) 560–3.

[32] D-Q. Yang, J-F. Rochette, E. Sacher, Functionalization of multiwalled carbon nanotubes by mild aqueous sonication, J. Phys. Chem. B 109 (2005) 7788–94.

[33] S. Simon, I. Ardelean, S. Filip, I. Bratu, I. Cosma, Structure and magnetic properties of Bi_2O_3–GeO_3–Gd_2O_3 glasses, Solid State Commun. 116 (2000) 83.

[34] M.C.R. Symons, Electron spin resonance part 2, Royal Society of Chemistry (1993).

[35] S. Iijima, Helical microtubules of graphitic carbon, Nature 354 (1991) 56 - 58.

[36] C. Chen, Y. Zhang, Nanowelded carbon nanotubes: From field-effect transistors to solar microcells, Springer (2009).

[37] M.F. Yu, O. Lourie, M.J. Dyer, K. Moloni, T.F. Kelly and R.S. Ruoff, Strength and breaking mechanism of multi-walled carbon nanotubes under tensile load, Science 287 (2000) 637–640.

[38] F. Wolny, T. Mühl, U. Weissker, K. Lipert, J. Schumann, B. Büchner, A. Leonhardt, Iron filled carbon nanotubes as novel monopole-like sensors for quantitative magnetic force microscopy, Nanotechnology 21 (2010) 435501.

[39] R. C. Mehrotra, Organometallic Chemistry: New Age International (2004).

[40] R.S. Wagner and W.C. Ellis, Vapor-liquid-solid mechanism of single crystal growth. Appl. Phys. Lett. 4 (1964) 89–90.

[41] R.T.K. Baker and P.S. Harris, The formation of filamentous carbon, Chemistry and Physics of Carbon 14 (1978) 83.

[42] S. Bellucci, A. Malesevic, Physics of carbon nanostructures in: Physical properties of ceramic and carbon nanoscale structures. Lecture Notes in Nanoscale Science and Technology, Springer 11 (2011) 155-94.

[43] G.G. Tibbetts, Why are carbon filaments tubular? Journal of Crystal Growth 66 (1984) 632-38.

[44] A.G. Nasibulina, A. Moisalaa, D.P. Brownb, E.I. Kauppinena, Carbon nanotubes and onions from carbon monoxide using $Ni(acac)_2$ and $Cu(acac)_2$ as catalyst precursors, Carbon 41 (2003) 2711–2724.

[45] T. Guo, P. Nikolaev, A.G. Rinzler, D. Tomanek, D.T. Colbert, R.E. Smalley, Self-assembly of tubular fullerenes, Journal of Physical Chemistry 99 (1995) 10694-7.

[46] Y-K. Kwon, Y.H. Lee, S-G. Kim, P. Jund, D. Tomanek, R.E. Smalley, Morphology and stability of growing multiwall carbon nanotubes, Physical Review Letters 79 (1997) 2065-8.

[47] I. Kunadian, R. Andrews, D. Qiana, M.P. Menguc, Growth kinetics of MWCNTs synthesized by a continuous-feed CVD method, Carbon 47 (2009) 384–395.

[48] F.S. Boi, Ferromagnetically filled carbon nanotubes: Radial structures and tuning of magnetic properties through new synthesis methods, http://qmro.qmul.ac.uk/jspui/handle/123456789/8734 (2013).

[49] M. Kumar, Y. Ando, Chemical vapor deposition of carbon nanotubes: A review on growth mechanism and mass production, Journal of Nanoscience and Nanotechnology 10 (2010) 3739–58.

[50] A. Schneider, Iron layer formation during cementite decomposition in carburising atmospheres, Corros. Sci. 44 (2002) 2353-2365.

[51] A. Leonhardt, M. Ritschel, D. Elefant, N. Mattern, K. Biedermann, S. Hampel, et al., Enhanced magnetism in Fe-filled carbon nanotubes produced by pyrolysis of ferrocene, J. Appl. Phys. 98 (2005) 074315.

[52] F.S. Boi, S. Maugeri, J. Guo, M. Lan, S. Wang, J. Wen, et al., Controlling the quantity of α-Fe inside multiwall carbon nanotubes filled with Fe-based crystals: the key role of vapor flow-rate, Appl. Phys. Lett. 105 (2014) 243108.

[53] Q. Liu, Z-G. Chen, B. Liu, W. Ren, F. Li, H. Cong, H-M. Cheng, Synthesis of different magnetic carbon nanostructures by the pyrolysis of ferrocene at different sublimation temperatures, Carbon 46 (2008) 1892-1902

[54] J. Jorge, E. Flahaut, F. Gonzalez-Jimenez, G. Gonzalez, J. Gonzalez, E. Belandria, et al., Preparation and characterization of α-Fe nanowires located inside double wall carbon nanotubes, Chem. Phys. Lett. 457 (2008) 347-351.

[55] X. Guia, K. Wanga, W. Wanga, J. Wei, X. Zhanga, R. Lvc, et al., The decisive roles of chlorine-contained precursor and hydrogen for the filling

Fe nanowires into carbon nanotubes, Mater. Chem. Phys. 113 (2009) 634-637.

[56] S. Karmakar, S.M. Sharma, M.D. Mukadam, S.M. Yusuf, A.K. Sood, Magnetic behaviour of iron-filled multiwalled carbon nanotubes, Journal of Applied Physics 97 (2005) 054306.

[57] V. Likodimos, S. Glenis, N. Guskos, C.L. Lin, Magnetic and electronic properties of multiwall carbon nanotubes, Physical Review B 68 (2003) 045417.

[58] K. Lipert, S. Bahr, F. Wolny, P. Atkinson, U. Weisker, T. Mühl, O.G. Schmidt, B. Büchner, and R. Klingeler, An individual iron nanowire-filled carbon nanotube probed by micro-Hall magnetometry, Applied Physics Letters 97 (2010) 212503.

[59] F.C. Dillon, A. Bajpai, A. Koos, S. Downes, Z. Aslam, N. Grobert, Tuning the magnetic properties of iron-filled carbon nanotubes, Carbon 50 (2012) 3674-3681.

[60] D.L. Leslie-Pelecky, R.D. Rieke, Magnetic properties of nanostructured materials, Chem. Mater. 8 (1996) 1770-1783.

[61] K. Balasubramanian, M. Burghard, Chemically functionalized carbon nanotubes, Small 1 (2005) 180–92.

[62] B. Sitharaman, K.R. Kissell, K.B. Hartman, L.A. Tran, A. Baikalov, I. Rusakova, Y. Sun, H.A. Khant, S.J. Ludtke, W. Chiu, S. Laus, E. Toth,

L. Helm, A.E. Merbach, and L.J. Wilson, Superparamagnetic gadonanotubes are high-performance MRI contrast agents, Chem. Commun. 31 (2005) 3915-3917.

[63] C. Richard, B-T. Doan, J-C. Beloeil, M. Bessodes, E. Toth and D. Scherman, Noncovalent functionalization of carbon nanotubes with amphiphilic Gd^{3+} chelates: toward powerful T_1 and T_2 MRI contrast agents, Nano Letters 8 (2008) 232-6.

[64] J.T-W. Wang, L. Cabana, M. Bourgognon, H. Kafa, A. Protti, K. Venner, A.M. Shah, J. Sosabowski, S.J. Mather, A. Roig, X. Ke, G.V. Tendeloo, R.T.M de Rosales, G. Tobias and K.T. Al-Jamal, Magnetically decorated multiwalled carbon nanotubes as dual MRI and SPECT contrast agents, Advanced Functional Materials 24(13) (2014) 1880-1894.

[65] J.H. Choi, F.T. Nguyen, P.W. Barone, D.A. Heller, A.E. Moll, D. Patel, S.A. Boppart, M.S. Strano, Multimodal biomedical imaging with asymmetric single-walled carbon nanotube/iron oxide nanoparticle complexes, Nano Lett. 7 (2007) 861-7.

[66] H.X. Wu, G. Liu, Y.M. Zhuang, D.M. Wu, H.Q. Zhang, H. Yang, H. Hu, S.P. Yang, The behavior after intravenous injection in mice of multiwalled carbon nanotube / Fe_3O_4 hybrid MRI contrast agents, Biomaterials 32 (2011) 4867-76.

[67] B. Chen, H. Zhang, C. Zhai, N. Du, C. Sun, J. Xue, D. Yang, H. Huang, B. Zhang, Q. Xie and Y. Wu, Carbon nanotube-based magnetic-fluorescent

nanohybrids as highly efficient contrast agents for multimodal cellular imaging, J. Mater. Chem. 20 (2010) 9895–9902.

[68] B. Sitharaman, B.D. Jacobson, Y.Z. Wadghiri, H. Bryant, J. Frank, The magnetic, relaxometric, and optical properties of gadolinium-catalyzed single walled carbon nanotubes, J. Appl. Phys. 113 (2013) 134308.

[69] P.M. Martin, editor, Handbook of deposition technologies for films and coatings (Third Edition), Elsevier (2010).

[70] M. Winterer, Nanocrystalline ceramics - synthesis and structure, Springer, Heidelberg, Springer Series in Materials Science Volume 53 (2002).

[71] C.E. Morosanu, Thin films by chemical vapour deposition, Elsevier (1990).

[72] H. Schlichting, Boundary layer theory, 6th ed., McGraw-Hill, New York (1968).

[73] J-H. Park, T.S. Sudarshan, editors, Chemical vapor deposition, The material information society (2001).

[74] M. Ohring, The material science of thin films, Academia Press (1992).

[75] F. Matsuoka, M. Shinkai, H. Honda, T. Kubo, T. Sugita, T. Kobayashi, Hyperthermia using magnetite cationic liposomes for hamster osteosarcoma, Biomagn. Res. Technol. 2 (2004).

[76] M. Kallumadil, M. Tada, T. Nakagawa, M. Abe, P. Southern, Q.A. Pankhurst, Suitability of commercial colloids for magnetic hyperthermia, Journal of Magnetism and Magnetic Materials 321 (2009) 1509–1513.

[77] Q.A. Pankhurst, J. Connolly, S.K. Jones, and J. Dobson, Application of magnetic nanoparticles in biomedicine, J. Phys. D: Appl. Phys. 36 (2003) 167-181.

[78] M. Farle, Magnetism goes nano, C4, Forschungszentrum Juelich (2005).

[79] C.S.S.R. Kumar, Nanomaterials for cancer therapy, Wiley-VCH (2006) 291-296.

[80] W.C. Elmore, The magnetization of ferromagnetic colloids, Phys. Rev. 54 (1938) 1092–1095.

[81] J.R. Oleson, T.C. Cetas and P.M. Corry, Hyperthermia by magnetic induction: experimental and theoretical results for coaxial coil pairs, Radiat. Res. 95 (1983) 175-86.

[82] J.P. Reilly, Principles of nerve and heat excitation by time-varying magnetic fields, Ann. New York Acad. Sci. 649 (1992) 96-117.

[83] W.J. Atkinson, I.A. Brezovich and D.P. Chakraborty, Usable frequencies in hyperthermia with thermal seeds, IEEE Trans. Biomed. Eng. BME 31 (1984) 70-5.

[84] S. Dutz and R. Hergt, Magnetic nanoparticles heating and heat transfer on a microscale: Basic principles, realities and physical limitations of hyperthermia for tumour therapy, Int. J. Hyperthermia 29(8) (2013) 790-800.

[85] Q.A. Pankhurst, N.T.K. Thanh, S.K. Jones, J. Dobson, Progres in applications of magnetic nanoparticles in biomedicine, J. Phys. D Appl. Phys. 42 (2009) 224001.

[86] W.R. Bauer and K. Schulten, Theory of contrast agents in magnetic resonance imaging: Coupling of spin relaxation and transport, Magnetic Resonance in Medicine 26 (1992) 16-39.

[87] P. Caravan, Strategies for increasing the sensitivity of gadolinium based MRI contrast agents, Chem. Soc. Rev. 35 (2006) 512-23.

[88] W.M.B. Jeff and L.K. Dara, Iron oxide MR contrast agents for molecular and cellular imaging, NMR Biomed. 17 (2004) 484–499.

[89] R. Weissleder and M. Papisov, Pharmaceutical iron oxides for MR imaging, Rev. Magn. Reson. Med. 4 (1992) 1-20.

[90] T.E. Yankeelov, D.R. Pickens, R.R. Price, Quantitative MRI in cancer, Taylor and Francis (2011).

[91] P. Caravan, J. Ellison, T. McMurry, R. Lauffer, Gadolinium (III) chelates as MRI contrast agents: structure, dynamics, and applications, Chem. Rev. 99 (1999) 2293-2352.

[92] R. Rebizak, M. Schaefer and E. Dellacherie, Polymeric conjugates of Gd^{3+}-diethylenetriaminepentaacetic acid and dextran.2. Influence of spacer arm length and conjugate molecular mass on the paramagnetic properties and some biological parameters, Bioconjugate Chem. 9 (1998) 94-99.

[93] F.N. Franano, W.B. Edwards, M.J. Welch, M.W. Brechbiel, O.A. Gansow and J.R. Duncan, Biodistribution and metabolism of targeted and nontargeted protein-chelate-gadolinium complexes: evidence for gadolinium dissociation in vitro and in vivo, Magn. Reson. Imaging 13 (1995) 201-14.

[94] A.E. Merbach and E. Toth, Editors, The Chemistry of contrast agents in medical magnetic resonance imaging, John Wiley and Sons, Chichester, (2001).

[95] J.A. Peters, J. Huskens and D.J. Raber, Lanthanide induced shifts and relaxation rate enhancements Prog. NMR Spectrosc. 28 (1996) 283-350.

[96] S.H. Koenig and R.D. Brown III, Field-cycling relaxometry of protein solutions and tissue: implication for MRI, Prog. NMR Spectrosc. 22 (1990) 487-567.

[97] R.B. Lauffer, Paramagnetic metal complexes as water proton relaxation agents for NMR imaging: theory and design, Chem. Rev. 87 (1987) 901–927.

[98] S. Aime, M. Botta, M. Fasano and E. Terreno, Lanthanide (III) chelates for NMR biomedical applications, Chemical Society Reviews 27 (1998).

[99] L. Banci, I. Bertini and C. Luchinat, Nuclear and electron relaxation (1991) VCH, Weinheim.

[100] W. Krause, Volume Editor, Contrast agents I: Magnetic resonance imaging, Springer (2002).

[101] N. Bloembergen, Proton relaxation times in paramagnetic solutions, J. Chem. Phys. 27 (1957) 572.

[102] I. Solomon, Relaxation processes in a system of two spins, Phys. Rev. 99 (1955) 559-565.

[103] J.H. Freed, Dynamic effects of pair correlation functions on spin relaxation by translational diffusion in liquids. II. Finite jumps and independent T1 processes, J. Chem. Phys. 68 (1978) 4034.

[104] A.D. Sherry, P. Caravan, and R.E. Lenkinski, A primer on gadolinium chemistry, J. Magn. Reson. Imaging. 30(6) (2009) 1240–1248.

[105] G.M. Nicolle, E. Toth, H. Schmitt-Willich, B. Raduchel,and A.E. Merbach, The impact of rigidity and water exchange on the relaxivity of a dendritic MRI contrast agent, Chem. Eur. J. 8 (2002) 1040-1048.

[106] E. Toth, D. Pubanz, S. Vauthey, L. Helm, and A.E. Merbach, The role of water exchange in attaining maximum relaxivities for dendrimeric MRI contrast agents, Chem. Eur. J. 2 (1996) 1607-1615.

[107] E.C. Wiener, M.W. Brechbiel, H. Brothers, R.L. Magin, O.A. Gansow, D.A. Tomalia, and P.C. Lauterbur, Dendrimer-based metal-chelates - a new class of magnetic-resonance-imaging contrast agents. Magn. Reson. Med. 31 (1994) 1-8.

[108] E. Toth, L. Helm, A.E. Merbach, Relaxivity of MRI contrast agents. Contrast agent I, Springer 221 (2002) 61-101.

[109] A.D. Sherry and Y. Wu, The importance of water exchange rates in the design of responsive agents for MRI, Curr. Opin. Chem. Biol. 17(2) (2013) 167–174.

[110] K.N. Raymond and V.C. Pierre, Next generation, high relaxivity gadolinium MRI agents, Bioconjugate Chem. 16 (2005) 3-8.

[111] L. Helm, A.E. Merbach, Inorganic and bioinorganic solvent exchange mechanisms, Chem. Rev. 105(6) (2005) 1923-59.

[112] M. Birkholz, Thin film analysis by X-Ray scattering, Wiley-VCH (2006).

[113] R.F. Egerton, Electron energy-loss spectroscopy in the TEM, Rep. Prog. Phys. 72 (2009) 016502.

[114] H. Lin, H. Zhu, H. Guo, L. Yu, Investigation of the microwave-absorbing properties of Fe-filled carbon nanotubes, Mater. Lett. 61 (2007) 3547-3550.

[115] S. Hudziak, A. Darfeuille, R. Zhang, T. Peijs, G. Mountjoy, G. Bertoni, M. Baxendale, Magnetoresistive phenomena on Fe-filled carbon nanotube/elastomer composites, Nanotechnology 21 (12) (2010) 125505.

[116] R. Klingeler, S. Hampel, B. Büchner, Carbon nanotube based biomedical agents for heating, temperature sensoring and drug delivery, Int. J. Hyperth. 24 (6) (2008) 496-505.

[117] I. Monch, A. Leonhardt, A. Meye, S. Hampel, R. Kozhuharova-Kosera, D. Elefant, et al., Synthesis and characterization of Fe-filled multi-walled

carbon nanotubes for biomedical application, J. Phys. Conf. Ser. 61 (2007) 820-824.

[118] M. Ferrari, Cancer nanotechnology: opportunities and challenges, Nat. Rev. Cancer 5 (2005) 161-171.

[119] I. Monch, A. Meye, A. Leonhardt, K. Kramer, R. Kozhuharova, T. Gemming, et al., Ferromagnetic filled carbon nanotubes and nanoparticles: synthesis and lipid-mediated delivery into human tumour cells, J. Magn. Magn. Mater. 290-291 (1) (2005) 276-278.

[120] P.C.P. Watts, W.K. Hsu, D.P. Randall, V. Kotzeva, G.Z. Chen, Fe-Filled carbon nanotubes: nano-electromagnetic inductors, Chem. Mater. 14 (2002) 4505-4508.

[121] F. Wolny, T. Mühl, U. Weissker, K. Lipert, J. Schumann, B. Büchner, A. Leonhardt, Iron filled carbon nanotubes as novel monopole-like sensors for quantitative magnetic force microscopy, Nanotechnology 21 (2010) 435501.

[122] R. Lv, S. Tsuge, X. Guic, K. Takaib, F. Kanga, T. Enoki, J. Weic, J. Gua, K. Wang, D. Wuc, In situ synthesis and magnetic anisotropy of ferromagnetic buckypaper, Carbon 47 (2009) 1141-1145.

[123] A. Morelos-Gomez, F. Lopez-Urias, E. Munoz-Sandoval, C.L. Dennis, R.D. Shull, H. Terrones, et al., Controlling high coercivities of ferromagnetic nanowires encapsulated in carbon nanotubes, J. Mater. Chem. 20 (2010) 5906-5914.

[124] J.H. Gao, D.L. Sun, Q.F. Zhan, W. He, Z.H. Cheng, Magnetization reversal process and magnetic relaxation of self-assembled Fe_3Pt nanowire arrays with different diameters: experiment and micromagnetic simulations, Phys. Rev. B 75 (2007) 064421.

[125] M. Kersten, Underlying theory of ferromagnetic hysteresis and coercivity, Z. Phys. 44 (1943) 63.

[126] G. Herzer, Nanocrystalline soft magnetic materials, J. Magn. Magn. Mater. 112 (1992) 258-262.

[127] S. Tebble, D.J. Craik, Magnetic materials, Wiley, New York, 1966.

[128] J. Haglund, G. Grimvall, T. Jarlborg, Electronic structure, x-ray photoemission spectra, and transport properties of Fe_3C (cementite), Phys. Rev. B 44 (7) (1991) 2914-2919.

[129] G.F. Goya, T.S. Berquo, F.C. Fonseca, M.P. Morales, Static and dynamic magnetic properties of spherical magnetite nanoparticles, J. Appl. Phys. 94 (5) (2003) 3520-3528.

[130] Z.H. Wang, Z.D. Zhang, C.J. Choi, B.K. Kim, Structure and magnetic properties of Fe(C) and Co(C) nanocapsules prepared by chemical vapor condensation, J. Alloys Compd. 361 (2003) 289-293.

[131] V. Sohatsky, S. Kolesnik, D. Makarov, A. Leonhardt, T. Muehl, I. Moench, et al. ESR of Fe-filled multi-walled carbon nanotubes, Fullerenes, Nanotubes, Carbon Nanostruct 13 (2005) 401–10.

[132] J. Kliava, A. Malakhovskii, I. Edelman, A. Potseluyko, E. Petrakovskaja, S. Melnikova, et al, Unusual magnetic transitions and nature of magnetic resonance spectra in oxide glasses containing gadolinium, Phys. Rev. B 71 (2005) 104406.

[133] J. Kliava, I.S. Edelman, A.M. Potseluyko, E.A. Petrakovskaja, R. Berger, I. Bruckental, et al. Magnetic and optical properties and electron paramagnetic resonance of gadolinium-containing oxide glasses, J. Phys: Condens Matter 15 (2003) 6671.

[134] K. Suenaga, S. Iijima, H. Kato, H. Shinohara, Fine-structure analysis of GdM_{45} near-edge EELS on the valence state of $Gd@C_{82}$ microcrystals, Phys. Rev. B 62 (2000) 1627–30.

[135] K. Yase, S. Horiuchi, M. Kyotani, M. Yumura, K. Uchida, S. Ohshima, et al. Angular resolved EELS of a carbon nanotube, Thin Solid Films 273 (1996) 222–4.

[136] M. Abbas, Z.Y. Wu, J. Zhong, K. Ibrahim, A. Fiori, S. Orlanducci, et al. X-ray absorption and photoelectron spectroscopy studies on graphite and single-walled carbon nanotubes: oxygen effect, Appl. Phys. Lett. 87 (2005) 051923.

[137] H.K. Jeong, H.J. Noh, J.Y. Kim, M.H. Jin, C.Y. Park, Y.H. Lee, X-ray absorption spectroscopy of graphite oxide, Europhys. Lett. 82 (2008) 67004.

[138] V. Datsyuk, M. Kalyva, K. Papagelis, J. Parthenios, D. Tasis, et al. Chemical oxidation of multiwalled carbon nanotubes, Carbon 46 (2008) 833–40.

[139] U. Zielke, K.J. Huttinger, W.P. Hoffman, Surface-oxidized carbon fibres: I. Surface structure and chemistry, Carbon 34 (1996) 983.

[140] J-P. Tessonnier, O. Ersen, G. Weinberg, C. Pham-Huu, D.S. Su, R. Schlogl, Selective deposition of metal nanoparticles inside or outside multiwalled carbon nanotubes, Am. Chem. Soc. 3 (2009) 2081–9.

[141] A.J. Hajdú, E. Tombácz, I. Bányai, M. Babos, A. Palko, Carboxylated magnetic nanoparticles as MRI contrast agents: Relaxation measurements at different field strengths, Journal of Magnetism and Magnetic Materials 324 (2012) 3173–3180.

[142] Q. Ma, M. Jebb, M.F. Tweedle and L.J. Wilson, The gadonanotubes: structural origin of their high-performance MRI contrast agent behavior, J. Mater. Chem. B 1 (2013) 5791-5797.

[143] J. Carrey, B. Mehdaoui, M. Respaud, Simple models for dynamic hysteresis loop calculations of magnetic single-domain nanoparticles, application to magnetic hyperthermia optimization, J. Appl. Phys. 109 (2011) 083921.

[144] R. Hergt, R. Hiergeist, I. Hilger, W.A. Kaiser, Y. Lapatnikov, S. Margel, U. Richter, Maghemite nanoparticles with very high AC-losses for application in RF-magnetic hyperthermia, Magn. Magn. Mater. 270 (2004) 345–357.

[145] Z.J. Zhang, B. Wei, J.W. Ward, R. Vajtai, G. Ramanath, P.M. Ajayan, Select pathways to carbon nanotube film growth, Advance Materials 13 (2001) 1767-1770.

[146] H.L. Grant, R.W. Stewart and A. Moilliet, Turbulence spectra from a tidal channel, Journal of fluid mechanics 12 (1962) 241-268.